

RICE UNIVERSITY

**Compressive Sensing and Imaging Applications**

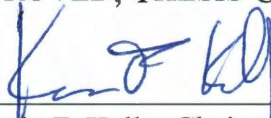
by

**Ting Sun**

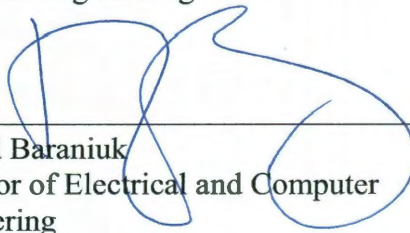
A THESIS SUBMITTED  
IN PARTIAL FULFILLMENT OF THE  
REQUIREMENTS FOR THE DEGREE

**Doctor of Philosophy**

APPROVED, THESIS COMMITTEE:



Kevin F. Kelly, Chair  
Associate Professor of Electrical and  
Computer Engineering



Richard Baraniuk  
Professor of Electrical and Computer  
Engineering



Wotao Yin  
Assistant Professor of Computational and  
Applied Mathematics

Houston, Texas

*December, 2011*

## ABSTRACT

### Compressive Sensing and Imaging Applications

by

Ting Sun

Compressive sensing (CS) is a new sampling theory which allows reconstructing signals using sub-Nyquist measurements. It states that a signal can be recovered exactly from randomly undersampled data points if the signal exhibits sparsity in some transform domain (wavelet, Fourier, etc). Instead of measuring it uniformly in a local scheme, signal is correlated with a series of sensing waveforms. These waveforms are so called sensing matrix or measurement matrix. Every measurement is a linear combination of randomly picked signal components. By applying a nonlinear convex optimization algorithm, the original can be recovered. Therefore, signal acquisition and compression are realized simultaneously and the amount of information to be processed is considerably reduced.

Due to its unique sensing and reconstruction mechanism, CS creates a new situation in signal acquisition hardware design as well as software development, to handle the increasing pressure on imaging sensors for sensing modalities beyond visible (ultraviolet, infrared, terahertz etc.) and algorithms to accommodate demands for higher-dimensional datasets (hyperspectral or video data cubes). The combination of CS with traditional optical imaging extends the capabilities and also improves the performance of existing equipments and systems.

Our research work is focused on the direct application of compressive sensing for

imaging in both 2D and 3D cases, such as infrared imaging, hyperspectral imaging and sum frequency generation microscopy. Data acquisition and compression are combined into one step. The computational complexity is passed to the receiving end, which always contains sufficient computer processing power. The sensing stage requirement is pushed to the simplest and cheapest level.

In short, simple optical engine structure, robust measuring method and high speed acquisition make compressive sensing-based imaging system a strong competitor to the traditional one. These applications have and will benefit our lives in a deeper and wider way.

# Contents

Abstract	ii
List of Illustrations	vii
List of Tables	xii
<b>1 Introduction to Sampling Theorem</b>	<b>1</b>
1.1 Nyquist-Shannon Sampling Theorem . . . . .	1
1.2 Compressive Sensing Theorem . . . . .	3
1.3 Compressive Sensing for Imaging . . . . .	7
1.3.1 Single Pixel Camera . . . . .	7
1.3.2 Circuit Failure Analysis . . . . .	8
1.3.3 Sum Frequency Generation . . . . .	10
1.3.4 Hyperspectral Imaging . . . . .	11
<b>2 Compressive Sensing Theory</b>	<b>14</b>
2.1 Sparsity . . . . .	14
2.2 Incoherent Projection . . . . .	16
2.3 Signal Reconstruction . . . . .	18
2.4 Pseudorandom Pattern . . . . .	20
2.5 Simulation Results . . . . .	23
<b>3 Single Pixel Camera</b>	<b>27</b>
3.1 Digital Micromirror Device . . . . .	27
3.1.1 introduction . . . . .	27
3.2 Light Modulator Package . . . . .	29



3.3	Single Pixel Camera . . . . .	32
3.3.1	Architecture . . . . .	32
3.3.2	Multiplexing Methodology . . . . .	33
3.3.3	Advantages . . . . .	37
<b>4</b>	<b>CS Application to OBIC and IR-PEM</b>	<b>39</b>
4.1	Introduction . . . . .	40
4.1.1	OBIC . . . . .	41
4.1.2	PEM . . . . .	41
4.2	SNR Analysis . . . . .	43
4.3	Experimental Setup . . . . .	47
4.4	Experimental Results . . . . .	50
4.4.1	OBIC Results . . . . .	50
4.4.2	IR-PEM Results . . . . .	57
4.5	Summary . . . . .	60
<b>5</b>	<b>CS Application to Sum Frequency Generation</b>	<b>63</b>
5.1	Introduction . . . . .	63
5.2	SFG Theory . . . . .	65
5.3	Experiment Preparation . . . . .	67
5.4	Microscope instrumentation . . . . .	69
5.5	Results and Discussion . . . . .	73
5.6	Summary . . . . .	79
<b>6</b>	<b>CS Application to Hyperspectral Imaging and Endmem- ber Unmixing</b>	<b>82</b>
6.1	Introduction to Hyperspectral Imaging . . . . .	83
6.2	Traditional Hyperspectral imaging . . . . .	85
6.3	CS Hyperspectral Imaging . . . . .	86

6.3.1	Experiment Setup . . . . .	88
6.3.2	Experiment Results . . . . .	89
6.4	Hyperspectral Endmember Unmixing . . . . .	94
6.4.1	Introduction . . . . .	94
6.4.2	CS Unmixing Model . . . . .	96
6.4.3	Experiment Results . . . . .	99
6.5	CS Blind Unmixing . . . . .	107
6.5.1	Blind unmixing model . . . . .	107
6.5.2	Experimental Results . . . . .	109
6.6	Summary . . . . .	113
<b>7</b>	<b>Conclusions</b>	<b>114</b>
	<b>Bibliography</b>	<b>115</b>

## Illustrations

2.1	(a) original circuit board image. (b) 8-level wavelet decomposition. Black: significant coefficient, white: insignificant coefficient. (c) compressed image recovered with 10% wavelet coefficients . . . . .	15
2.2	CS formulation in linear algebra . . . . .	17
2.3	$64 \times 64$ reshaped Walsh basis functions (left column) and corresponding measurement patterns after permutation (right column)	21
2.4	original $256 \times 256$ -pixel cameraman image. . . . .	24
2.5	double-permuted Walsh-Hadamard pattern: (a)-(f) reconstruction results under 5%, 10%, 15%, 20%, 25% and 100% of the measurement data respectively. . . . .	25
2.6	normalized MSE versus the percentage of measurements under two cases: (a) noise free (b) Gaussian noise added. . . . .	26
3.1	(a) DMD chip; (b) scanning electron microscope image of micromirror [1]; (c) schematic of micromirror [2]. . . . .	29
3.2	Transmission spectra of three different DMD window materials. . . .	30
3.3	ALP mounted on a DMD1100 board . . . . .	31
3.4	Single pixel camera schematic . . . . .	33
4.1	(a) Forward biased p-n junction (b) Reverse biased p-n junction. [3] .	42

4.2	OBIC measurements under different lighting conditions: (a) raster scan with illumination power $P$ and optical power $P$ per pixel (b) CS and BS with with illumination power $NP$ and optical power $P$ per pixel (c) CS and BS with with illumination power $P$ and optical power $P/N$ per pixel. . . . .	44
4.3	Numerical simulation OBIC measurements, with $M = 128 \times 128$ resolution. Horizontal axis is SNR of acquired raster images (full $16K$ measurements). Vertical axis is SNR of CS (100 measurements). The optical power for the CS measurements is $\sqrt{N} = 128\times$ higher than the raster measurements. . . . .	48
4.4	Optical setup for OBIC and IR-PEM. (Light ray paths highlighted in three line styles: blue solid for OBIC measurement; blue dash for USB Camera imaging; red solid for IR emission) . . . . .	49
4.5	Image of DUT with (a) 100% illumination. (b) - (c) represent pixels in a $32 \times 32$ raster scan illumination pattern. (d) a $32 \times 32$ permuted Walsh-Hadamard illumination pattern. (e) a $64 \times 64$ permuted Walsh-Hadamard illumination pattern. . . . .	51
4.6	(a)-(f) OBIC CS reconstructions of $256 \times 256$ pixel image with different measurement ratio. . . . .	53
4.7	Normalized mean squared error of $256 \times 256$ OBIC reconstruction . .	54
4.8	OBIC CS reconstruction of a $1024 \times 768$ pixel image using 5% of the total measurements. . . . .	55
4.9	OBIC measurements of DUT with constant optical power per pixel, $256 \times 256$ resolution. (a) Image of the device. (b): CS measurements with 30% data. (f) Raster data with $10\times$ extra gain to boost SNR. .	56
4.10	OBIC measurements at constant total illumination power, $128 \times 128$ resolution. (a) raster scan (b) CS with 30% data. . . . .	56

4.11	(a)-(f) IR-PEM CS reconstructions of a $256 \times 256$ pixel image with different measurement ratio. . . . .	59
4.12	Normalized mean squared error of $256 \times 256$ IR-PEM reconstruction.	60
4.13	IR-PEM results. Left column: Images obtained by raster scanning for various sample resolutions; Right column: Images obtained by CS measurement for the same sample resolutions but at a compressed rate.	61
5.1	Optical microscope image of the gold pattern. . . . .	69
5.2	the sum frequency generation-compressive sensing imaging microscope.	70
5.3	Schematic diagram of SFG-CSI microscope setup . . . . .	71
5.4	A $32 \times 32$ -pixels SFG image of gold pattern reconstructed using 100% measurements. 200 laser pulses were averaged for each measurement. Signal from Au stripes was bright and signal from Si substrate was dark.	73
5.5	Effect of number of pulses/shots per random pattern on the quality of the SFG-CS images: reconstructed images and the corresponding measurement coefficients obtained with various number of shots, (a) 20 (b) 50 (c) 100 (d) 120 (e) 150 (f) 200. The images were recovered at a resolution of $32 \times 32$ pixels and 1024 patterns employed. . . . .	75
5.6	(a) Measurement coefficients averaged with various numbers of shots per pattern (b) Illustration of SNR change: standard deviation of the averaged measurements under 20, 50, 100, 120, 150 and 200 shots per pattern. The images were obtained at a resolution of $32 \times 32$ pixels and 1024 patterns employed. To get a clear comparison of the coefficients, some curves were offset in (a). . . . .	76
5.7	Number of pattern effect on quality of the reconstructed SFG images of the gold pattern. The image resolution was $32 \times 32$ and 200 shots per pattern were obtained and averaged. (a) 20%, (b) 40%, (c) 60%, (d) 80%, and (e) 100% of the total patterns. . . . .	78

5.8	Comparison of the quality of the SFG-CS images using various image resolutions applied to the DMD. 150 shots were acquired and averaged for each pattern applied to DMD. (a) SFG-CS image acquired and reconstructed at an image resolution of $32 \times 32$ pixels with 1024 patterns. (b) SFG-CS image acquired and reconstructed at an image resolution of $64 \times 64$ pixels with 4096 patterns. . . . .	79
5.9	. Comparison of the SFG images obtained using the novel CS and the traditional Raster method. (a) CS image at a resolution of $16 \times 16$ pixels (b) Raster scanning image at a resolution of $16 \times 16$ pixels (c) CS image at a resolution of $32 \times 32$ pixels (d) Raster scanning image at a resolution of $32 \times 32$ pixels. . . . .	80
6.1	The hyperspectral cube structure. [4] . . . . .	84
6.2	Traditional hyperspectral acquisition techniques: (a) whisk broom; (b) push broom; (c) filter wheel. . . . .	87
6.3	CS hyperspectral paradigm illustrated in linear algebra . . . . .	88
6.4	CS hyperspectral imaging setup . . . . .	89
6.5	A standard colorchecker: 18 color plus 6 gray patches. . . . .	90
6.6	Reconstructed spectral frames with 30% of total measurements . . . .	91
6.7	Spectrum of the illuminating light source . . . . .	92
6.8	(a) Montage of hyperspectral images with a lateral resolution of $256 \times 256$ pixels and a spectrum resolution of 4nm. The compression rate is 10:1. (b) Reconstructed image after summing up all the visible bands. (c) Camera image . . . . .	93
6.9	Comparison of $256 \times 256$ grey scale raster scan and CS reconstruction for two separate spectral bands . . . . .	94
6.10	"Color wheel" image under test. . . . .	101
6.11	Measured spectral signatures of the chosen endmembers. . . . .	101

6.12	Estimated abundance: CS unmixing solution from 10% measurements.	102
6.13	Six slices computed by CS unmixing model. . . . .	103
6.14	Six slices computed slice-by-slice using 2D TV algorithm TVAL3. . .	103
6.15	(a) Input spectral signatures added with Gaussian noise. (b) Reconstructed abundances: CS unmixing solution from 20% measurements. . . . .	105
6.16	(a) Input spectral signatures added with periodic noise. (b) Reconstructed abundances: CS unmixing solution from 20% measurements. . . . .	106
6.17	(a) Input spectral signatures added with impulsive noise. (b) Reconstructed abundances: CS unmixing solution from 20% measurements. . . . .	108
6.18	Measured spectral signatures of the chosen endmembers under white light LED illumination. . . . .	110
6.19	(a) Initial Guess of spectral signatures. (Cyan's signature is switched.) (b) Recovered spectral signatures. (c) Reconstructed abundances: CS blind unmixing solution from 20% measurement. . .	111
6.20	(a) Initial Guess of spectral signatures. (Arbitrary guess of cyan's signature) (b) Recovered spectral signatures. (c) Reconstructed abundances: CS blind unmixing solution from 20% measurement. . .	112

## Tables

6.1	HSL Values of Color Wheel. M: Magenta, Y:Yellow, C:Cyan . . . . .	100
-----	---	-----



## Chapter 1

### Introduction to Sampling Theorem

#### 1.1 Nyquist-Shannon Sampling Theorem

In early 19th century, French mathematician named Joseph Fourier proposed a complete frequency-domain description of continuous signals — Fourier series and Fourier transform, which states that any arbitrary signal can be represented as the sum of a series of sine and cosine functions. Later, with the need for digital instrumentation, the Fourier family has been enriched with discrete time Fourier series and discrete Fourier transform to work with sampled versions of signals in both time and frequency domains. By sampling, a continuous signal is approximated with a set of discrete values taken at equally spaced intervals. The Fourier sampling theorem tells us that if we take enough samples, in other words, if the interval is sufficiently small, the signal can be exactly reconstructed with no information loss. But the question is, "how many samples are enough?" In 1940s, Harry Nyquist and Claude Shannon developed a theorem which addresses that, to avoid aliasing, the sampling rate should be greater than twice the highest frequency of the input signal in order to be able to reconstruct the original back perfectly. This Nyquist-Shannon sampling theorem is the fundamental result of today's information theory, and has been widely used through the years to solve problems in mathematics, physics and engineering fields.

The Nyquist-Shannon criterion provides a sufficient condition for the sampling and reconstruction of a band-limited signal. Ideally, as long as the sampling rate reaches

the Nyquist rate, the interpolation algorithms can reconstruct the exact signal. However, due to the anti-aliasing, resolution and noise issues in practical applications, signal oversampling becomes an indispensable prerequisite. In general, the sampling rate needs to be several orders of magnitude higher than the Nyquist rate to produce a more accurate signal recovery. Nowadays, the design of analog-to-digital (A/D) and digital-to-analog (D/A) converters all follows this principle. Digital audio, for example, is usually sampled at a rate of 44.1KHz, as used by compact disk (CD). Therefore, the highest frequency of the recorded audio from the CD should not exceed 22.05KHz. A low pass filter is needed to block everything above 22.05KHz in order to remove the harmful aliasing frequencies. Since human ear can detect sound frequency from 20 Hz to 20KHz, signal shall be attenuated from 0dB at 20KHz to 90dB at 22.05KHz by an analog filter. This deep slope is difficult and expensive to realize and will cause phase shift problem, thus ends up poor sound quality. Instead, oversampling relaxes the anti-aliasing filter burden by raising the sampling frequency to  $2\times$ ,  $4\times$  or even  $8\times$  of 44.1KHz, such that filtering can be done in a sufficient broad transition band. Similar to one-dimensional signals, images will also suffer from aliasing problem if the sampling rate is inadequate. Take the CCD (charge-coupled device) or CMOS (complementary-symmetry metal-oxide-semiconductor) camera for example. Grids of pixels and underlying circuits convert the light signal into the electrical signal and digitize it with an A/D converter. To achieve the full resolution of the imaging system, CCD should have a sampling frequency at least twice the highest spatial frequency in the target image, which means that the pixel size must be less than half of the size of the diffraction limited or the Airy disk on the focal plane. In practice  $2.5\times \sim 3\times$  oversampling is used to compensate for the distance across the diagonal of the pixel and increase the resolution by interpolation reconstruction. The

higher the pixel density, the better the image is reproduced.

This Nyquist-Shannon sampling theorem has been quite successful in the history of digital signal/image processing. However, with the rapid development of digital revolution, this criterion will lead us to a dilemma. Faster sampling and processing rate, higher signal resolution, multi-dimensional data, as well as oversampling demands have brought a big pressure on the digital signal processing (DSP) hardware design and algorithms to accommodate the data deluge. Signal of Giga-Hz and image of Mega-pixel have generated huge amount of data for acquisition and processing. More importantly, to achieve additional requirements such as low energy consumption, high signal to noise ratio (SNR), great efficiency and low cost, more difficulties are imposed to the system design and manufacturing.

## 1.2 Compressive Sensing Theorem

To surmount the obstacles which traditional sampling method has met, a novel technology came into being. In 2006, D. Donoho, E. Candès, T. Tao and J. Romberg presented their initial results of compressible signal's recovery with highly incomplete set of data that does not satisfy the Nyquist-Shannon criterion [5–7]. Here "compressible" signal means that the signal can be sparsely represented in some domain with only a few big coefficients compared to its original resolution. Therefore, locating those significant coefficients and pursuing their values become the core problem. Instead of measuring the signal components uniformly in a local scheme, the signal is correlated with a series of sensing waveforms. These waveforms are so called sensing matrix or measurement matrix. For each measurement, it is a linear combination of randomly picked signal components, which may be important or not at all. However, embedded in these measurements is all of the critical information about the signal. In

a global sense, each signal element will be addressed at least once, such that no information will be missed even it is sampled much less times than what Nyquist-Shannon theorem has expected. By applying a nonlinear convex optimization algorithm, we can search for what the significant values are and where they are located.

Compressive Sensing theory is an evolution of the Nyquist-Shannon sampling theorem since the bound on the signal acquisition rate is highly reduced. The bandwidth in its initial domain (e.g. spatial, temporal) is not the determining factor of how fast or how dense the signal should be sampled. Instead, the intrinsic signal dimension or the essential signal bandwidth affects the sensing pace. For example, suppose a time domain signal has a frequency spectrum with the maximum frequency of 100MHz. But the big amplitudes only locate on a few frequency components. According to Nyquist criterion, the signal has to be sensed at least 200MHz. If it is undersampled, it introduces ambiguity between the significant frequency coefficients and harmful coherent aliases, which prevents unique reconstruction of the original signal. However, when the signal is instead randomly undersampled in a CS scheme, a sampling rate slightly greater than the number of significant frequency components would be sufficient for signal recovery. Thus, the demanding request for the A/D converter's sampling speed is greatly relieved. Similarly, in the 2D case, the number of pixels decides the number of measurements. So the physical design of sensors follows the array structure to uniformly map the scene on the focal plane. If one pixel is missing, the image won't be recovered due to information loss. Currently, with the rapid development of sensor production technology, higher and higher spatial resolution is achieved. However, this growth has encountered challenges. Given that the size of a sensor array is fixed, the only way to increase the spatial resolution is to reduce the pixel size. When the pixel size shrinks, the mean photon count at each pixel falls and

so does the Poisson variance of the photon signal. Thus, reducing pixel size inevitably increases image noise. To realize the high resolution imaging with a decent signal-to-noise ratio has become a hard issue for engineers to crack. Fortunately, the unique measurement procedure of CS offers a solution to this dilemma. The multiplexing mode measurement handles the linear combination of many pixels instead of one, so the light signal from the scene is maximally exploited with high efficiency. More importantly, image can be reconstructed with much fewer measurements than the total number of pixels which greatly saves acquisition time and data storage volume.

Notice that the CS theorem is based on the assumption that signal is sparse. If the sparsity is lacking, signal can not be recovered. However this priori information is not a rare case since all the common signals we are normally interested in capturing have such inherent structure. Natural signals such as sound, image and video all have this property in some known domain after the corresponding transform — Fourier, Wavelet, Curvelet, etc. The involvement of the concept "sparsity" in CS theory embodies the spirit of compression in signal acquisition. This is an initiative sensing scheme. Because compressible signal needs less essential information to be acquired than non-compressible signal, CS measurement directly extracts this information without wasting sampling rate on the inconsequential one. Clearly, the Shannon sampling scheme does not exploit the possibility that there is sparse structure in the signal. Instead, CS fully utilizes this and can sample and recover the signal at sub-Nyquist rate.

Sparsity is one crucial factor for CS. The other one is incoherence. The success of CS measurement relies on the design of sensing waveforms. In other words, measurement basis should be incoherent with the sparsity basis. No element of either basis can be sparsely represented in terms of the elements of the other one. Since

the signal structure is shown in the sparsity basis, the measurement basis should not match the signal structure at all. It turns out that the random noise-like matrices are universally incoherent with all the known sparsity bases. So they are the ideal choices of the sensing matrices. The details of sparsity and incoherence will be explained in Chapter 2.

CS changes the symmetry of traditional sensing system. The signal acquisition and reconstruction are traded off against each other. The sensing stage becomes computationally light and linear, while the signal recover requires non-linear processing and high CPU power. To reconstruct the original signal is like to solve an underdetermined equation, with information much less than the number of unknowns. This type of inverse problem has infinite solutions. However the restriction of sparsity helps to find the most optimized one, which is the sparsest solution. Its amplitude spectrum turns out to be the right significant components plus some low level random noises. By setting a threshold and amplitude correction, the original signal can be exactly recovered. Meanwhile, the size of the random noise is a function of the undersampling factor. The fewer samples acquired, the higher the noise level. Therefore, CS undersampling turns the Nyquist anti-aliasing problem into a much simpler denoising problem. As long as the sparse coefficients are above the noise level, they can be pursued and the original signal can be reconstructed. Researches are continually coming up with better and faster algorithms based on convex optimization.

In short, compressive sensing is a multidisciplinary theorem which involves statistics, information technology, sampling theory and optimization theory. Due to the advantages CS has brought in digital signal/image processing, this new field are drawing more and more attentions in both academia and industry. The history of compressive sensing has evolved a lot from pure mathematic theory to real application

and these two also stimulate one another for continued improvement.

### 1.3 Compressive Sensing for Imaging

As an important breakthrough in information theory, CS unique sensing and reconstruction mechanism offers a great opportunity to explore and discover the nature with better and smarter techniques. Guided by the theorem, a series of novel sensing frameworks have been realized and adapted from remote sensing, medical imaging and consumer photography to surveillance, machine vision and multimedia systems. These applications have and will benefit our lives in a deeper and wider way.

Our discussion in this thesis is mainly focused on the direct application of compressive sensing for imaging in 2D and 3D cases. The combination of CS with traditional optical imaging extends the physical capabilities and improves the performance of existing equipments and systems. First, we will start with the prototype of CS — single pixel camera.

#### 1.3.1 Single Pixel Camera

In traditional 2D digital photography, the field of view is recorded with a sensor array (CCD or CMOS), which is represented as a matrix in mathematics. Every sensor is responsible for a measurement of the light signal from one pixel of the scene. But in CS scheme, the signal received by the sensor is not the usual real-space sample anymore; instead it is a linear projection of light from all the pixels of the scene, which can be easily recorded with a single photodetector. A series of measurements are acquired according to a sequence of projections. So the spatial extent of sampling array is traded off with a sequential sampling over time. This is especially important and valuable for imaging areas where the 2D sensor array is either unfeasible or very

costly to manufacture.

Furthermore, for conventional imagers, as the spatial resolution increases, the signal intensity on each pixel drops quickly and might drop below the detection limit; however with CS, the sum of the intensity from almost half of all the pixels is measured each time no matter what the resolution is and therefore better signal to noise ratio is obtained even with lower gain and higher resolution compared to the traditional pixel imagers.

To implement the compressive sensing idea, we have constructed a prototype — single pixel camera. The random linear projections are realized by an optical modulator — digital micromirror device (DMD) from Texas Instruments. One mega tiny mirrors are built in a  $1\text{cm} \times 1\text{cm}$  area to manipulate the reflection direction of the incident light. Every mirror can be controlled and programmed to tilt in either  $+12^\circ$  or  $-12^\circ$ , which allows us to display the random pattern on the DMD. The light from the scene is first focused on the DMD, multiplexed by a random pattern, bounced back and finally captured with a photodiode. This process is repeated every time a new measurement pattern is displayed on DMD. The yielding photo-voltage values are imported to the nonlinear optimization algorithm and the original scene is reconstructed back. The setup and mechanism of single-pixel camera will be detailed in Chapter 3.

### 1.3.2 Circuit Failure Analysis

In traditional imaging, except for the 2D pixel-mapping technique, the raster scanning is also widely used, especially in the scientific research area. For example, confocal microscopy, two-photon excitation microscopy, laser scanning microscopy, Raman imagery and so on. Scanning technique is based on point illumination and point



detection. In other words, each time only one pixel is illuminated and the signal from the same pixel is recorded by a single detector. This technique is very useful to acquire low-light signal (anywhere from one to thousands of photons per second or per pulse), since varieties of sensitive and economical detectors are available, such as the vacuum tube photomultiplier tube (PMT) or the avalanche photodiode (APD).

However, this point-mapping approach still has limitations. First, signal to noise ratio of an image may suffer greatly with increasing resolution. If the illumination is constant, the higher the resolution, the less amount of signal acquired from a pixel. Since the detected signal intensity is proportional to the incident light power, increasing the illumination at each pixel might solve this problem. But the light power has to be limited to prevent optical damage and photo-bleaching to the sample. Furthermore, higher resolution means longer acquisition time. For an  $N \times N$ -pixel scene,  $N^2$  measurements are needed without exception.

To conquer the limitations, we include the CS idea in the conventional scanning microscopy and demonstrate the results in circuit failure analysis field. Traditional laser-based failure-analysis technique such as optical beam induced current (OBIC) involves scanning a focused laser beam across a sample by means of a laser scanning microscope (LSM). Instead, we use a CS-based OBIC measurements without requiring a laser or an LSM. The light source and a spatial light modulator create a series of pseudo-random on/off illumination patterns (structured illumination) on the device under test (DUT). The electrical signals (photocurrent) are produced in the silicon depletion region, converted to a voltage level by the transimpedance amplifier (TIA) and recorded by an analog to digital converter. We present reconstruction results from OBIC measurements on a discrete power transistor. We also demonstrate static IR photon emission microscopy (IR-PEM) images obtained using CS techniques in

which the light source is replaced with a single-element infrared photon detector so that no detector array is required. The detailed descriptions will be presented in Chapter 4.

### 1.3.3 Sum Frequency Generation

In surface science, sum frequency generation (SFG) is a powerful and versatile analytical technique to study the details of molecular structure and dynamics at surfaces. As a second-order nonlinear optical spectroscopy, the extremely high surface selectivity of the SFG is able to resolve the bonding, orientation and vibrational information of functional groups of molecules and ions at interfaces. The physical principle behind this surface selectivity is that the SFG is inherently blind to centro-symmetric bulk materials — gases, liquids, and isotopic solids, but is sensitive to places with low symmetry. At an interface between two materials, the inversion symmetry is broken, and the SFG optical signal can be generated and detected.

The conventional SFG imaging includes two techniques. First is based on the traditional laser scanning microscopy. Each time two laser beams (one visible and one IR) are focused on the same spot of the sample to stimulate the SF signal. The generated SF signal is then collected by a PMT photodetector. By scanning pixel-by-pixel over time, the spatial molecule/ions distribution of the entire surface area is achieved. This method needs special mechanical components to accurately control the scanning angles of both laser beams. It is also very inefficient and time-consuming, especially for higher resolution imaging. The second technique is 2D array acquisition. The laser beams are expanded to cover the whole area. The SF signal from all the pixels are recorded simultaneously using a greatly sensitive and costly CCD camera. Both the sample and the camera can remain stationary. However,

since the light intensity on every pixel is attenuated dramatically, the camera needs a long integration time to take an image with a decent SNR.

In Chapter 5, we present the construction of a new sum frequency generation imaging system using the CS technique. The SFG images of a gold pattern with stripes on silicon wafer are successfully acquired and reconstructed. Influence of number of pixels, number of pulses collected for each CS testing pattern, and the number of CS testing patterns on image quality are examined. The results also illustrate that SNR plays an important role on the quality of the reconstructed image and also on the minimum sampling rate required for an accurate reconstruction. A comparison of the traditional raster scan and CS is also made and the results clearly shows that raster scanning image produce unresolved image features at high resolution. This effect is due to signal dilution of tradition imaging. The weak raster scanning signal quickly drops below the detection limit of the detector as the number of pixel increases; while for CS, almost 50% of the signal is always detected, thus even for higher resolution it still maintains a good SNR.

#### **1.3.4 Hyperspectral Imaging**

Hyperspectral imaging, as a relatively new analytical technique, has drawn more and more attention in a wide field. By monitoring the interaction of electromagnetic radiation with matter as functions of wavelengths, the unique identification and classification of the substances can be realized due to their individual spectral signatures. However this important sensing method is limited by the scanning mode detection. To acquire the 3D hyperspectral data cube, raster scan is required, no matter with a scanning mirror in the X-Y spatial dimension or tunable spectral filter in the spectral dimension. This process is time consuming and very inefficient. Meanwhile, signal

to noise ratio of an image may suffer greatly with increasing resolution because the signal intensity from every scanning point is limited by the detector integration time. On the other hand, huge amount of data from every scene — normally hundreds of megabytes, need to be stored and processed before transmission, which brings heavy computation burden and programming complexity into the acquisition stage.

Chapter 6 is devoted to the extension of the single pixel camera to the hyperspectral imaging. The photo-sensing element is replaced with a spectrometer. Inside the spectrometer, incident light is diffracted by a reflective grating and focused onto a linear sensor array. Each sensor produces a photovoltage output for one random pattern. So the logged data corresponds to a spectrum (represented as a linear vector) for every measurement, with the length equal to the number of wavelength channels. Then each spectral slices are independently reconstructed and pile up together to form the 3D cube.

Typically, hyperspectral imaging is of spatially low resolution, in which each pixel from a given spatial element of resolution and at a given spectral band is a mixture of several different material substances, termed endmembers, each possessing a characteristic spectral signature. Hyperspectral unmixing is to decompose each pixel spectrum to identify and quantify the relative abundance of every endmember. Many linear mixing algorithms exist for determining endmembers based on the 3D hyper-cube. In our case, compressed hyperspectral data is first acquired with the CS hyperspectral imager. In the decoding side, a numerical procedure is performed to directly compute the abundance fractions of given endmembers, completely bypassing high-complexity tasks involving the hyperspectral data cube itself. Without the intermediate stage of 3D hyper-cube processing, we combine data reconstruction and unmixing into a single step of much lower complexity. We assume that the involved

endmember signatures are known and given, from which we then directly compute abundances. We also extend this approach to blind unmixing where endmember signatures are not precisely known a priori.

## Chapter 2

# Compressive Sensing Theory

Compressive sensing differentiates itself from the conventional sampling approaches by recovering certain signals and images from far fewer samples or measurements. The traditional sampling methods follow Shannon's theorem and the sampling rate must be at least twice the maximum frequency present in the signal. While for CS, depending on the sparsity of the sampling system, a fraction of the maximum frequency is required for sampling to retrieve the signal. To make this possible, CS relies on two principles: sparsity and incoherence

### 2.1 Sparsity

Most of the signals (sound, image, video, etc.) in nature possess an inherent structure, termed sparsity. Even if it is not directly revealed in the temporal or spatial domain, investigators have found various ways to highlight this sparsity by transforming to another domain, such as the frequency domain. In a proper basis there might be a large number of nonzero coefficients for the many of the real world signals or images. However, all but a few of the coefficients are large and the large coefficients carry most of the information of the signal. The signal can still be represented concisely by throwing away the small coefficients without much loss.

Sparsity, which has a long history of success in digital signal/image processing, considerably reduces the computational requirements and storage cost of data. So the



Figure 2.1 : (a) original circuit board image. (b) 8-level wavelet decomposition. Black: significant coefficient, white: insignificant coefficient. (c) compressed image recovered with 10% wavelet coefficients

fundamental problem is to look for a transformation that puts the most energy of the signal in the fewest transform coefficients. Currently, the design of dictionaries (e.g. DCT, Fourier, wavelet, curvelet, etc.) for sparse representations has led to extremely efficient compression methods, such as JPEG, MP3 and MPEG for image, audio and video data respectively.

Figure 2.1 shows an example of a sparse wavelet representation of a circuit board image [8]. Only a few coefficients in the transform domain are significant and located on the edge area of the image. Others are equal or close to zero. Through a wavelet transform, energy is concentrated in a relatively small number of components compared to the total number of pixels of the original image. We sort out the coefficients and discard those small ones. By using those big coefficients for reconstruction, image information is well preserved without much perceptual loss.

This demonstration also shows how traditional imaging works. We must acquire all the pixel signals first to execute a wavelet transform. For an  $n \times n$ -pixel scene,  $n^2$  samples are needed to avoid losing information. For example, CCD and CMOS

are widely used image sensors with an  $n \times n$  array of photoelectric detectors. Each detector represents one pixel of the image. The DSP chips behind the sensor collect all the data from CCD or CMOS, transform it in the wavelet domain and sort out the big coefficients. The whole process is done in the sensing stage, which is time and energy consuming when performing the complicated mathematical calculation. Since the images have the property of sparsity, with most transform coefficients insignificant and negligible, it appears redundant to acquire all the pixel values in the first place.

As an alternative, without starting with a potentially large number of samples  $N$  ( $N = n^2$ ), CS realizes an efficient method of signal acquisition by directly acquiring a condensed representation without going through the intermediate stage of acquiring all  $N$  samples. CS theory states that a signal can be recovered exactly from randomly undersampled data points if the signal exhibits sparsity in some transform domain [5–7]. A limited number  $M$  (where  $M \ll N$ ) of measurements carry and preserve the most essential information of the signal when reducing the dimension from  $\mathbb{R}^N$  down to  $\mathbb{R}^M$ .

## 2.2 Incoherent Projection

Assume that we acquire a real-valued, discrete signal  $x = [x_1, x_2, \dots, x_N]$  (for example, an  $N$ -pixel image) which can be represented in an orthogonal basis  $\Psi = [\psi_1, \psi_2, \dots, \psi_N]$ . Suppose the basis provides a  $K$ -sparse representation of  $x$ , then the signal can be expanded as a linear combination of  $K$  elements chosen from  $\Psi$

$$x_{N \times 1} = \Psi_{N \times N} \alpha_{N \times 1}. \quad (2.1)$$

or

$$x = \sum_{n=1}^N \psi(n) \alpha(n) = \sum_{l=1}^K \psi(n_l) \alpha(n_l) \quad (K \ll N). \quad (2.2)$$



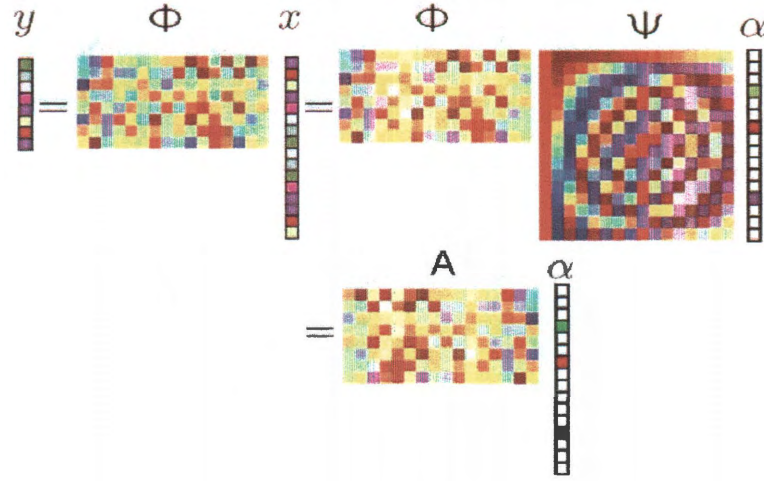


Figure 2.2 : CS formulation in linear algebra

Here  $\alpha$  is the transform coefficient vector with only  $K$  nonzero elements. To search for the  $K$  significant coefficients, the signal  $x$ , of dimensionality  $N$ , is first projected into a lower-dimensional basis function  $\Phi = [\phi_1, \phi_2, \dots, \phi_N]$  via

$$y_{M \times 1} = \Phi_{M \times N} x_{N \times 1} \quad (M \ll N), \quad (2.3)$$

where the inner product between the basis  $\Phi$  and signal  $x$  produces an  $M \times 1$  column vector  $y$  with every entry termed “a measurement” (see figure 2.2). Since the dimension of  $y$  is greatly smaller than that of the signal  $x$  ( $M \ll N$ ), recovery of  $x$  from the measurements  $y$  is an ill-posed inverse problem. However, the additional assumption of signal sparsity makes the recovery practical. Merging equation (2.1) and (2.3), we can write as

$$y_{M \times 1} = \Phi_{M \times N} x_{N \times 1} = \Phi_{M \times N} \Psi_{N \times N} \alpha_{N \times 1} = A_{M \times N} \alpha_{N \times 1}. \quad (2.4)$$

CS theory addresses that it is possible to construct a matrix  $A$  such that the sparse coefficients  $\alpha$  can be recovered from the measurements  $y$ . The sufficient con-

dition is the so-called restricted isometry property (RIP). Alternatively, to ensure  $A$  satisfies the RIP, the measurement matrix  $\Phi$  must be incoherent respect to the sparse representation matrix  $\Psi$  as much as possible, which requires that  $\phi_m$  can not sparsely represent the elements of  $\psi_m$  and vice versa [5–7].

A measure of mutual coherence of the two bases is given by

$$\mu(\Phi, \Psi) = \sqrt{n} \cdot \max(|\langle \phi_k, \psi_j \rangle|)_{1 \leq k, j \leq n}. \quad (2.5)$$

If  $\Psi$  and  $\Phi$  contain correlated elements, the coherence is large. Otherwise, it is small. For example, delta spikes are maximally incoherent with sinusoids. In particular, this incoherence holds with high probability between an arbitrary fixed basis (wavelet, curvelet, Fourier, etc.) and a randomly generated one, such as a matrix with independent identically distributed (i.i.d.) Gaussian ( $\phi_{ij} \in N(0, 1)$ ) or Bernoulli ( $\phi_{ij} = \pm 1$ ) with equal probability.

## 2.3 Signal Reconstruction

To recover the signal  $x$  from the  $M$  measurements  $y$ , there are two fundamental approaches for CS reconstruction. First is convex optimization, such as basis pursuit (BP) [6], fixed-point continuation (FPC) [9], gradient projection for sparse reconstruction (GPSR) [10], etc. The second is greedy search algorithm, which includes matching pursuit (MP) [11], compressive sampling MP (CoSaMP) [12], iterative hard thresholding (IHT) [13], and so on. Both of them have their own advantages. In general, the convex optimization approach has better reconstruction accuracy than the greedy search algorithm; while the latter has a less computational complexity.

In particular, the  $l_1$ -regularized convex optimization has attracted intensive research activities. It turns out that, if matrix  $A = \Phi\Psi$  has the RIP property and

the number of measurements  $M$  satisfies  $M \geq cK \log(N/K)$ , where  $c$  is a small constant, the original signal  $x$  can be reconstructed exactly from  $y$  with overwhelming probability by solving a constrained optimization problem

$$\min \|\Psi^T x\|_1 \quad \text{subject to} \quad y = \Phi x \quad (2.6)$$

in a noise-free case or

$$\min \|\Psi^T x\|_1 \quad \text{subject to} \quad \|y - \Phi x\|_2 \leq \varepsilon \quad (2.7)$$

when measurement noise exists.  $\varepsilon$  quantifies the noise level involved in the measurement  $y$ .

For image restoration, recent research [14–16] has confirmed that the use of total variation (TV) regularization instead of the  $l_1$  term in CS problems makes the recovered image quality sharper by preserving the edges or boundaries more accurately, which is essential to characterize images. We solve

$$\min TV(x) \quad \text{subject to} \quad y = \Phi x. \quad (2.8)$$

Here  $TV$  is the sum of the magnitudes of the discrete gradient at every point:

$$TV(x) = \sum_{ij} (|D_{h,ij}x| + |D_{v,ij}x|) = \sum_{ij} \|D_{ij}x\|_1 \quad (2.9)$$

$$D_{h,ij}x = \begin{cases} x_{i+1,j} - x_{i,j} & (i < N) \\ 0 & (i = N) \end{cases} \quad (2.10)$$

$$D_{v,ij}x = \begin{cases} x_{i,j+1} - x_{i,j} & (j < N) \\ 0 & (j = N) \end{cases} \quad (2.11)$$

The advantages of TV minimization stem from the property that it can recover not

only sparse signals or images, but also dense staircase signals or piecewise constant images. The experimental results presented in this thesis are reconstructed by the new efficient TV minimization scheme based on augmented Lagrangian and alternating direction algorithms — TVAL3 [17].

## 2.4 Pseudorandom Pattern

The design possibilities of the random matrix are extensive. In considering the hardware implementation, we have employed several pseudorandom patterns.

### 1. Mersenne Twister (MT):

MT is a pseudorandom number generating algorithm developed by Makoto Matsumoto and Takuji Nishimura in 1996 and 1997. The algorithm is coded into a C-source. By seeding a randomizer, a sequence of random numbers can be generated [18]. According to the parity, the entries of the pattern are set as +1 or -1, with the ratio of about 1:1. This method ensures the pattern randomness to a pretty high level. But CS reconstruction based on MT patterns is relatively slow and computationally expensive due to non-availability of a fast inverse transform. The whole  $M \times N$  measurement matrix has to be loaded in Matlab for calculation, which consumes large amounts of computer memory especially in high resolution imaging.

### 2. Walsh Hadamard Matrix:

We also exploit a double-permuted, sequence-ordered Hadamard matrix which contains only  $\pm 1$  entries. Each row of the matrix of order  $N$  is a Walsh function or Hadamard vector. By randomly permuting the rows and the elements in each row, a new measurement matrix  $\Phi_{N \times N}$  is formed. We take the first  $M$  rows

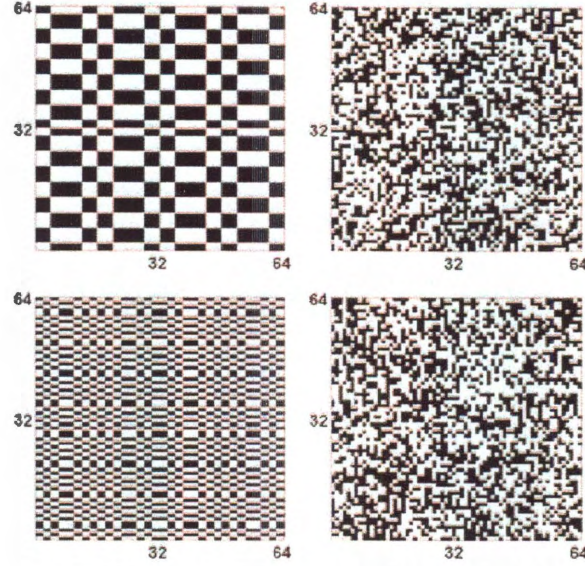


Figure 2.3 :  $64 \times 64$  reshaped Walsh basis functions (left column) and corresponding measurement patterns after permutation (right column)

$\{\phi_i, i = 1, \dots, M\}$  and reshape each one of them to a 2D matrix for the hardware operation. Some examples of  $64 \times 64$  reshaped Walsh basis function and the corresponding real measurement pattern after the permutation are shown in Figure 2.3. This double permutation insures to a great extent the necessary pattern randomness.

In mathematics, Walsh-Hadamard transform is an important tool because of its simplicity. It is a non-sinusoidal transform by addition and subtraction which is similar to Fourier series analysis, but uses square waves instead of sinusoidal waves. The Walsh-Hadamard matrix does not need to be stored in memory to perform the matrix-vector multiplication. It's fast transform and inverse transform guaranty a numerically efficient CS implementation.

### 3. Circulant Matrix:

A circulant matrix is a matrix whose columns, or equivalently rows, are circular permutations of one another. For example, it can take this form

$$\Phi_{\text{circulant}} = \begin{bmatrix} t_n & t_{n-1} & \cdots & t_1 \\ t_1 & t_n & \cdots & t_2 \\ \ddots & \ddots & \ddots & \ddots \\ t_{n-1} & t_{n-2} & \cdots & t_n \end{bmatrix}.$$

The last column is an vector  $\{t_i, i = 1, 2, \dots, n\}$ . The remaining columns are each cyclic permutations of the vector with offset equal to the column index. Similarly, the first row is the vector in reverse order, and the remaining rows are each cyclic permutations of the first row. Since circulant matrix is diagonalized by the Fourier transform

$$\Phi_{\text{circulant}} = F^* D F,$$

then we get

$$y = \Phi x = F^* D F x.$$

The matrix-vector multiplies is sped up through the fast Fourier transform (FFT), which improves the CS reconstruction speed.

This pattern generation approach is simple and convenient. All that is required is the seed vector or mother vector. We shift this vector left-to-right and up-to-down to generate all the others. Then each vector is reshaped into a 2D matrix/pattern for CS imaging implementation. Primary results have shown that circulant matrix is not only effective but also enable much faster decoding [19].

In short, from Mersenne Twister to Walsh-Hadamard patterns, the image reconstruction time is dramatically reduced. The computational efficiency is greatly improved as well. Our next step is to perform deeper investigations on circulant pattern. Its unique properties will surely enrich the CS family and benefit the practical imaging applications.

## 2.5 Simulation Results

To demonstrate the performance of the measurement basis (*Walsh-Hadamard*) and the sparsity basis (*gradient under the total variation operator*), Matlab simulated results are presented here. Synthesized measurement vector is created by multiplying the target image (Figure 2.4) with each row of the double-permuted Walsh-Hadamard matrix. There are altogether  $256^2$  elements in the vector, which comprise a complete set of measurement data for further analysis. Then we choose different percentage of this set of measurements for reconstruction. As shown, Figure 2.5(f) is reconstructed using all 100% measurements, while Figure 2.5(a)-2.5(e) is based on partial ones, from 5%, 10%, 15% to 20%, 25% respectively. Visually, the qualities of the recovered images keep improving with the increasing number of measurements, and more and more image details are shown up. However after 20%, no substantial improvement is observed.

Figure 2.6(a) plots the normalized mean squared error (MSE) versus the number of applied measurements. Here MSE is computed as

$$\frac{\sum_i [X_r(i) - X(i)]^2}{\sum_i X(i)^2}. \quad (2.12)$$

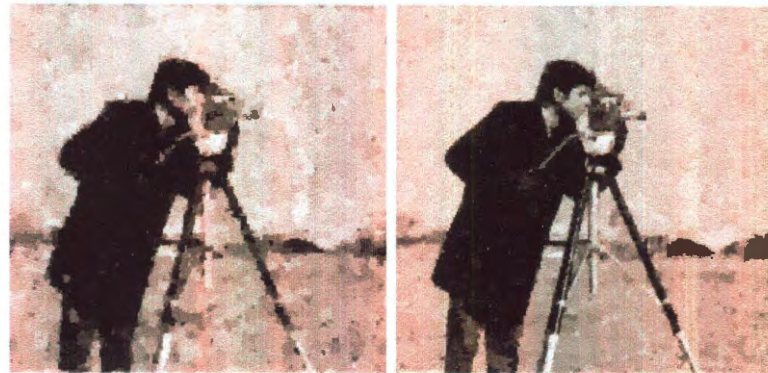
$X$  is the original image.  $X_r$  is the recovered one. The summations are across all the pixels. The MSE sharply decreases from 0.02 to 0.005 and then decays more



Figure 2.4 : original  $256 \times 256$ -pixel cameraman image.

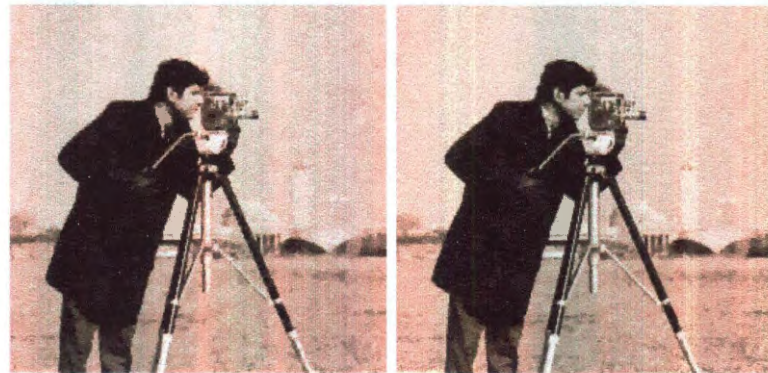
slowly afterwards. This trend shows that the number of measurements  $M$  reaches the sparsity level of the image at about 25%, which already contains abundant information to locate the big coefficients and recover the real space images. If the measurement data contains noise, the MSE curve shows the similar trend as in Figure 2.6(b).





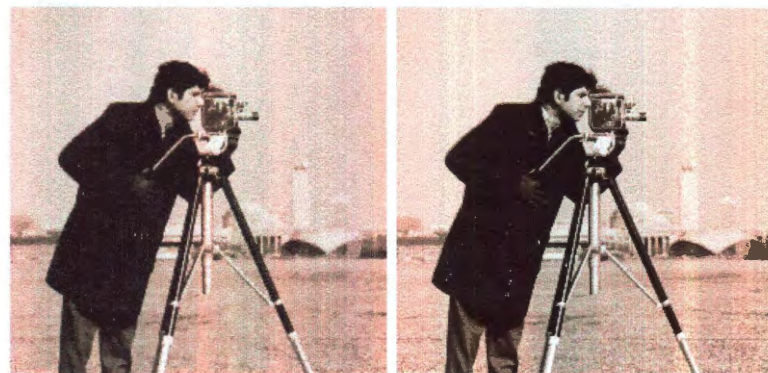
(a) 5%

(b) 10%



(c) 15%

(d) 20%



(e) 25%

(f) 100%

Figure 2.5 : double-permuted Walsh-Hadamard pattern: (a)-(f) reconstruction results under 5%, 10%, 15%, 20%, 25% and 100% of the measurement data respectively.

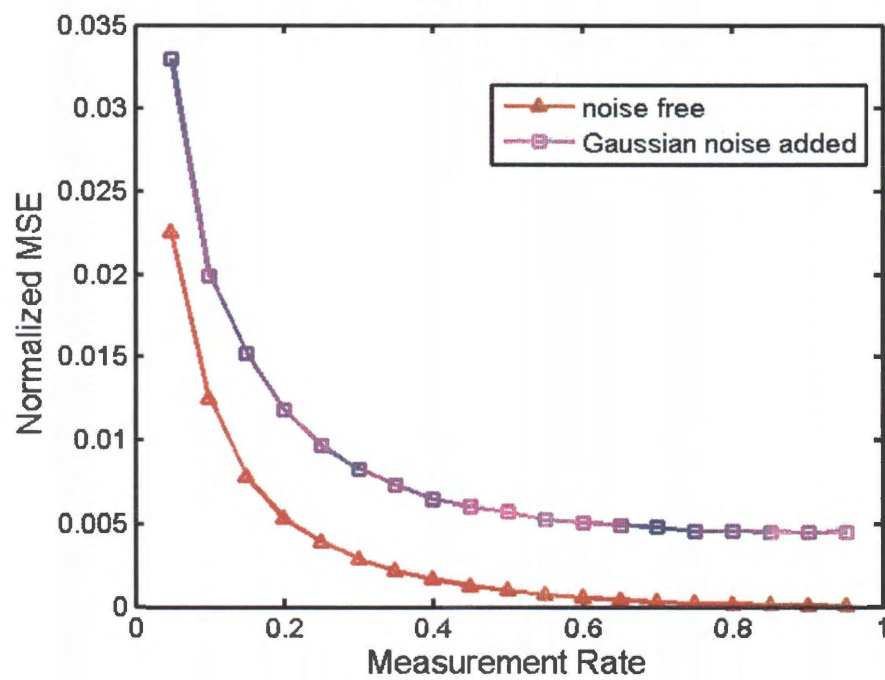


Figure 2.6 : normalized MSE versus the percentage of measurements under two cases: (a) noise free (b) Gaussian noise added.

## Chapter 3

### Single Pixel Camera

The implementation of compressive sensing to imaging is through the realization of random projections. Light signal from multiple pixels of the scene is combined into one signal output according to different random pattern. To realize the CS theory into real imaging system, a proper light modulator is required. It should have the capability to control the light transmission or reflection from a 2D plane. Furthermore, the frame rate of the modulation sequence has to be fast enough to adapt to the practical imaging application. Fortunately there exists a spatial light modulator called a digital micromirror device (DMD) (Texas Instrument) which is currently an ideal candidate for compressive imaging application because it processes high addressing speed, high contrast and a friendly digital interface.

### 3.1 Digital Micromirror Device

#### 3.1.1 introduction

DMD was invented by Larry Hornbeck and William Nelson of Texas Instruments (TI) in 1987. Till now, it has become one of the most successful commercial MEMS technologies in digital display industry and widely used in projector, HDTV and digital cinema. The unique properties and high standard performance make DMD even more attractive for many emerging applications, including holographic data storage, lithography, scientific instrumentation, and medical imaging.

As a spatial light modulation device, DMD creates high resolution and good quality images by modulating the light with microscopic mirrors (Figure 3.1(b)), with each of them looking like a “pixel” as in a CCD. Mirror orientation is controlled by underlying electronics as shown in Figure 3.1(c). The mirror is rigidly connected to a yoke which is connected by two mechanically compliant torsion hinges. Since each mirror is suspended above an individual static random access memory (SRAM) cell, according to which bit is loaded into the cell, a proper voltage is applied to the yoke address electrodes. The electro-static attraction forces the mirror to rotate until it comes to rest against mechanical stops. Therefore, mirrors can tilt and be positioned in one of two states— $+12^\circ$  (“on” state) or  $-12^\circ$  (“off” state) from horizontal; light falling on the DMD can be reflected in two directions depending on the orientation of the mirrors. So collecting light from one direction with lenses will produce gray scale images on the screen.

Due to the digital nature, we load binary numbers to every SRAM to control the mirror orientation and represent the gray levels of brightness. This technique is called binary pulse width modulation. The bit depth varies from 1 to 8, corresponding to gray scale values of 0 to 255. It is realized by varying the ratio of “on” verse “off” time of the mirror. Human eyes integrate the pulsed light to form a perception of desired intensity. For example, 1 bit/pixel means only binary patterns (“black” or “white”) can be displayed. One frame needs  $N$  bits to display ( $N$  is the total number of mirrors). For 8 bit/pixel, it takes  $N \times 8$  bits to store a frame. So, there is a strong trade-off between the frame rate, the gray level and the DMD resolution. For example, *Discovery<sup>TM</sup> 4100 0.7 XGA* DMD consists of a  $1024 \times 768$  array of electrostatically actuated micromirrors. It can display a sequence of binary XGA patterns at 32550 frames/sec or 8-bit gray scale patterns at 4068 frames/sec. *Discovery<sup>TM</sup> 4100 0.95*



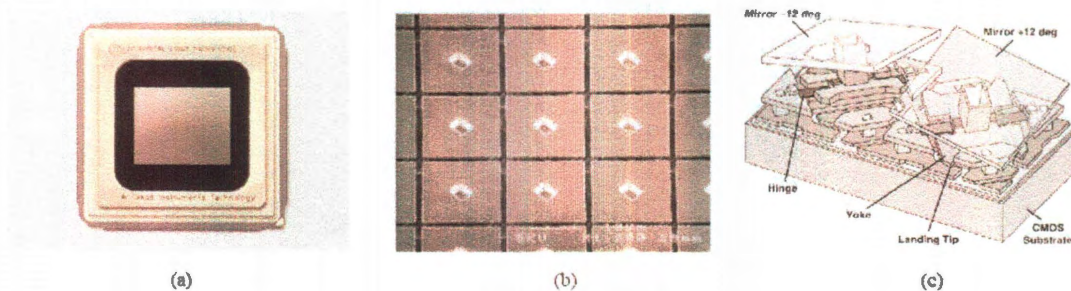


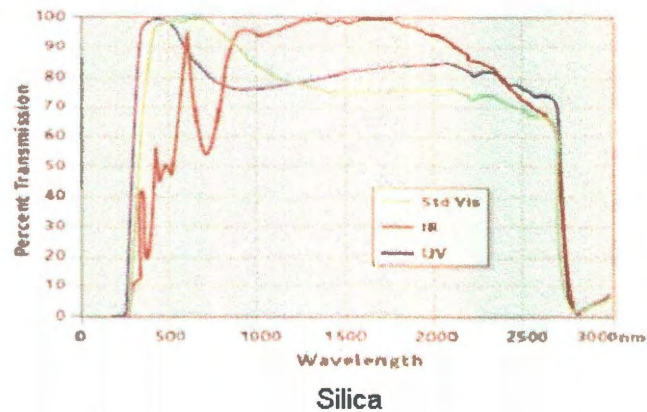
Figure 3.1 : (a) DMD chip; (b) scanning electron microscope image of micromirror [1]; (c) schematic of micromirror [2].

1080P DMD consists of a  $1920 \times 1080$  array of mirrors and displays a sequence of binary patterns at 24690 frames/sec.

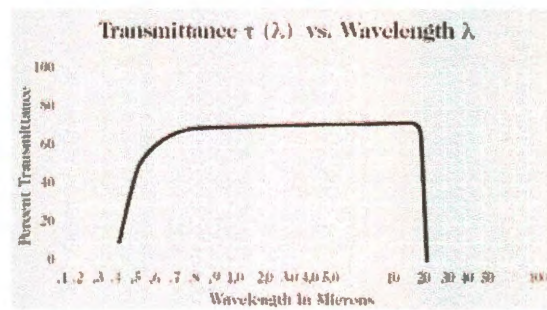
As a reflection light modulator, the micromirror is made of aluminum and the sealing glass window is coated with an anti-reflection layer. According to different applications, the window materials vary as needed to transmit in the waveband of choice from deep ultraviolet (UV) to long wave infrared (LWIR). Figure 3.2 shows the window transmission spectra of three materials — silica (three different coatings), Zinc Selenide and Barium Fluoride [20]. In DMD, light efficiency is maximized as a reflective device.

### 3.2 Light Modulator Package

The light modulator package (ALP) is the high speed controller of the DMD, which links the on-board memory with the DMD data lines. Due to the digital nature, DMD accepts binary numbers in the range of  $1 \sim 16$  bits to display time average grayscale levels. It is realized by varying the ratio of "on" versus "off" time of the mirror. Human eyes integrate the pulsed light to form a perception of desired intensity. Triggering options are provided in both directions. In the master mode, when



Silica



Zinc Selenide (ZnSe)

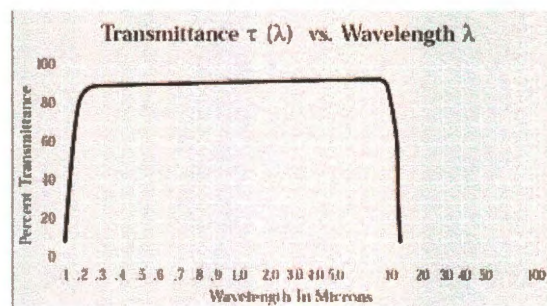
Barium Fluoride (BaF<sub>2</sub>)

Figure 3.2 : Transmission spectra of three different DMD window materials.

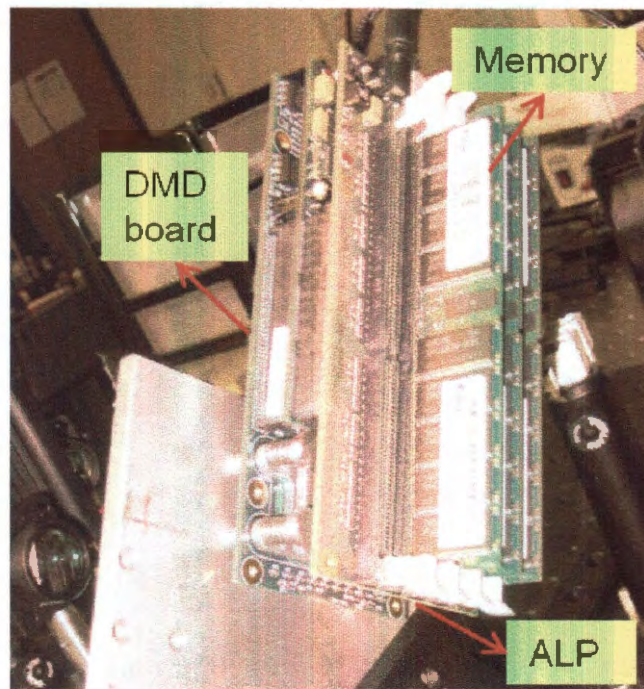


Figure 3.3 : ALP mounted on a DMD1100 board

the mirror flips, DMD sends out a pulsed voltage signal to trigger other devices, such as ADC or spectrometer. In the slave mode, DMD is triggered to display and switch patterns when an external pulsed signal is received.

A user friendly JAVA interface enables us to program the DMD and ALP for our needs. All the patterns are first loaded via USB from PC to the ALP memory(96Gbits). Once loaded, the frame sequences can be selected to be transferred to the DMD by a high speed FPGA and displayed on the mirrors. Parameters such as sequence time, illumination time, picture time and trigger delay are set separately without reloading the frame sequences. Figure 3.3 is the picture of our ALP mounted on a DMD1100.



### 3.3 Single Pixel Camera

#### 3.3.1 Architecture

Figure 3.4 shows a schematic of the optical setup of a CS application — the single-pixel camera. It is in essence an optical computer that randomly but controllably modulates the incident light from the target scene and sums it up to the output at the photodetector.

Light radiated or reflected from the object is first focused on DMD surface through a lens. By inputting a known random pattern  $\Phi$  to the DMD, the reflected light is modulated by the corresponding tilting angles of the micromirrors. Each mirror represents one element of the matrix  $\Phi$ . If  $\Phi$  is a binary pattern, then the  $+12^\circ$  mirror represents "1" and  $-12^\circ$  mirror represents "0". Light signal reflected from  $+12^\circ$  mirrors is collected with another lens and recorded with a photodiode. The resultant photo-voltage is a measurement of the projection or inner product between the scene and the random matrix  $\Phi$  displayed on DMD. We take a sequence of measurements corresponding to a sequence of patterns. Based on those measurements, the original scene can be reconstructed by our optimization algorithm.

To define the sampled image resolution, the micromirrors are divided into a number of blocks. Mirrors within one block are programmed to tilt in the same direction, with each block corresponding to a pixel. For example, by setting  $3 \times 3$  mirrors as one block,  $256 \times 256$  pixel imaging is performed; a  $24 \times 24$ -mirror block yields to a  $32 \times 32$  pixel imaging (use the center  $768 \times 768$  mirrors of DMD for display). This scheme can be additionally adjusted to control the field of view.



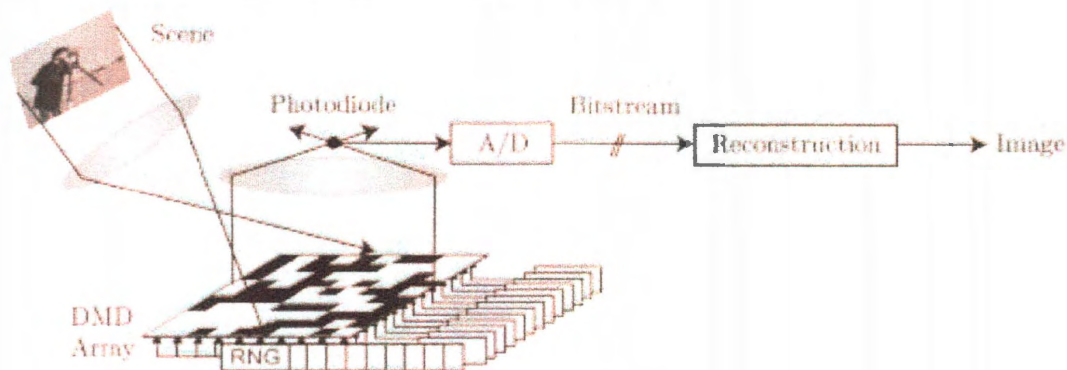


Figure 3.4 : Single pixel camera schematic

### 3.3.2 Multiplexing Methodology

The single-pixel camera is a flexible architecture to implement a range of different multiplexing methodologies. With the same setup, different acquisitions from the photodiode are reconstructed into original image based on corresponding multiplexing methods. In addition to the CS pattern, we also employed the raster scan and basis scan patterns on DMD to compare their performance.

- CS: A single sensor takes  $M$  measurements sequentially from different combinations of the  $N$  pixels as determined by random pattern  $\{\phi_m\}$ . Typically, we set  $M = O(K \log(N/K))$  which is  $\leq N$  when the image is compressible. In our analysis, we assume that the  $M$  rows of the matrix  $\Phi$  consist of randomly drawn rows from a permuted Walsh-Hadamard matrix. The acquired image is obtained from the measurements  $y$  via a sparse reconstruction algorithm such as TVAL3.
- Raster scan: Light signal from each pixel is acquired sequentially, starting in the

pixel on the top left corner, going from left to right, and then row by row from the top to the bottom of the image. This corresponds to test functions  $\{\phi_m\}$  that are delta functions and thus  $\Phi = I$ . The number of  $N$  measurements  $y$  directly provides the acquired image  $x$ . On DMD, it is accomplished by illuminating the entire active region and tilting a single mirror at a time towards the sample.

- Basis scan(BS): Similar to CS, a single sensor takes  $N$  measurements sequentially from different combinations of the  $N$  pixels as determined by patterns  $\{\phi_m\}$  that are a complete set of orthonormal bases, such as noiselet, DCT, Walsh-Hadamard, etc. The acquired image is easily calculated from the measurements  $y$  by  $x = \Phi^{-1}y$ .

Here we first conduct a theoretical analysis on the SNR which is a important factor to characterize the efficiency of the three methodologies. Experimental results comparison will be detailed in the following chapters.

We assume an image with  $N$  pixels and express it in a vectorized representation  $x = [x(1) \dots x(N)]^T$ . To measure the image, we shine a series of light intensity patterns  $\mathbf{a}_n = [a_n(1), \dots, a_n(N)] (n = 1, \dots, N)$ , which provides us with measurements

$$y(n) = \sum_{n'=1}^N a_n(n')x(n') = \mathbf{a}_n \mathbf{x}.$$

If we stack the  $N$  row vectors  $\mathbf{a}_n$  into a matrix  $\mathbf{A}$  of size  $N \times N$ , then this measurement process can be represented as the matrix equation  $\mathbf{y} = \mathbf{A}\mathbf{x}$ , where  $\mathbf{y} = [y(1) \dots y(N)]^T$ . We suppose the light power radiated from pixel  $m$  to be unity  $x(m) = 1$ , and assume variance of white noise  $\sigma$  is added to each obtained measurement  $y(m)$ ; by collecting the noise values into a vector  $\mathbf{x}_n = [x_n(1) \dots x_n(N)]^T$ , our measurements then correspond to  $\mathbf{y} = \mathbf{A}\mathbf{x} + \mathbf{x}_n$ . When  $\mathbf{A}$  is a basis (or more

generally a full rank matrix), an estimate of the image data is obtained as

$$\hat{\mathbf{x}} = \mathbf{A}^{-1}\mathbf{y} = \mathbf{A}^{-1}(\mathbf{A}\mathbf{x} + \mathbf{x}_n) = \mathbf{x} + \mathbf{A}^{-1}\mathbf{x}_n.$$

Thus the signal to noise ratio becomes for the estimate of the  $m^{th}$  pixel is

$$\text{SNR}(m) = \frac{|x(m)|}{|\hat{x}(m) - x(m)|} = \frac{|x(m)|}{|\mathbf{a}_m^{-1}\mathbf{x}_n|},$$

where  $\mathbf{a}_m^{-1}$  denotes the  $m^{th}$  row of the matrix  $\mathbf{A}^{-1}$ .

The Euclidean norm of the rows  $\mathbf{a}_m = [a_m(1) \dots a_m(N)]$  of the matrix  $\mathbf{A}$  is defined as

$$\|\mathbf{a}_m\| = \sqrt{\sum_{n'=1}^N a_m(n')^2},$$

for the different techniques; the SNR will be proportional to this norm.

- In raster scan, we set the matrix  $\mathbf{A}$  to the identity so that only one pixel is measured at a given time. The row  $\mathbf{a}_m = [0 \ 0 \ \dots \ 0 \ 1 \ 0 \ \dots \ 0 \ 0]$ , with the 1 at index  $m$ . In this case,  $\mathbf{a}_m^{-1}\mathbf{x}_n = x_n(m)$  and the SNR becomes

$$\text{SNR}_{\text{raster}}(m) = \frac{|x(m)|}{|x_n(m)|} = \frac{1}{\sigma}.$$

- In basis scan, we set the matrix  $\mathbf{A} = \mathbf{W}$ , where  $\mathbf{W}$  is the Walsh matrix with entries 1 and -1. The row  $\mathbf{a}_m$  corresponds to the  $m^{th}$  Walsh pattern. The matrix  $\mathbf{B} = \mathbf{A}^{-1}$  will have entries  $b_m(n')$  of magnitude  $\frac{1}{N}$ , and so the expected value of

the denominator of the SNR is

$$\begin{aligned}
E[|\mathbf{a}_m^{-1} \mathbf{x}_n|] &= E[|\mathbf{b}_m \mathbf{x}_n|] = E\left[\left|\sum_{n'=1}^N b_m(n') x_n(n')\right|\right], \\
&= \sqrt{E\left[\sum_{n'=1}^N b_m(n')^2 x_n(n')^2\right]}, \\
&= \sqrt{\sum_{n'=1}^N b_m(n')^2 E[x_n(n')^2]}, \\
&= \sqrt{\sum_{n'=1}^N b_m(n')^2 \sigma^2}, \\
&= \sigma \sqrt{\sum_{n'=1}^N b_m(n')^2}, \\
&= \frac{\sigma}{\sqrt{N}}.
\end{aligned} \tag{3.1}$$

So we obtain in expectation that

$$\text{SNR}_{\text{basis}}(m) = \frac{\sqrt{N}}{\sigma}.$$

This shows that basis scan outperforms raster scan in SNR by a factor of  $\sqrt{N}$ .

- In CS, the measurements follow the same formulation as in basis scan. CS recovery introduces an amplification in the noise power by a constant  $C_n$ , which has been shown experimentally to be approximately 4 [21]; thus we can say roughly that

$$\text{SNR}_{\text{CS}} = \frac{\sqrt{N}}{2\sigma},$$

where now we refer to the SNR averaged over the entire image. The advantage of CS over basis scan is that we only need  $M \ll N$  measurements. Thus the acquisition time is reduced by a factor  $M/N$ , which could be 10x or more depending on the image. For further discussion of basis scan and CS theory, see refs [22, 23].

### 3.3.3 Advantages

In summary, the traditional sampling process wherein massive data is first acquired and then discarded to facilitate storage and transmittance is extremely wasteful. Compressive sensing brings about a smart and efficient method of signal acquisition with two steps: random compressed measurements and nonlinear recovery. It directly acquires the important information of the signal with highly condensed measurements. Signals from the pixels are linearly projected to one output/measurement. A sequence of measurements is acquired by changing the projection pattern. The 2D spatial system is transformed to a 1D spatial plus temporal system. The compression inherent in compressive sensing also reduces the time duration, which enables the real application of imaging with a single-pixel detector. Random projection is a universal encoding strategy because it is incoherent with any fixed sparsity basis. Using the same random measurements, a decoder can recover the signal under any sparse basis according to different applications. If a sparser representation is proposed in the future, the same measurement data can be used for reconstruction with even higher quality.

The simple optical engine structure, robust measuring method and high speed acquisition makes compressive sensing-based single pixel camera a strong competitor to traditional imaging systems. Data acquisition and compression are combined into one step. There is no computation involved in the sensing stage. All the computational complexity is passed to the receiving end, which always contains sufficient computer processing power. The sensing stage requirement is pushed to the simplest and cheapest level. Moreover, one detector instead of detector arrays enables more applications, such as IR imaging with an InGaAS photodiode, low light imaging with PMT (Photomultiplier Tube) or APD (Avalanche Photodiode), hyperspectral

imaging with a spectrometer and so on. More details will be discussed in the next chapter.

## Chapter 4

### CS Application to OBIC and IR-PEM

Laser scanning microscopy is a vital technique for studying function and process in micro-structure. Its basic working principle is to focus laser light with objective lens on a spot on the focal plane within the specimen and scan over it in a pixel-by-pixel manner. The contrast of an image may come from reflection, transmission, fluorescence, Raman, nonlinear harmonics signals, photocurrent, etc. Because of the monochromaticity, narrow linewidth, low divergence and strong power, laser as the light source has its own priority in low light imaging and confocal microscopy.

This traditional sequential point mapping approaches require an additional incorporation of a sample positioning stage or scanning mechanics, such as galvanometer-driven mirrors [24] and acousto-optic deflectors [25], to address every pixel precisely and repeatedly. The data acquisition time, signal to noise ratio and spatial resolution couple strongly and combine to limit the effectiveness of such a technique. The higher the resolution, the less signal that is received by the detector per measurement, and thus the more integration time needed to accomplish the scanning. However, the single-detector configuration is still extensively used due to the relatively low cost and great diversity of individual detectors.

In our work, we proposed a new microscope system based on the idea of compressive sensing, which outperforms the conventional microscopy from both acquisition time and SNR. Instead of illuminating the pixel one-by-one uniformly, a structured illumination is created. It is realized by modulating the light source with a series

of pseudo-random patterns before it reaches the device under test (DUT). The resulting signal from the DUT (e.g. photo-current, photo-resistance) is recorded and reconstructed for the entire imaging area. Meanwhile, the single element detection preserves the advantages of simple optical structure and versatile detector choices. We will demonstrate this microscope's performance in the field of circuit failure analysis in the following sections.

## 4.1 Introduction

In today's semiconductor industry, devices are becoming more and more miniaturized and complex. Transistors, diodes, capacitors, resistors and their interconnections are all assembled into a small integrated circuit (IC) chip, which is generally microscopic in size. Due to this high integration, high density and high functionality, failure causes and mechanisms are also complex. Therefore, it is important to analyze failed devices, clarify failure modes and mechanisms, and provide feedback to improve the manufacturing and design processes.

Semiconductor failure analysis (FA) involves a number of different techniques, such as X-ray radiography, curve tracing, scanning acoustic microscopy (SAM), scanning electron microscopy (SEM), Optical Beam-Induced Current (OBIC), Photon emission microscopy (PEM), microthermography (Hot Spot Detection), auger emission spectroscopy (AES), focused ion beam analysis, etc. Each technique provides its own specialized information and contributes to arrive at an accurate determination of the cause of failure. In this chapter, we illustrate CS applications to two FA techniques — OBIC and IR-PEM.



#### 4.1.1 OBIC

OBIC is a photovoltaic effect which is used to locate electrically active defects such as diffusion, stacking faults, latch-up and leakage in IC chip. OBIC images are produced by monitoring the nonrandom recombination current of the electron-hole-pairs generated by a laser as it is scanned across the chip surface. If the excitation photon energy exceeds the smallest band gap, the photon absorption effect will provide the electron with enough energy to overcome the band gap and jump to the conduction band. It will produce many free electron-hole pairs. These pairs usually recombine randomly in the material; however, if production occurs in a depletion region, the charge carriers will be separated by the junction potential before recombination producing an OBIC signal. The variations in current produced by the laser beam as it scans the sample are converted into variations in contrast to form the OBIC image, which represent the circuit chip's properties.

OBIC is an efficient and non-invasive optical analysis technique in detecting and localizing certain IC failures. First, it requires little in the way of sample preparation. Second, since OBIC introduces no charge into the circuit, it causes no damage. Last, no external bias or circuit is needed to observe a signal. Due to these advantage, applications of OBIC range from detection of diffusion region and defective junction to gate oxide short, etc.

#### 4.1.2 PEM

PEM is widely used for circuit failure analysis as a defect localization tool. When an electron transits from a higher energy state to a lower one, the energy difference is emitted as electromagnetic radiation. If the excitation source is due to electrical stimulation, the radiative transition is also termed electroluminescence.

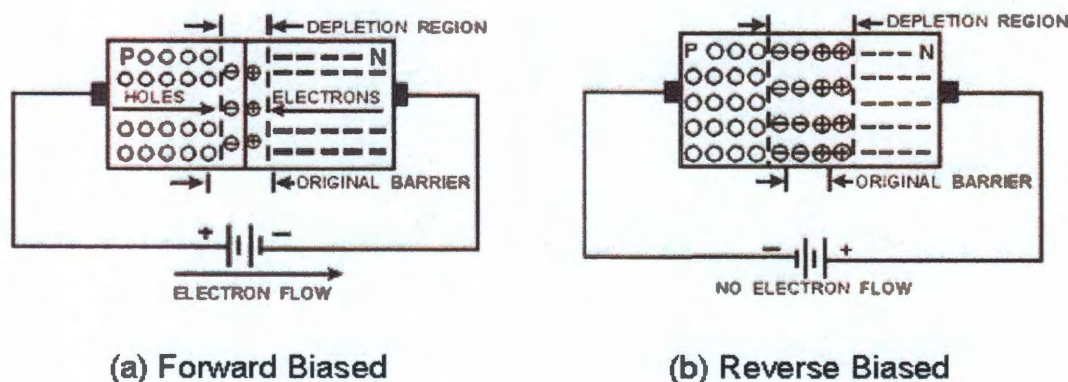


Figure 4.1 : (a) Forward biased p-n junction (b) Reverse biased p-n junction. [3]

In silicon chip, photon emission from the defect area generally falls into four categories: forward or reverse biased p-n junctions (Figure 4.1), transistors in saturation, latchup, and gate oxide breakdown. When a forward biased voltage is applied to a p-n junction, N-type majority carriers, electrons, move from the N-type material towards the P-type material. P-type majority carriers, holes, move towards the N-type material. The emission is generated by inter-band electron-hole recombination near the junction area. The energy of the emitted photon is near the bandgap of silicon (1.12eV), and the corresponding wavelength of the photon is near 1107nm. When a reverse biased voltage is applied to a p-n junction, majority carriers are attracted away from the junction. The positive terminal attracts electrons away from the edge of the barrier on the N side. The negative terminal attracts holes away from the junction barrier on the P side. This increases the width of the nonconducting depletion barrier. There is no recombination of majority carriers. Only a small current flows due to minority carriers. But the reverse bias creates a substantial electric field in the depletion region. As the reverse bias increases, the electric field increases as

well. Once its intensity is beyond a critical level, the p-n junction will break down and generate photons from the recombination of carriers whose energies is significantly above the bandgap energy. The resulting emission spectrum will extend into the visible wavelength, varying from 400nm to 1100nm.

## 4.2 SNR Analysis

Conventional OBIC imaging requires laser as the scanning light source. One reason is that the size of the beam spot decides the resolution of the image. Another reason is the signal-to-noise ratio. Since the photocurrent signal is proportional to the illumination power, stronger light source excites more current which brings higher SNR in the measurement. The standard approach to OBIC is the time-tested raster scan by stepping the laser beam to each pixel sequentially. If the laser beam has power  $P$ , then the optical illumination power on each pixel is also equal to  $P$ , as shown in Figure 4.2(a). The alternatives to the raster scan are the basis scan and CS measurement. In basis scan, the entire die is illuminated with a series of patterns that comprise a complete basis set. If there are  $N$  pixels, then  $N$  patterns are required. In CS, one uses not a complete set of basis functions but a smaller set of random illumination patterns. This is advantageous because the theory of CS tells us that if our imagery is compressible, then we can take many fewer random measurements than the number of raster-scanned pixels or basis-scan functions. If there are  $N$  pixels in the image, then typically we can make  $M$  measurements, where  $M/N$  is on the order of 10% or less, with only a small SNR penalty compared to basis scan. This is analogous to the familiar JPEG compression of images — although the compression is lossy, most of the information in the image is retained even though the file size is much smaller than the original.

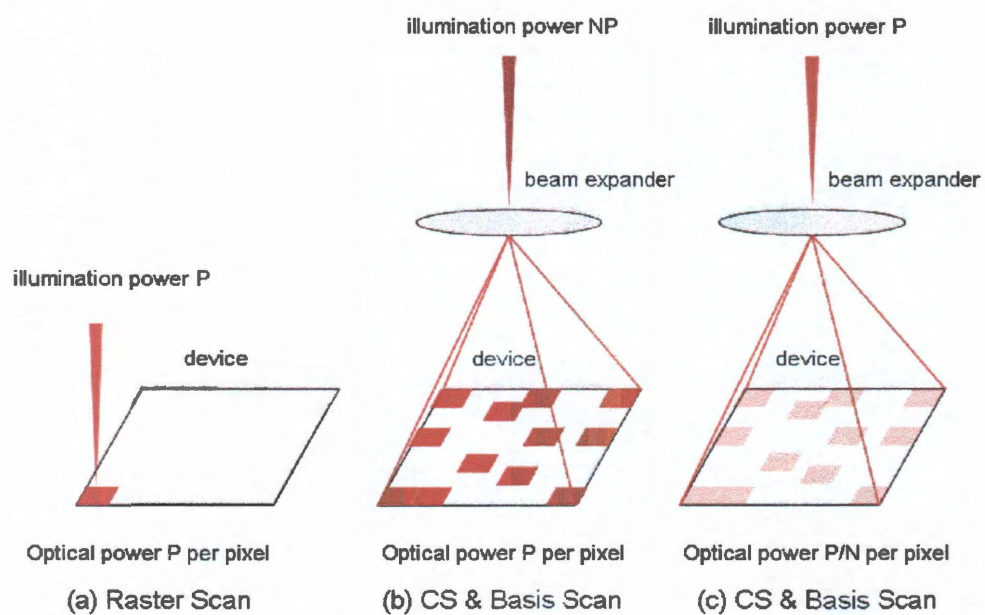


Figure 4.2 : OBIC measurements under different lighting conditions: (a) raster scan with illumination power  $P$  and optical power  $P$  per pixel (b) CS and BS with illumination power  $NP$  and optical power  $P$  per pixel (c) CS and BS with illumination power  $P$  and optical power  $P/N$  per pixel.

Since basis scan and CS don't require a low divergence light source, normal lamps or LEDs can be utilized for illumination. So as an updated version of SNR analysis in Chapter 3, we illustrate the OBIC SNR comparison among raster, BS and CS in two different lighting conditions. The schematics of them are presented in Figure 4.2(b) and 4.2(c).

1. Total illumination power  $P$ :

- In raster scan, we set the matrix  $\mathbf{A} = P \cdot \mathbf{I}$ , where  $P$  is the optical power and  $\mathbf{I}$  is the identity matrix. The row  $\mathbf{a}_m = [0 \ 0 \ \dots \ 0 \ P \ 0 \ \dots \ 0 \ 0]$ , with the  $P$  at index  $m$ . Then  $\mathbf{a}_m^{-1} \mathbf{x}_n = x_n(m)/P$ , and the SNR becomes

$$\text{SNR}_{\text{raster}}(m) = \frac{|x(m)|}{|x_n(m)|} = \frac{P}{\sigma}. \quad (4.1)$$

- In BS and CS, the laser is expanded and uniformly cover the whole DMD area, with optical power  $P$  distributed equally among the  $N$  pixels. we set the matrix  $\mathbf{A} = \frac{P}{N} \cdot \mathbf{W}$ . The row  $\mathbf{a}_m$  corresponds to the  $m^{\text{th}}$  Walsh pattern has entries  $-P/N$  and  $P/N$ . The matrix  $\mathbf{B} = \mathbf{A}^{-1}$  will have entries  $b_m(n')$  of magnitude  $\frac{1}{P}$ , and so the expected value of the denominator of the SNR is

$$\begin{aligned} E[|\mathbf{a}_m^{-1} \mathbf{x}_n|] &= E[|\mathbf{b}_m \mathbf{x}_n|] \\ &= \sigma \sqrt{\sum_{n'=1}^N b_m(n')^2}, \\ &= \frac{\sigma \sqrt{N}}{P}. \end{aligned} \quad (4.2)$$

The SNR becomes

$$\text{SNR}_{\text{basis}}(m) = \frac{P}{\sigma \sqrt{N}}, \quad (4.3)$$

$$\text{SNR}_{\text{CS}} = \frac{P}{2\sigma\sqrt{N}}. \quad (4.4)$$

In this case, the raster scan technique outperforms CS by a factor around  $2\sqrt{N}$ .

2. Optical power  $P$  per pixel:

- In raster scan, it stays the same SNR,

$$\text{SNR}_{\text{raster}}(m) = \frac{|x(m)|}{|x_n(m)|} = \frac{P}{\sigma}.$$

- In the basis scan, with optical power  $P$  per pixel, the total optical power is  $NP$ . We set the matrix  $\mathbf{A} = P \cdot \mathbf{W}$ . The matrix  $\mathbf{B} = \mathbf{A}^{-1}$  will have entries  $b_m(n')$  of magnitude  $\frac{1}{NP}$ , and so the expected value of the denominator of the SNR is

$$\begin{aligned} E[|\mathbf{a}_m^{-1} \mathbf{x}_n|] &= E[|\mathbf{b}_m \mathbf{x}_n|] \\ &= \sigma \sqrt{\sum_{n'=1}^N b_m(n')^2}, \\ &= \frac{\sigma}{P\sqrt{N}}. \end{aligned} \quad (4.5)$$

So we obtain in expectation that

$$\text{SNR}_{\text{basis}}(m) = \frac{P\sqrt{N}}{\sigma}, \quad (4.6)$$

$$\text{SNR}_{\text{CS}} = \frac{P\sqrt{N}}{2\sigma}. \quad (4.7)$$

In this case, CS is superior by a factor of about  $\sqrt{N}/2$  compared to raster scan.

Figure 4.3 shows numerical simulations of the relative scaling of SNR for CS vs. raster-scanned images. A series of  $128 \times 128$  images with up to 10 nonzero data points was used. The amplitude of each nonzero point within an image was set to 1, 10, 100, or 1000. Gaussian noise of RMS value 1 was then added. Each image was reconstructed with raster scan (using the full 16K measurements) and CS (using 100 measurements) and the expectation value of the SNR, averaged over the entire image, was calculated. The CS measurements used 128 times as much total illumination power incident on the sample as the raster measurements; in this limit the SNR values are approximately equal as expected, over a range of about 3 orders of magnitude.

Interestingly, for low SNR and small number of nonzero pixels, the CS measurement performs somewhat better than raster. This is because the CS technique only required 100 measurements (vs. 16K for raster) and so the signal was extracted without adding in an enormous number of noise measurements. At higher SNR and higher number of nonzero pixels, the raster scan shows some improvement over the CS. This is due to the heavier weighting of the high-signal pixels when averaged over the whole image. In the high-SNR regime either image would be sufficiently clean to be useful, but the CS measurement in this (extremely sparse) case required less than 1% of the measurements required for the raster scan.

### 4.3 Experimental Setup

To demonstrate compressive sensing's application in failure analysis related to OBIC and IR-PEM, we constructed a simple but robust platform. As shown in Figure 4.4, according to the two reflection angles of the DMD, the setup was divided into two parts to acquire the OBIC and IR emission data separately.



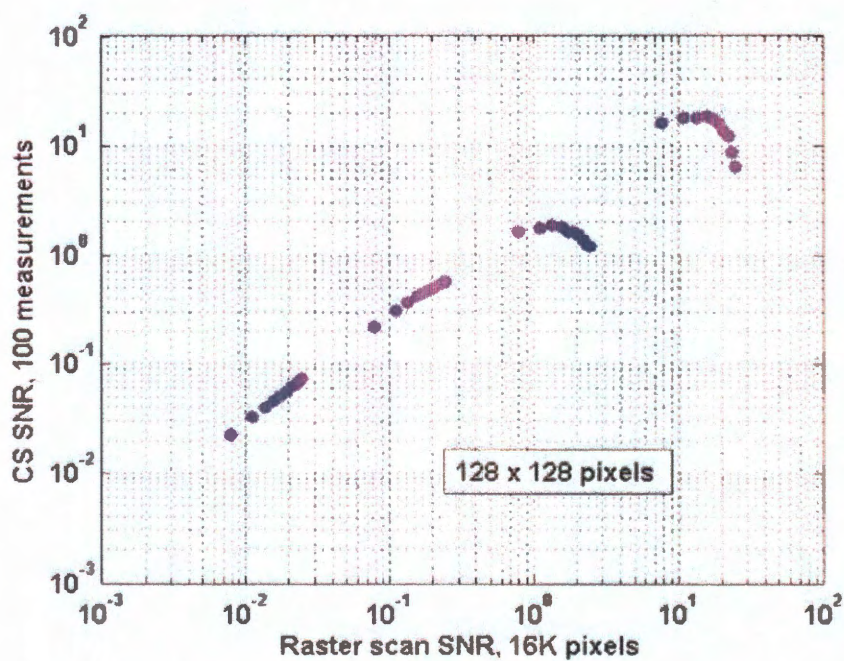


Figure 4.3 : Numerical simulation OBIC measurements, with  $M = 128 \times 128$  resolution. Horizontal axis is SNR of acquired raster images (full 16K measurements). Vertical axis is SNR of CS (100 measurements). The optical power for the CS measurements is  $\sqrt{N} = 128\times$  higher than the raster measurements.



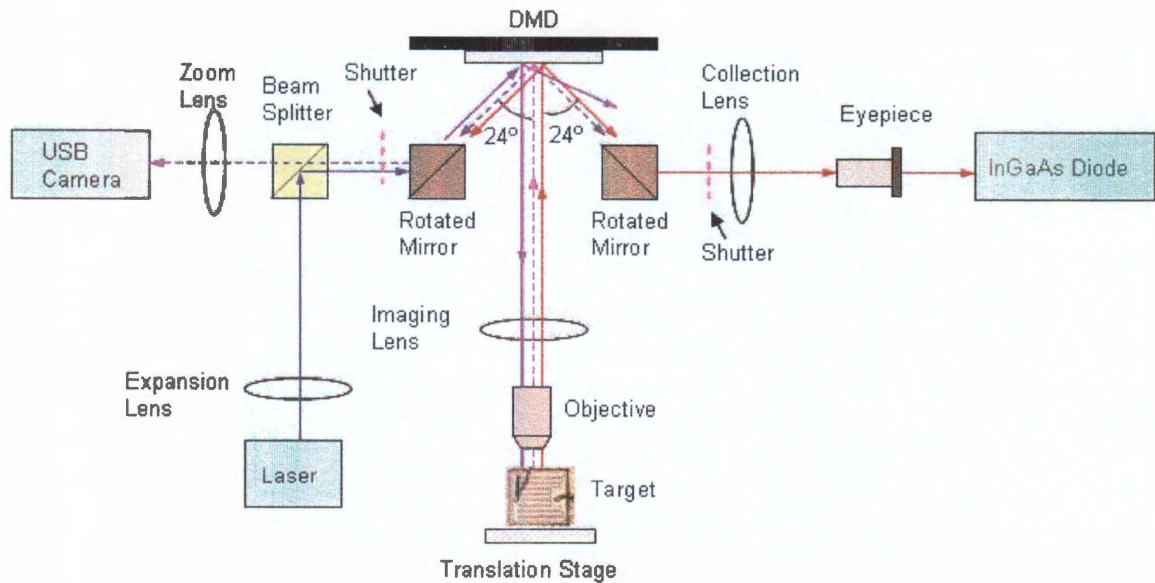


Figure 4.4 : Optical setup for OBIC and IR-PEM. (Light ray paths highlighted in three line styles: blue solid for OBIC measurement; blue dash for USB Camera imaging; red solid for IR emission)

The left arm contained a light source which was expanded and collimated onto DMD to cover the whole  $\sim 1\text{cm}^2$  mirror array area. The DUT was placed on the optical conjugate plane of DMD, such that the structured illumination on the DUT matched the digital illumination pattern applied to the DMD. A USB camera helped to visualize and focus the DUT while justifying the position of the translation stage.

The right arm was devoted to IR signal collection. The detector was a commercial TE-cooled InGaAs photodiode from Hamamatsu. The DUT was a discrete power transistor in a TO-3 package with the cap removed. The base emitter junction of the DUT was forward-biased, causing emission due to electron-hole recombination.

The infrared light emitted by the DUT was first imaged onto DMD. The modulated intensity patterns reflected by the DMD were collected by the photodiode and then digitized.

Once the optical system is focused, the two different measurements are both available. Since DMD always has light reflected in two angles, during OBIC measurements, we closed the shutter on the right arm in case the ambient light reached the photodiode. Similarly, in emission acquisition, the left shutter was closed. Also note that, the applied patterns on OBIC and IR emission are simply inverted versions of each other, which means one is displaying the pattern  $\{\phi_m\}$  while the other is displaying  $\{1 - \phi_m\}$ . Thus, the reconstruction process is the same for both.

In addition to the known random patterns, we also displayed a raster scan pattern on the DMD and compared the experimental results of the two different acquisition methods. The sequential raster scan was accomplished by illuminating the entire DMD and tilting a single mirror-pixel at a time towards the sample. The representative illumination patterns on the DUT are shown in figure 4.5. Notice that figure 4.5 (b)-(c) both have one block of black area (one pixel) which is addressed independently.

## 4.4 Experimental Results

### 4.4.1 OBIC Results

First we employed a 3mW He-Ne laser as the illumination light source to acquire and reconstruct the OBIC signals. The DUT was a discrete PNP power transistor (NTE219) with the base and emitter terminals connected to a TIA. The OBIC signal from the DUT was converted to a voltage level by the TIA and recorded by an analog to digital converter.

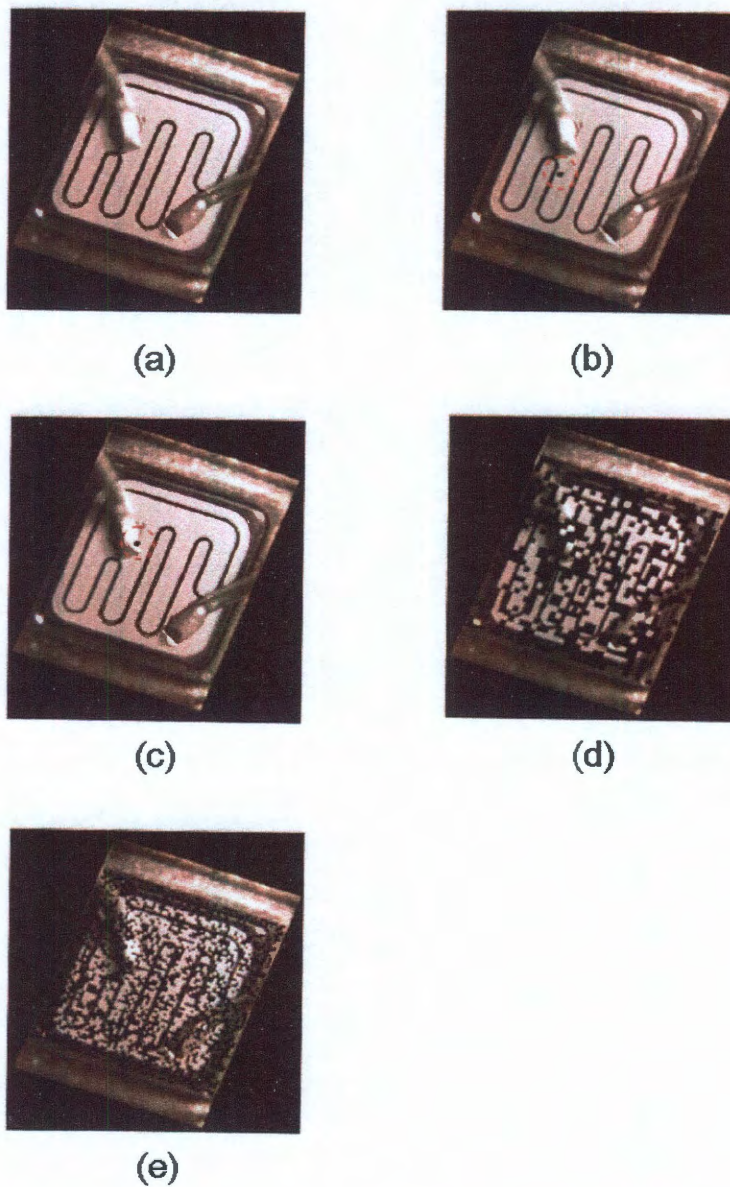


Figure 4.5 : Image of DUT with (a) 100% illumination. (b) - (c) represent pixels in a  $32 \times 32$  raster scan illumination pattern. (d) a  $32 \times 32$  permuted Walsh-Hadamard illumination pattern. (e) a  $64 \times 64$  permuted Walsh-Hadamard illumination pattern.

The sampled image resolution was set as  $256 \times 256$  pixels. The measurement patterns were switched every  $200\mu s$ , so the total data acquisition time needed was  $200 \times M \mu s$  ( $M$  is the number of measurements). We took a complete data set with the whole  $M = 256^2$  random patterns, then chose partial measurement data for reconstruction and quality comparison. In Figure 4.6(f), the result was reconstructed by all the  $256^2$  measurements and set as the raw image since it involved no compression. Figure 4.6(a)-(e) were reconstructed using partial measurements under different ratio. As shown, the recovered image quality kept improving as the number of measurements increased, especially when below 10%. After that, the improvement became very small and unnoticeable. In practice one would only record the required fraction of the total patterns, leading to an acquisition time advantage compared to raster scan. The flexibility to trade off SNR directly for acquisition time is an advantage of CS techniques over raster scan: if one terminates an OBIC scan 5% of the way through a measurement, one only obtains data for 1/20 of the field of view rather than obtaining an image that encompasses information from the entire field of view.

Figure 4.7 plots the normalized mean squared error versus the measurement ratio for OBIC reconstruction. The MSE drops quickly from 0.1 to 0.02 when the measurement ratio is below 10%. This trend shows that the number of measurements  $M$  reaches the sparsity level of the target at about 10%. In general,  $M$  is dependent on the sparsity of the scene in the reconstruction basis and the system noise level. For the same amount of data, the sparser a signal is, the better reconstruction is expected. Our experimental result is consistent with the simulation in Chapter 2.

It is also possible to employ all  $1024 \times 768$  micromirrors to produce a high resolution OBIC image as opposed to being limited by the base two nature of the Hadamard



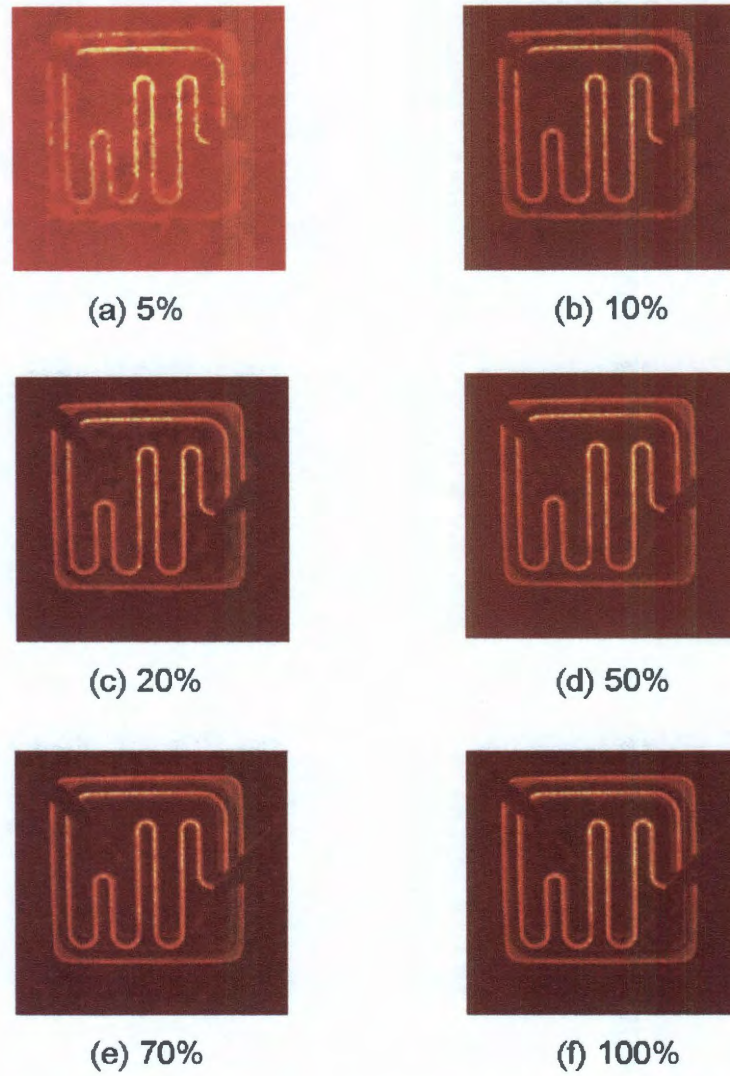


Figure 4.6 : (a)-(f) OBIC CS reconstructions of  $256 \times 256$  pixel image with different measurement ratio.

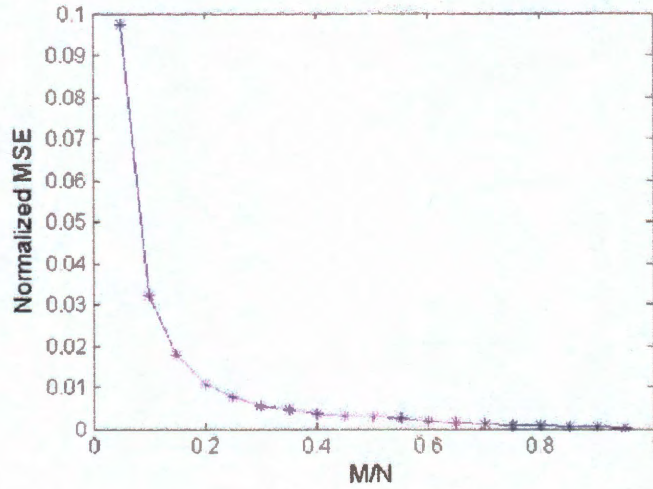


Figure 4.7 : Normalized mean squared error of  $256 \times 256$  OBIC reconstruction

transform. Figure 4.8 is the reconstructed image under 1:20 compression. The measurement only took about 8 sec. This was accomplished in a manner similar to the zero-padding to perform the fast Fourier transform on odd-sized images.

Except for the laser as the light source, we also presented CS-OBIC results acquired using a white light source (arc lamp). The SNR comparison of raster and CS was described under two situations - constant total illumination power and constant optical power per pixel.

The DUT was an NPN power transistor (Figure 4.9(a)) with the base and emitter terminals connected to a TIA. The whole DUT active area was uniformly illuminated. We displayed CS random pattern and raster scanning pattern on DMD respectively for data acquisition. The optical power on every mirror/pixel kept a constant. Figure 4.9(b) shows a CS result reconstructed with 30% of the data set for a  $256 \times 256$  pixel image. Figure 4.9(c) shows a raster result under the same spatial resolution. In this



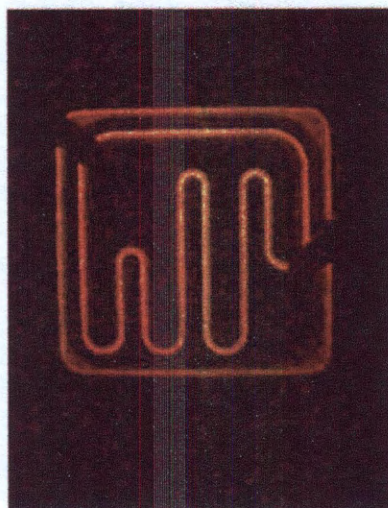


Figure 4.8 : OBIC CS reconstruction of a  $1024 \times 768$  pixel image using 5% of the total measurements.

case the signal was so small as to be limited by quantization noise in the ADC. The gain of the TIA was increased by  $10\times$  to compensate. Even in this case some of the weaker features (such as the outer contact ring due to the collector-base junction) were completely missing. The constant power per pixel assumption reflects cases in which there is a maximum allowed intensity one can apply to the DUT. This would be relevant when limited by optical damage to the DUT or by the need to avoid latchup.

In the constant illumination case, it is analogous to expanding a laser beam from a raster-scanning measurement to fill the entire die and performing CS instead. The setup was the same as the previous light condition, but we attenuated the white light source by approximate  $10^4$  during the CS measurements to achieve roughly constant total power for a  $128 \times 128$  pixel imaging. The results are shown in Figure 4.10. As predicted by theory, the raster measurement was cleaner, although the OBIC data was still quite good.

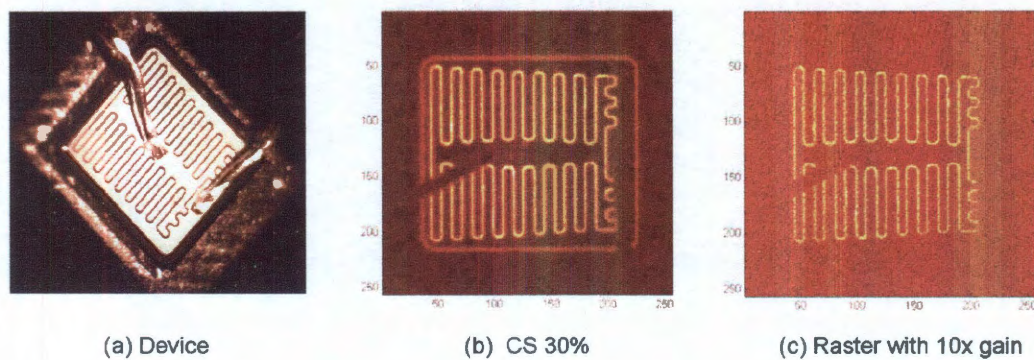


Figure 4.9 : OBIC measurements of DUT with constant optical power per pixel,  $256 \times 256$  resolution. (a) Image of the device. (b): CS measurements with 30% data. (f) Raster data with  $10\times$  extra gain to boost SNR.

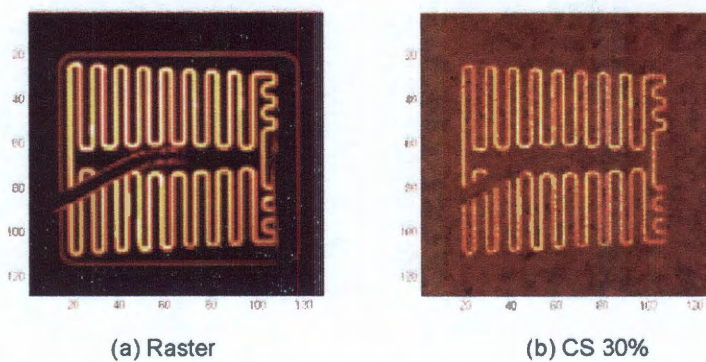


Figure 4.10 : OBIC measurements at constant total illumination power,  $128 \times 128$  resolution. (a) raster scan (b) CS with 30% data.



#### 4.4.2 IR-PEM Results

Visible imaging has been a mature industry because of the continued miniaturization and development of silicon CCD and CMOS technology over the past 30 years. Beyond the visible region, new narrow-bandgap materials such as InGaAs, HgCdTe and InSb need to be employed as focal plane arrays (FPA) for two-dimensional imaging in various bands of the infrared regions. The high cost of forming these materials into large pixel arrays has greatly limited the widespread use of such IR imagers. They also have different thermal expansion coefficients than the silicon of the read-out integrated circuit (ROIC) which is required to store the signal and to sequentially read the signal of all the pixels to an output amplifier. This mismatch brings more complexity and challenge to the sensor fabrication process. Another complication is the additional need for cooling to reduce the associated thermal noise and achieve a reasonable signal-to-noise ratio. Liquid nitrogen, Stirling cycle engine and Joule-Thompson cooler are the typical methods of cooling [26], which make the detector bulky, heavy, expensive or energy consuming.

As another important application, CS is also relevant for IR emission imaging from integrated circuits. Instead of acquiring emission images using expensive FPA detectors, one can use a single-pixel photon detector and spatial light modulator. This is the basis of the original single-pixel camera idea. The advantage in this case is the greatly reduced cost and complexity of a single-pixel emission microscope compared to an FPA-based system. Scientific-grade InGaAs FPAs with liquid-nitrogen cooling cost much more than 20K and are not commercially available everywhere in the world. On the other hand, a single-element photodiode along with a DMD could cost significantly less and achieve comparable levels of performance in some cases.

The infrared detector in our experiment was a commercial TE-cooled InGaAs

photodiode from Hamamatsu Corp. (G6122). The PNP power-transistor DUT was forward biased at  $V_{BE} = 1.8V$ ,  $I = 0.67A$ . The  $256 \times 256$  measurement patterns were changed every  $400\mu s$ . Figure 4.11(a)-(f) shows reconstruction results using varying fractions of the total potential 65K patterns.

Figure 4.12 plots the normalized mean squared error versus the measurements ratio for the recovered IR emission images. The number of measurements  $M$  reaches the sparsity level of the target at about 20%. It is higher than OBIC because the IR emission signal is much noisier due to inherently low photon counts and the non-cryogenic cooling of our detector.

The images are all reconstructed in less than 3s. with an ordinary personal computer. The fast acquisition (20% needs 6 sec.) and reconstruction make it particularly attractive for many practical applications.

In addition, the 90% fill factor of DMD provides high quantum efficiency compared to many focal plane array detectors. Furthermore, every separate sensor on an array detector receives light only from a single pixel of the scene, while in CS the single detected signal is always the light combination from half of all the pixels. In the regime where the total SNR is limited by dark noise of the detector, the optical Hadamard multiplexing achieved advantage by improving the SNR as

$$SNR_{CS} = (\frac{\sqrt{N}}{2})SNR_{raster}, \quad (4.8)$$

where we refer to the SNR averaged over the entire image.

To compare the results, we switched on one block of mirrors in turn to acquire raster scan image. The signal collected by the photodiode is corresponding to the one in each sensor of the FPA. As shown in Figure 4.13, when the resolution is as low as  $32 \times 32$ , the emission area shows up. When the resolution goes up to  $64 \times 64$ , 1/4 times less light is collected from each pixel and the area of interest is almost buried

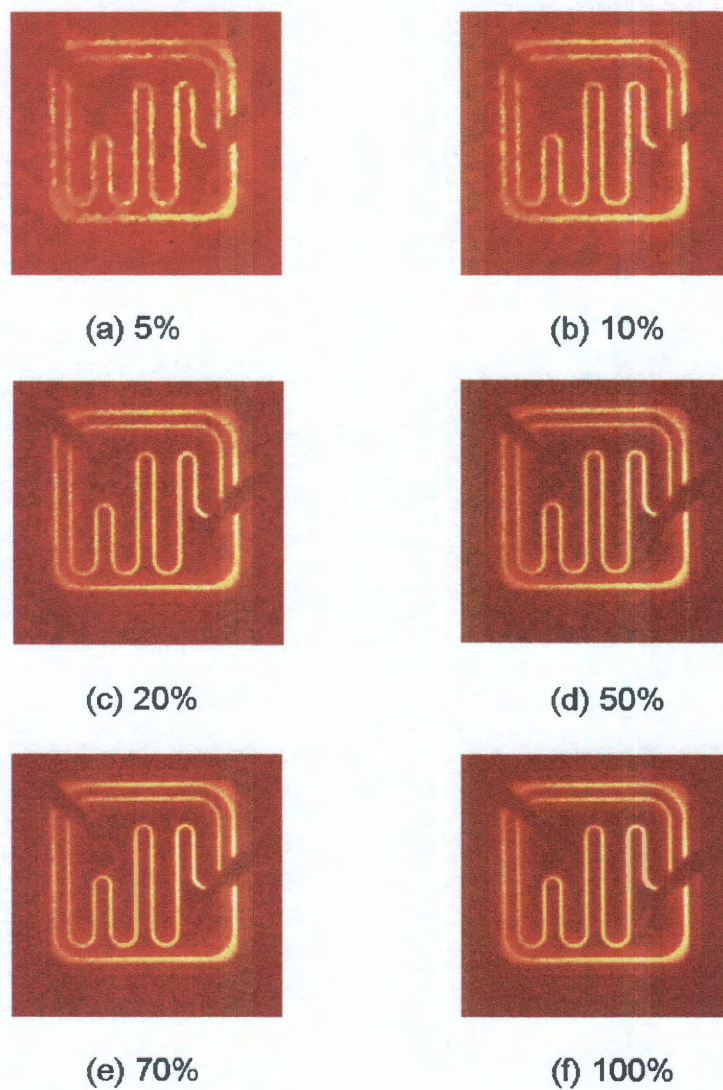


Figure 4.11 : (a)-(f) IR-PEM CS reconstructions of a  $256 \times 256$  pixel image with different measurement ratio.

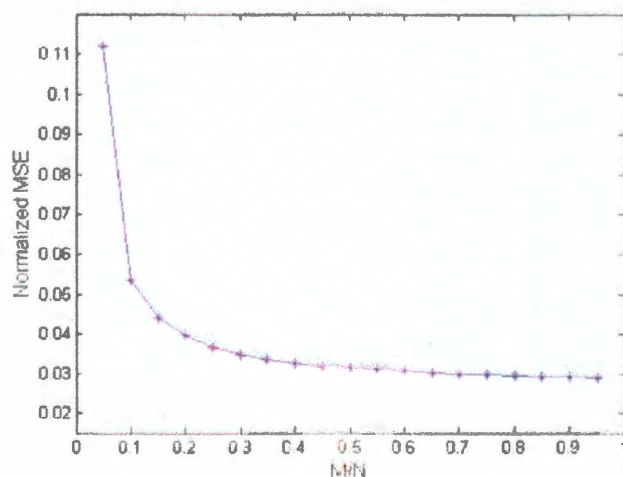


Figure 4.12 : Normalized mean squared error of  $256 \times 256$  IR-PEM reconstruction.

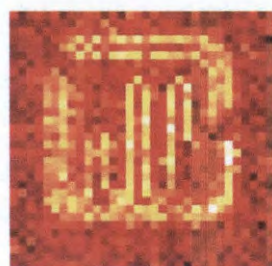
into background noise. At  $128 \times 128$  and  $256 \times 256$ , the image results in white noise, while under the same settings the CS reconstruction has a much higher SNR. This illustrates why traditional IR imaging requires significant cooling to reduce the sensor background noise and identify the signal from the target; yet CS based imaging can overcome this limit and reconstruct the entire image with higher quality.

When the transistor was reverse biased, twas reverse biased,

## 4.5 Summary

We have demonstrated OBIC measurements taken without the need for a laser or a laser-scanning microscope. Using a digital micromirror device and compressive sensing techniques, we are able to acquire OBIC data using a simple optical system. Under some circumstances a CS-OBIC system can outperform a comparable raster-OBIC system or be more suitable for automated measurements. For IR-PEM detection, compressive sensing based measurement also reduces the required size, complexity,

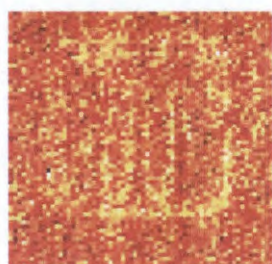




(a) Raster 32x32



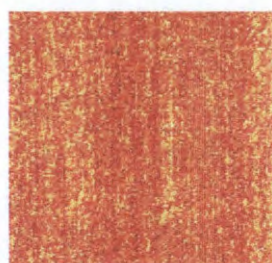
(e) CS 32x32 (80%)



(b) Raster 64x64



(f) CS 64x64 (60%)



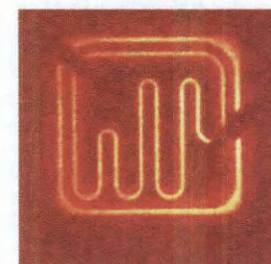
(c) Raster 128x128



(g) CS 128x128 (30%)



(d) Raster 256x256



(h) CS 256x256 (20%)

Figure 4.13 : IR-PEM results. Left column: Images obtained by raster scanning for various sample resolutions; Right column: Images obtained by CS measurement for the same sample resolutions but at a compressed rate.

and cost of the IR sensor array down to a single unit. In addition, the intensity of the compressed signal at the detector is greater than its raster scan counterpart and therefore results in better signal sensitivity and improved image quality.

## Chapter 5

# CS Application to Sum Frequency Generation

### 5.1 Introduction

Chemical heterogeneity of surfaces or interfaces plays a crucial role in fundamental understanding of many chemical processes and applications, such as heterogeneous catalysis, corrosion, wetting, natural systems, bio adhesion, and so forth. Macroscopic probe techniques such as x-ray photoelectron spectroscopy (XPS), Raman spectroscopy, infrared spectroscopy, and sum frequency generation (SFG) spectroscopy provide the spatially averaged information and are not typically able to deduce the chemical heterogeneity. A molecular-level microscopic picture of the chemical heterogeneity would allow an understanding of these processes in a more profound way.

Traditional heterogeneity characterization techniques, such as scanning tunneling microscopy (STM) [27], scanning electron microscopy (SEM) [28], transmission electron microscopy (TEM) [29], and atomic force microscopy (AFM) [30], while providing excellent spatial resolution are not able to elucidate the molecular chemical information of the surfaces/interfaces. Vibrational spectroscopy, Fourier-transform infrared microscopy (FT-IR microscopy) [31] and Raman micro-spectroscopy [32] allow the chemical imaging of heterogeneous systems; however they reveal only the structure of the bulk. XPS microscopy, another powerful technique which is capable of giving the chemical distribution on a surface requires ultra-high vacuum conditions and lacks the ability of probing interfaces involving liquids such as solid-liquid bound-

ary. SFG is a unique second-order nonlinear optical technique which is highly surface specific and allows the operation in ambient conditions and is able to detect various interfaces, such as solid-liquid [33], gas-liquid [34], and solid-gas interfaces with sub-monolayer sensitivity [35, 36]. Moreover, SFG is able to reveal the surface chemistry in both vibrational spectroscopy and the orientation of the functional groups on the surface/interface.

The conventional approaches of SFG imaging microscope and nonlinear microscopy include the traditional raster scan [37–43] or using a costly CCD camera as reported by Flörsheimer et al. [44], Kern and co-workers [45, 46], and Baldelli and co-workers [47–53]. SFG imaging of CO on platinum [47], microcontact-printed ( $\mu$ CP) mixed self-assembled monolayers (SAMs) on gold surfaces [53], microcontact-printed monolayers derived from aliphatic dithiocarboxylic acids [48], octadecanethiol SAM on mild steel [52], octadecanethiol on zinc surfaces [51], and patterned SAMs with different terminal groups were successfully conducted using the microscope. Note that most of the reported SFG imaging was on metal substrates. The detection limit of the CCD camera allows the detection of the relatively strong SFG signals. Furthermore, for conventional imagers as the resolution increases, or the number of pixels increases, the signal intensity on each pixel drops quickly and might drop below the detection limit; the acquisition time of the traditional imaging system is long. It is this impetus to develop an alternate, economic, SFG microscopy technique which provides two-dimensional chemical surface maps with better quality and is sensitive enough to detect the low SFG signal in a time efficient manner. The improvement of a faster acquisition and higher resolution of the images will greatly expand the utility of SFG imaging for surface chemists.

There are several features which make CS an unique and beneficial technique for



SFG imaging. First, CS involves acquiring a signal from a surface then reconstructing the image accurately from a far smaller number of linear measurements than the desired resolution of the images or signals. Second, CS always detects 50% of the signal from the surface all the time; the signal dilution with increasing resolution (or pixel), which is the limiting factor that affects the image quality and resolution for traditional raster scan and CCD mapping, does not apply to CS in the sense of dark noise or read-out noise limits of the detector. The improved SNR even with low gain and high resolution, compared to the traditional imaging, would be obtained for CS. Third, CS allows for the use of a single pixel detector, for example, PMT, to acquire the SF signal with gated integration data acquisition system. The higher gain of a PMT than that of the pixel sensors makes it possible to capture the weak SF signal and chemically image the surface/interface. Fourthly, the SFG-CS microscope is much more economic than the traditional imaging systems that use the costly CCD or CMOS imagers. In summary, CS enables significantly reduced measurement time and sampling rates, lowers the cost of the setup and allows better image quality even with high spatial resolution and thus high chemical contrast.

## 5.2 SFG Theory

Sum frequency generation [35] is a second order nonlinear optical technique which is very sensitive (detecting molecules at a level below  $10^{-9} \text{ mol/cm}^2$ ) [54], highly surface-specific [55] and provides molecular vibrational information of various surfaces and interfaces, such as air/liquid [34], liquid/liquid [56], liquid/solid [33], air/solid [35, 36] and solid/solid [57] interfaces.

When an external electric field becomes intense enough and is comparable to the internal field felt by an electron, the response of a material to the applied electrical

field is no longer linear. Under the electric dipole approximation the polarization  $\mathbf{P}$  is expressed as a power series in the field strength  $E$  as [58, 59]

$$\mathbf{P} = \chi^1 \mathbf{E} + \chi^2 : \mathbf{E}\mathbf{E} + \chi^3 : \mathbf{E}\mathbf{E}\mathbf{E} \dots,$$

where  $\chi^n$  is the  $n^{th}$  order susceptibility.

]When two laser beams, the visible beam and IR beam, overlap both in space and time, a new beam is produced with the sum of the incident frequencies, which can be expressed by 2<sup>nd</sup> order susceptibility as

$$\mathbf{P} = \frac{1}{2} \chi^2 : \mathbf{E}_1 \mathbf{E}_2 \cos(\omega_1 + \omega_2)t.$$

The direction of the SF signal is determined by momentum conservation parallel to the interface

$$k_{SFx} = k_{Visx} + k_{IRx},$$

where  $k_{SFx}$  is the wave vector of the SF signal along  $x$  axis,  $k_{Visx}$  is the wave vector of the visible beam along  $x$  axis, and  $k_{IRx}$  is the wave vector of the IR beam along  $x$  axis. For a co-propagation geometry, the momentum conservation could be written as [58–60]

$$\omega \sin \beta = \omega_1 \sin \beta_1 + \omega_2 \sin \beta_2,$$

where  $\omega$ ,  $\omega_1$  and  $\omega_2$  are the frequencies of the SF signal, visible and IR laser beam, respectively;  $\beta$ ,  $\beta_1$  and  $\beta_2$  are the incident or reflection angle from surface normal of the SF, visible, and IR beams, respectively. The intensity of sum frequency signal is given by

$$I_{SF} \propto |\chi_{eff}^{(2)}|^2 I_{IR} I_{VIS},$$

where  $\chi_{eff}^{(2)}$  is the effective second order susceptibility,  $I_{IR}$  and  $I_{VIS}$  denotes the intensity of the incident IR beam and visible beam.  $\chi_{eff}^{(2)}$  consists of two parts, a resonant

component  $\chi_R^{(2)}$  and a nonresonant component  $\chi_{NR}^{(2)}$ , as described by the following equation

$$\chi_{eff}^{(2)} = \chi_R^{(2)} + \chi_{NR}^{(2)}.$$

For dielectric materials,  $\chi_{NR}^{(2)}$  is typically small, while for metals and semiconductors the nonresonant signal generally would be complex quantities and large [60,61] due to highly nonlinear properties of the materials. [55,62,63].

### 5.3 Experiment Preparation

In SFG imaging experiment, the samples to be examined is synthesized by Baldelli's group at University of Houston. The detailed preparation process is as follows:

1. **Materials:** The alkanethiol, 1-octadecanethiol (98%), was purchased from Sigma Aldrich; heptane,  $Na_2S_2O_4$ ,  $H_2O_2$  (30 wt.% solution in water), and  $K_4Fe(CN)_6$  were from Aldrich and used as received; absolute ethyl alcohol was from Aaper. KOH was obtained from Mallinckrodt Chemicals;  $K_3Fe(CN)_6$  and 1-Octanol were from Baker;  $H_2SO_4$  (> 98%) was from Fisher. The prepolymer, Sylgard silicone elastomer base and curing agent, used for fabricating the elastomeric stamps, were obtained from Dow Corning Corp. All aqueous solutions were prepared in  $18.2M\Omega \cdot cm$  water obtained by purification of distilled water with a Millipore Milli-Q system. The replica master mold used for microcontact printing was a homemade one with stripes of a width of  $100\mu m$  and spacing of  $100\mu m$ . All chemicals were used as received.
2. **Gold Surface Preparation:** Evaporated gold surfaces were used to prepare the gold stripe pattern and the octadecanethiol self-assembled monolayer (ODT SAM) pattern. Gold of 99.99% purity was used. Gold films of a thickness of

100nm were deposited on the highly polished side of silicon (100) substrates by thermal evaporation at a pressure of  $1 \times 10^{-5}$  Torr in a vacuum chamber with a rate of  $1.0 \sim 1.1 \text{ \AA/s}$ . A 10 nm Cr layer was deposited with a rate of  $1.0 \text{ \AA/s}$  prior to Au to improve the adhesion to the Si wafer.

3. **Microcontact Printing and Gold Pattern Fabrication:** The micropatterned, elastomeric polydimethylsiloxane (PDMS) stamp was replicated from the master mold, following the published procedure [64]. The stamp was inked by dropping a 3mM ODT ethanol solution on the surface with the patterns and blow-dried gently with nitrogen gas until no solvent was observed. The stamp was then brought into contact with the gold surface for about 30s with gentle pressure. The gold features were generated by etching the ODT patterned gold surface utilizing a solution of the mixture of  $\text{Na}_2\text{S}_2\text{O}_3$  (0.1 M),  $\text{KOH}$  (1.0 M),  $\text{K}_3\text{Fe}(\text{CN})_6$  (0.06 M), and  $\text{K}_4\text{Fe}(\text{CN})_6$  (0.001 M). A “defect-healing” additive, 1-octanol was added to the etching bath as well to achieve high-selectivity etching. The substrate with features of gold was then sonicated in MilliQ water for about 1 minute, rinsed thoroughly with MilliQ water and absolute ethanol and dried under a stream of nitrogen gas. The optical microscope image of gold pattern by a  $5\times$  optical microscope is illustrated in Figure 5.1. The actual width of both the gold stripe and spacing is about  $100\mu\text{m}$ .

The fundamental  $1064\text{nm}$  laser was produced by a PL2251 series  $\text{YVO}_4/\text{YAG}$  diode laser (Ekspla) with a repetition rate of  $20\text{Hz}$ . Then it was split into two beams. One passed through a nonlinear crystal  $\text{KTiOPO}_4$  (KTP) and generated a  $532\text{nm}$  green laser via second harmonic generation. The other was incident to an optical parametric generator/optical parametric amplifier (OPG/OPA, Laservision)

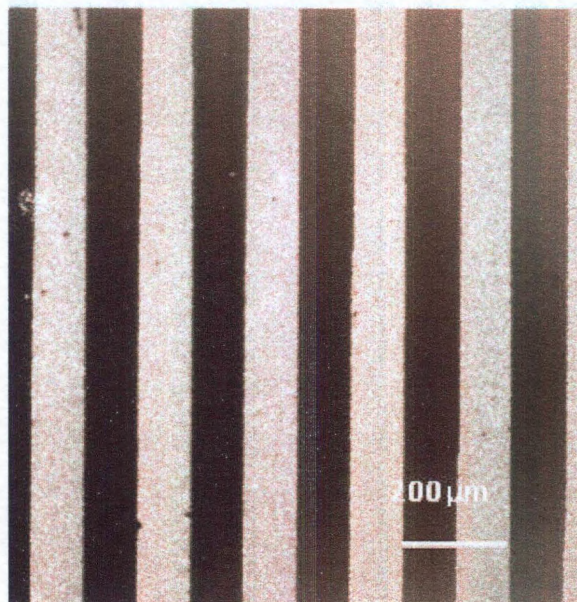


Figure 5.1 : Optical microscope image of the gold pattern.

system and produced tunable IR beam with the wavenumber varying from  $2000\text{cm}^{-1}$  to  $4000\text{cm}^{-1}$ . In our experiment, the IR wavenumber is fixed at  $2880\text{cm}^{-1}$ . At this wavenumber, both the nonresonant signal from the gold surface and the resonant signal of the symmetric C—H stretching from the residue ODT monolayer on the gold stripes contributed to the detected SF signal.

#### 5.4 Microscope instrumentation

Figure 5.2 shows a picture of the SFG compressive sensing imaging (SFG-CSI) microscope. Figure 5.3 illustrates its schematic diagram. The  $532\text{nm}$  visible beam and tunable IR beam overlapped temporarily and spatially on the sample at an incident angle (relative to the surface normal) of  $50^\circ$  and  $60^\circ$ , respectively. The SF signal's angle is  $51.2^\circ$  determined by momentum conservation. Then the SF signal passed

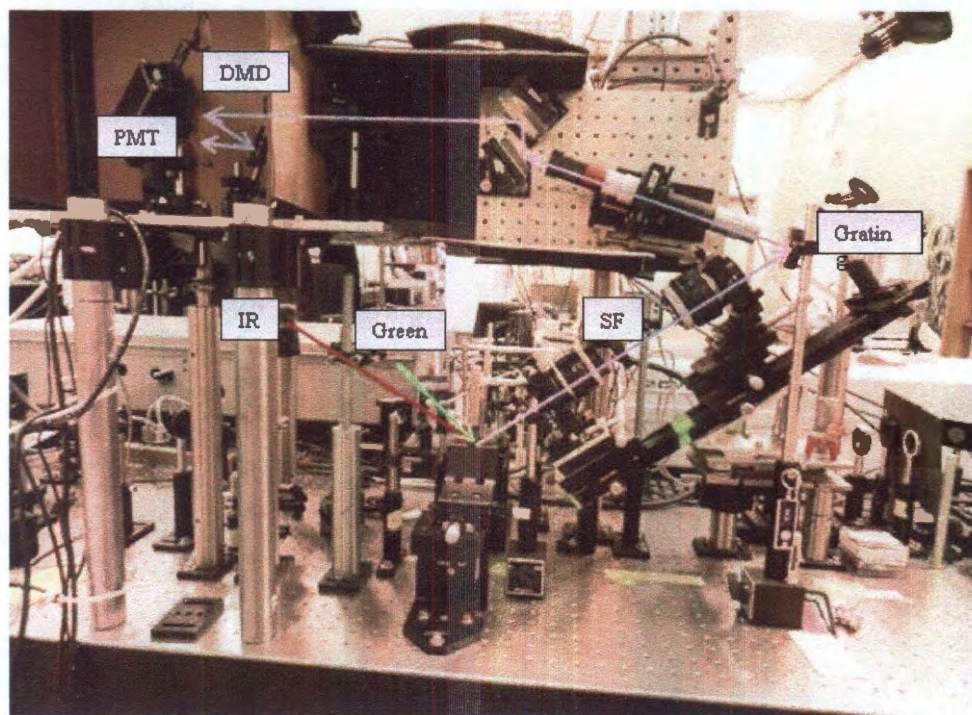


Figure 5.2 : the sum frequency generation-compressive sensing imaging microscope.



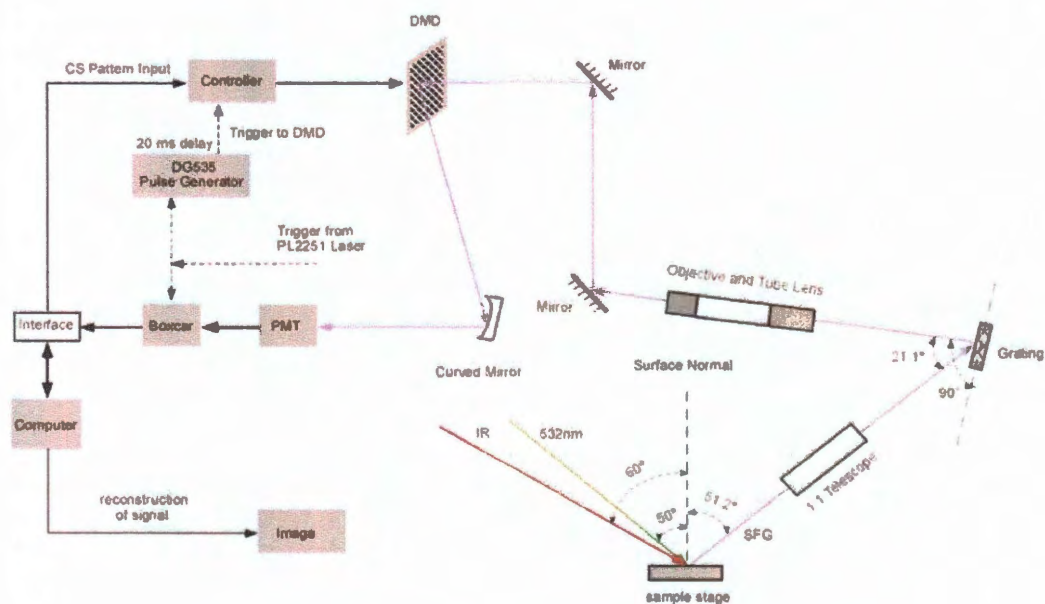


Figure 5.3 : Schematic diagram of SFG-CSI microscope setup

through a 1:1 telescope which maintains the size of the SF beam. The telescope is composed of two sets of Nikon camera lenses (55mm and 50mm) and reduces spherical and chromatic aberrations to improve the image quality. A 1200/600 nm interferometrically ruled precision grating (Thermo Jarrell Ash) in a Littrow condition with the diffracted beam perpendicular to the grating surface was used to direct the SF beam to a 1 : 10 magnification system. The incident angle of the SF signal to the grating was set to be  $21.1^\circ$  to the grating surface normal. The SF beam magnified by the  $10\times$  microscope was maintained collimating by a tube lens and then reflected by two mirrors to the DMD. The DMD modulated and reflected the SF beam to a silver coated concave mirror with a focal length of 150mm. The concave mirror focused the SF beam onto the detector, a R928HA photomultiplier tube obtained from Hamamatsu. Before the beam impinged to the PMT, seven filters were used along the SF

beam path to filter out the light except for the SF signal. The filters include (1) two 505 SP (400-510 nm, transmittance 85%) short pass filters, one 441.6AELP-GP long pass filters in front of the PMT; (2) two 505 SP short pass filters mounted in a tube and placed in front of the DMD; (3) one 505 SP short pass filter placed right after the sample and in front of the first lens of the 1:1 telescope; and (4) one 465AF50 Omega optical band-pass filter (430-480 nm, transmittance 70-80%) placed between the two lens sets of the 1:1 telescope.

The YAG laser has a 20Hz precise trigger (PRET) output which was used to synchronize the SF pulse generation with DMD pattern switching, and PMT data acquisition. The boxcar integrator and A/D computer interface were triggered by the master PRET trigger. The DMD pattern switching was triggered by a TTL trigger from the oscilloscope (Stanford Research Systems, Inc., Model DG535), which was also triggered by PRET with a 20 ms delay.

The whole synchronization process of the laser, DMD and A/D converter was integrated into a LabVIEW program. The inputs for the program are the location of file of generated DMD patterns, total number of patterns, average number and location of output acquisition data file. The program first initializes the DMD driver, sets parameters of DMD, and transfers patterns from pattern files to the RAM of DMD. For example, the program sets the DMD to slave mode, which means the DMD displays a pattern only when it receives a trigger signal. Then it communicates with the data acquisition board and set its synchronization mode. The main principle is that for every trigger signal generated from the oscilloscope, the DMD displays a pattern and then the acquisition board acquires a signal. The program interface shows the current pattern displayed in DMD as well as signals acquired from acquisition board in real time. It implements the synchronization communications of the hardware for



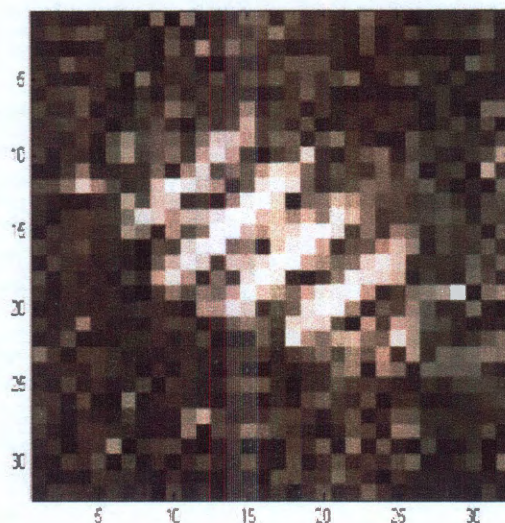


Figure 5.4 : A  $32 \times 32$ -pixels SFG image of gold pattern reconstructed using 100% measurements. 200 laser pulses were averaged for each measurement. Signal from Au stripes was bright and signal from Si substrate was dark.

the whole system and the automatic signal detection.

## 5.5 Results and Discussion

Figure 5.4 shows the sum frequency generation image of the gold pattern acquired and reconstructed using the CS technique. The image resolution was set as  $32 \times 32$  pixels. 1024 random patterns were applied to DMD in a time sequence and 200 pulses were acquired and averaged for each pattern. The IR beam diameter, which is the limiting size for SF signal generation, was about  $800\text{-}1000\mu\text{m}$ . Therefore 4-5 gold stripes were captured in the SFG image of the gold pattern. The intensity distribution in the image is due to the visible and IR beam profiles, which follow Gaussian distribution

in an ideal case and have the highest intensity distributed in the center of the beam.

Since measurement noise is the crucial factor that dictates the number of measurements needed for reconstruction in CS. For a  $k$ -sparse signal, the following condition on the number of measurements was obtained [65]

$$M \geq \frac{2K \log(N/K)}{\log(1 + SNR)},$$

where  $N$  is the signal length;  $K$  is the sparsity of the system;  $M$  is the minimum number of measurements needed. The sparser the image or the higher the SNR, the less measurements needed for a decent reconstruction result. Therefore, in our experiment, we usually acquired a certain amount of SF pulses/shots and averaged them to one measurement for each random pattern to obtain relative high SNR. Figure 5.5 shows the measurement coefficients averaged with different number of pulses/shots and the images reconstructed. It shows the results of 20, 50, 100, 120, 150, and 200 shots acquired per pattern. The results clearly showed that for 20 shots per pattern, the coefficient plot was quite noisy and the image barely showed the stripe; for 50 shots per pattern the coefficients were less noisy and in the image the stripes emerged. As the number of shots increased from 20 to 200, a progressive improvement of SNR was observed from the measurements and the reconstructed image quality as well. Figure 5.6 illustrated the relationship of relative noise level with the number of shots acquired. The noise was calculated as the standard deviation of the standard deviation of the SF signal for each pattern over a specific number of pulses. It shows a dramatic improvement as the number of shots per pattern increases.

The effect of number of CS measurements was also examined. In Figure 5.7, (a)-(f) show the SFG images reconstructed using various measurement ratio, from 20% to 100%, with each measurement averaged from 200 shots. The image reconstruction

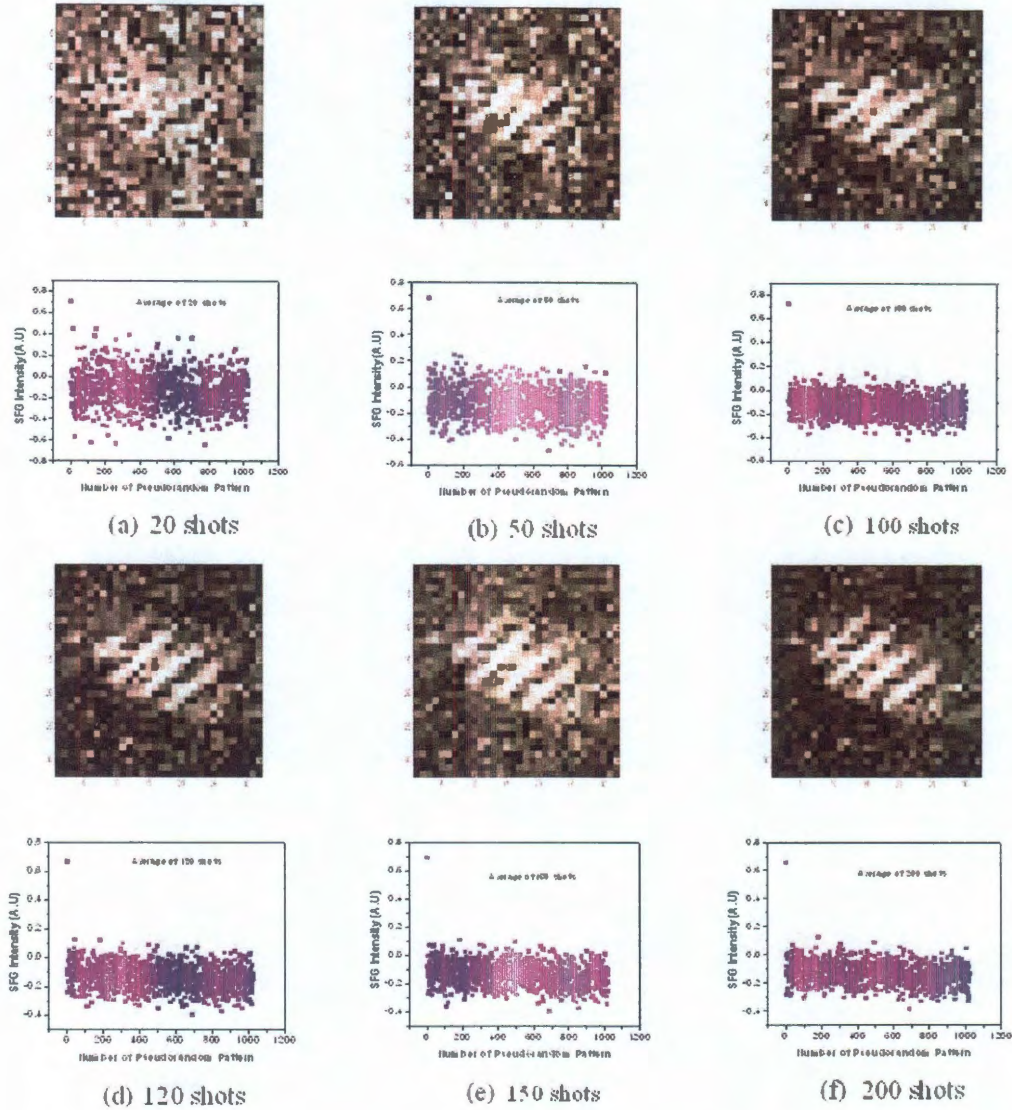
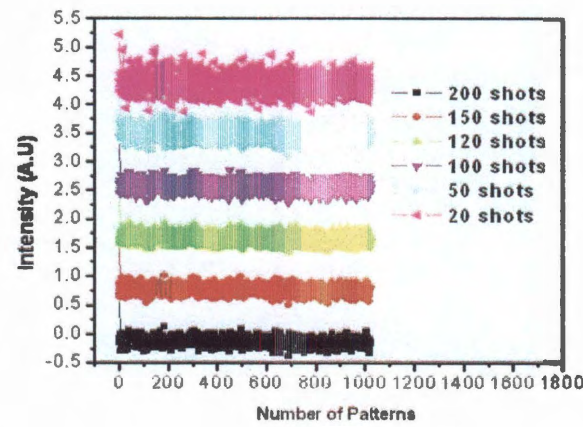
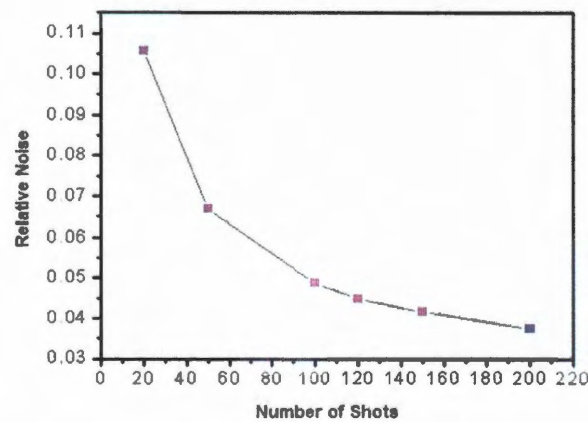


Figure 5.5 : Effect of number of pulses/shots per random pattern on the quality of the SFG-CS images: reconstructed images and the corresponding measurement coefficients obtained with various number of shots, (a) 20 (b) 50 (c) 100 (d) 120 (e) 150 (f) 200. The images were recovered at a resolution of  $32 \times 32$  pixels and 1024 patterns employed.





(a)



(b)

Figure 5.6 : (a) Measurement coefficients averaged with various numbers of shots per pattern (b) Illustration of SNR change: standard deviation of the averaged measurements under 20, 50, 100, 120, 150 and 200 shots per pattern. The images were obtained at a resolution of  $32 \times 32$  pixels and 1024 patterns employed. To get a clear comparison of the coefficients, some curves were offset in (a).

using 20% of the available patterns did not give clear stripes of the Au pattern. As the number of patterns increased better image of the gold pattern were obtained.

The previous images showed that the DMD was under filled with the SF signal. Attempts was made to enlarge the SF beam by adjusting the IR lens to make the IR beam larger and by moving the objective of the 1:1 telescope closer to the sample and the corresponding adjustment of the other lens set. Images obtained under this condition were shown in Figure 5.8. The resulting images indicated that the magnification of the SF beam was larger after the adjustments however the DMD was still not filled up with the SF beam.

Figure 5.8 shows the comparison of the images acquired and reconstructed at different image resolutions,  $32 \times 32$  pixels and  $64 \times 64$  pixels. The number of shots per CS testing pattern was 150 for both images. It showed that the higher resolution,  $64 \times 64$  pixels, provides better image of the gold pattern. Note that the width of the gold stripe and spacing is around  $100 \mu m$ ; the width of each individual micromirror of the DMD is  $10.8 \mu m$ . A random pattern uses a  $768 \times 768$  mirror array. For a  $32 \times 32$  pixel image resolution, an array of  $24 \times 24$  mirrors was defined as one optical unit and width of this unit is about  $260 \mu m$  ( or a little bit larger than  $260 \mu m$  if taking the spacing between mirrors into account), which is larger than the actual width of the gold stripe, while for a  $64 \times 64$  pixel image resolution, the optical unit consists of  $12 \times 12$  mirrors and the width of the optical unit is about  $130 \mu m$ , which is closer to the actual width of the gold stripe.

A comparison of using CS and the traditional raster scan to obtain the SFG image of the gold pattern was also performed. Figure 5.9 shows the images of the gold pattern obtained using both CS and raster scan at various image resolutions,  $16 \times 16$  and  $32 \times 32$ . For both CS and raster scan at a resolution of  $16 \times 16$ , two

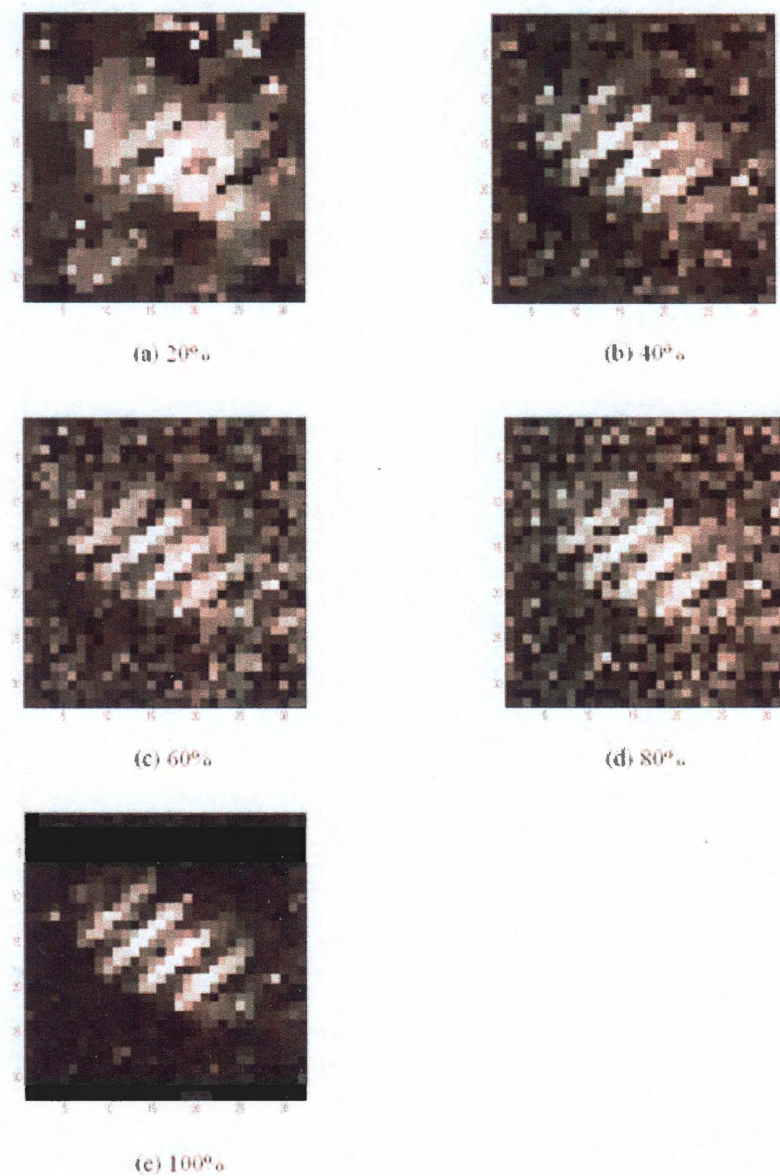


Figure 5.7 : Number of pattern effect on quality of the reconstructed SFG images of the gold pattern. The image resolution was  $32 \times 32$  and 200 shots per pattern were obtained and averaged. (a) 20%, (b) 40%, (c) 60%, (d) 80%, and (e) 100% of the total patterns.



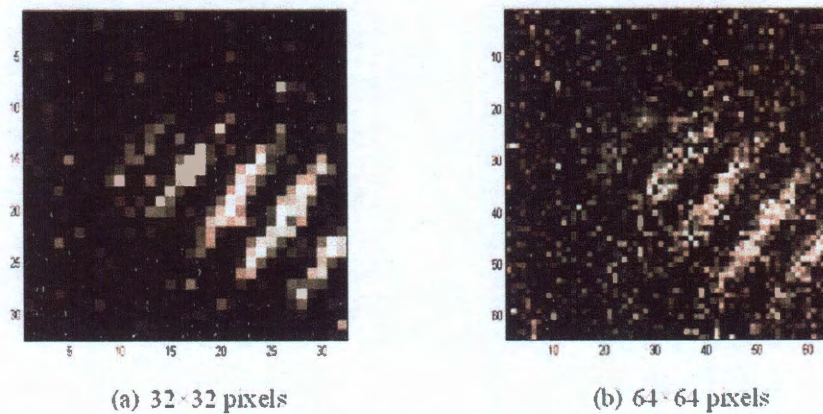


Figure 5.8 : Comparison of the quality of the SFG-CS images using various image resolutions applied to the DMD. 150 shots were acquired and averaged for each pattern applied to DMD. (a) SFG-CS image acquired and reconstructed at an image resolution of  $32 \times 32$  pixels with 1024 patterns. (b) SFG-CS image acquired and reconstructed at an image resolution of  $64 \times 64$  pixels with 4096 patterns.

blurry stripes appeared in the SFG images. As the resolution increased to  $32 \times 32$ , a better image of the gold pattern was obtained using CS, while for raster scan the chemical contrast of the SFG signal of the gold pattern was lost. The advantage of CS methods showing here is unique. CS measures 50% of the signal all the time and therefore maintained a good signal to noise ratio, while for raster scan the signal was diluted by increasing the resolution, or the pixels.

## 5.6 Summary

A new SFG microscope against the traditional imaging concept by using the novel sampling theory, compressive sensing, was successfully constructed. The sum frequency generation image of a gold pattern with stripes was successfully acquired and recovered using CS algorithms. The next step is to perform the CS-SFG imaging on

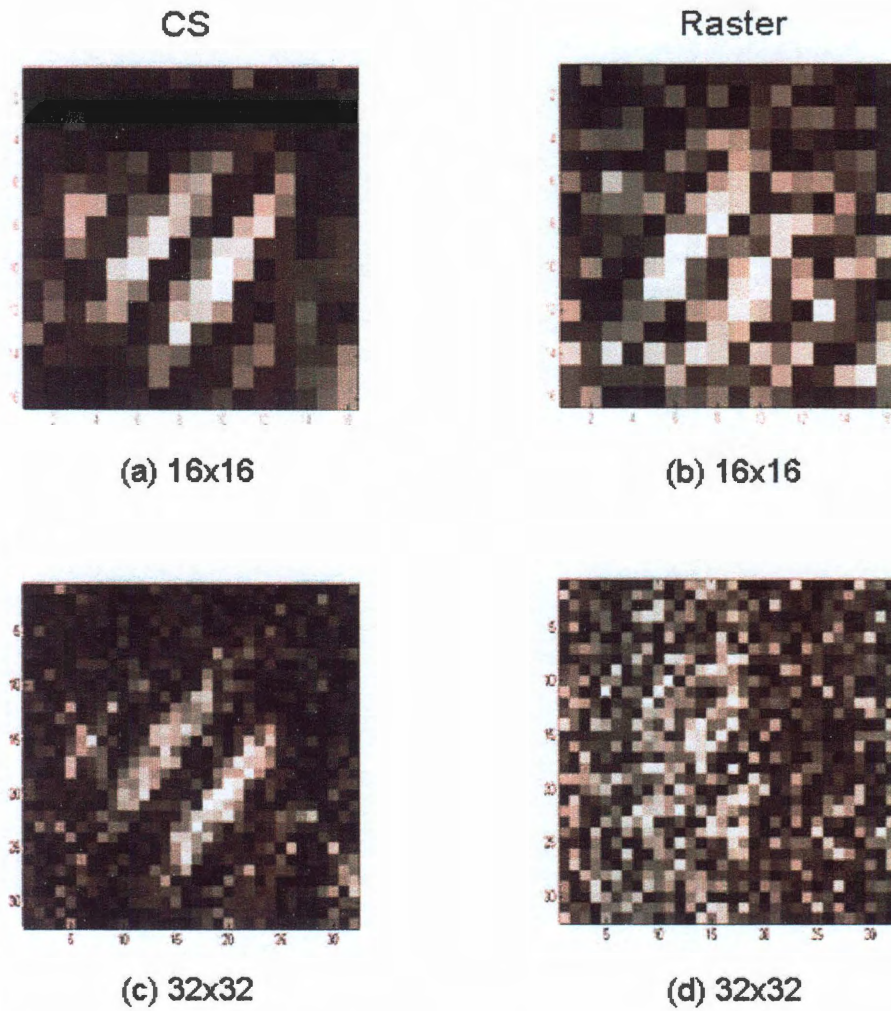


Figure 5.9 : . Comparison of the SFG images obtained using the novel CS and the traditional Raster method. (a) CS image at a resolution of  $16 \times 16$  pixels (b) Raster scanning image at a resolution of  $16 \times 16$  pixels (c) CS image at a resolution of  $32 \times 32$  pixels (d) Raster scanning image at a resolution of  $32 \times 32$  pixels.



dielectric material, such as molecules and bio-samples, with higher spatial resolution.

Because the current picosecond laser system with a low repetition rate was not able to fully implement the inherent advantages of CS. Using higher repetition rates and shorter pulses will impact signal, push the sample damage threshold to a higher value and reduce the necessary measuring times.

## Chapter 6

### CS Application to Hyperspectral Imaging and Endmember Unmixing

We design and construct a hyperspectral imaging system based on the idea of single pixel camera. An important advantage of the single pixel camera is that the detector can be swapped out for alternatives. For instance, one could easily replace the photodiode with a spectrometer to create a compressive hyperspectral imager. The random multiplexed light from the target is diffracted along the linear sensor array inside the spectrometer. Each sensor takes the compressed measurement of corresponding wavelength band. Thus, the spatial as well as the spectral information are acquired simultaneously and a 3D hyper-cube can be reconstructed based on those compressed measurements.

The other important CS application in hyperspectral imaging is endmember unmixing. As we know, the hyperspectral data cube is embedded with spectral information of different materials. Based on their unique spectrum signatures, material identification and classification can be realized. Hyperspectral unmixing algorithms decompose the pixel spectrum to identify the relative abundance fractions of materials or endmembers. The representative endmembers from a scene are generally known a priori from a spectral library (e.g., ASTER [66] and USGS [67]) or codebook. If the 3D hyper-cube is fully accessible, many algorithms are available aiming at endmember search in a scene, such as N-FINDR [68], PPI (pixel purity index) [69], VCA (vertex component analysis) [70], and SGA (simplex growing algorithm) [71]; NMF-MVT

(nonnegative matrix factorization minimum volume transform) [72], SISAL (simplex identification via split augmented Lagrangian) [73], MVSA (minimum volume simplex analysis) [74], and MVES (minimum-volume enclosing simplex) [75]. CS can contribute its value in the hyperspectral data acquisition and full cube reconstruction. However, its benefit does not end there. Instead of reconstructing the cube followed by the existing unmixing process, a direct endmember unmixing is available from the CS measurements. The intermediate, complicated 3D cube recovery stage can be bypassed, which will greatly save the data storage and the computational power because the massive cube always generates huge amount of data and consumes lots of memory and CPU resources. Detailed interpretation of CS endmember unmixing model as well as the real data analysis will be presented within this chapter.

## 6.1 Introduction to Hyperspectral Imaging

Electromagnetic (EM) radiation is a form of energy exhibiting wave-like behavior traveling through a free space or a material medium. It may be reflected, transmitted or absorbed. The amount and spectral composition of energy reflected depends on the nature of the surface. For any given material, the amount of radiation varies with wavelength. By monitoring the interaction of electromagnetic radiation with matter as a function of wavelength, the unique material is represented with its individual spectral "fingerprint".

In hyperspectral imaging, data is collected and processed from across a broad EM spectrum. Unlike a consumer camera, which just records visible light, a hyperspectral camera can see much more beyond it. As such, a hyperspectral image can be represented by a three dimensional data cube  $H$  with two spatial dimensions and one spectral dimension for processing and further analysis (Figure 6.1). Each two

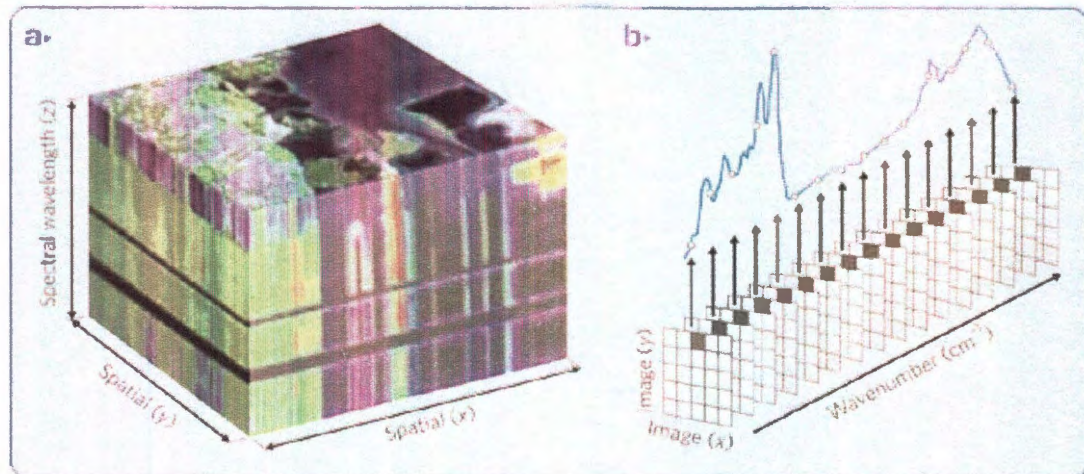


Figure 6.1 : The hyperspectral cube structure. [4]

dimensional slide  $H(\cdot, \cdot, z)$  corresponds to a spatial image at a different spectrum  $z$ , and each vector  $H(x, y, \cdot)$  is the spectral information at a different spatial coordinate  $(x, y)$ . For instance, data in the RGB image directly offer a visual way to show the spatial information by three bands corresponding to Red, Green and Blue. A hyperspectral imager records light signals at typically more than 300 bands from deep UV to far infrared.

The greatest advantage of hyperspectral imagery lies in target recognition and identification. Like the eyes of mantis shrimps, which enable them to visualize many different corals, prey, or predators that all appear as the same color to human eyes, information across different spectra enables the recognition of different types of targets that are hardly distinguishable in color pictures. For much of the past decade, hyperspectral imaging has been actively researched and widely developed. Researches are working on designing all kinds of hyperspectral imagers to acquire the 3D hyper-cube and curve fitting algorithms to segment one material from each other and calculate

their spatial distribution. This has become one of the most important topics in remote sensing field and has drawn more and more attention because of its great potential for application in mineral exploration [76, 77], environmental monitoring [78], food and agriculture [79], chemistry and biology [80], etc.

## 6.2 Traditional Hyperspectral imaging

This important sensing method is based on the conventional scanning mode detection. To acquire the hyperspectral data cube, typically a raster scan is required [81, 82], or a tunable spectral filter is needed in the spectral dimension [83].

### 1. Space-based hyperspectral imager:

The motion of the observing platform accounts for two scanning modes - whisk broom and push broom (Figure 6.2(a) and 6.2(b)). The whisk broom, also termed across track, uses a 1D linear sensor array as the detector. A mirror scans across every spot of the scene and reflects light to a grating which disperse the signal along the sensor array. Thus, a spectrum  $H(x, y, \cdot)$  is collected from one spot at a time. By arranging all the vectors together, a hyper-cube is formed. Since each pixel in each spectral image is acquired with the same detector, the artifacts are relatively simple and easier to correct. However, it has relatively low spatial resolution. The short dwelling time results in relatively low SNR. The mechanical scanning parts make this type of sensor expensive and more prone to wearing out.

The push broom, termed along track, uses a 2D sensor array as detector and gathers a complete spectrum of each point on one spatial line. The area of interest is scanned one line at a time. Light enters the spectrometer through a slit and recorded with a CCD or CMOS camera after diffraction. Each column

of sensors gives a readout of the spectrum for one point or pixel on a line that crosses the scene. To image the whole area, the camera must move. The hypercube is formed by compiling the optical data from each spatial line. Compared to whisk broom, it has longer dwelling time which provides higher SNR. But each column of each spectral image is acquired with a different detector which leads to striping artifacts.

## 2. Spectrum-based hyperspectral imager:

Each spectral slice  $H(\cdot, \cdot, z)$  is captured with a 2D sensor array under a bandpass filter (Figure 6.2(c)). Spectrum within a certain range is captured each time. By changing the filters, the whole wavelength range is covered. Stack up those frames and generate a cube. The spectral resolution depends on the number of filters switched. The camera and sample can remain stationary. But the spectra resolution is relatively low due to the number of filter sets available and their high cost.

These traditional hyperspectral imagers need to acquire information from every voxel. Huge amount of data from a scene (normally hundreds of megabytes), need to be stored and processed, which brings heavy computation burden and programming complexity into the hyperspectral acquisition stage. To simple the hardware and software implementation, reduce the high cost of the detectors and achieve a decent signal to noise ratio, compressive sensing offers a great solution.

## 6.3 CS Hyperspectral Imaging

The theory of CS shows that a sparse or compressible signal can be recovered from a relatively small number of linear measurements. In particular, the concept of the sin-



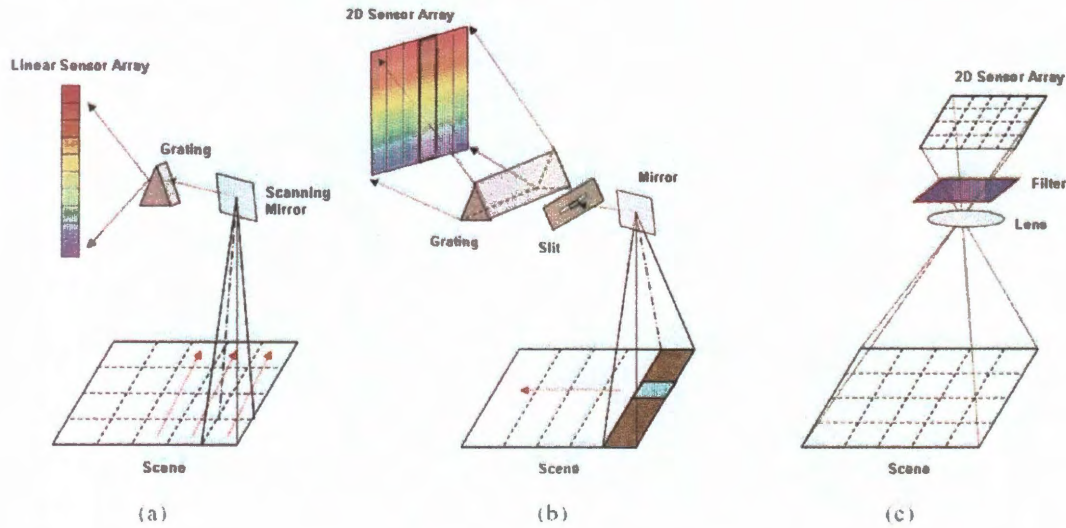


Figure 6.2 : Traditional hyperspectral acquisition techniques: (a) whisk broom; (b) push broom; (c) filter wheel.

gle pixel camera can be extended to the acquisition of compressed hyperspectral data. By replacing the photodiode with a spectrometer, the single-pixel camera is converted into a compressive hyperspectral imager. The logged data is now represented as a linear vector for each random projection instead of a single number reflecting the photo-voltage. As shown in Figure 6.3, we represent the data as a matrix  $Y$ , where each column corresponds to a different spectral band and each row corresponds to a different measurement vector. The hyperspectral cube  $X$  is reshaped to a 2D matrix with the dimension of  $N \times S$ .  $S$  is the number of bands and  $N$  is the number of spatial pixels. However, the dimension of measurements  $Y$  is only  $M \times S$  ( $M$ : the number of measurements or random patterns), which is much smaller than  $X$ . To reconstruct  $X$  from  $Y$  is like to solve an underdetermined equation, with information much less than the number of unknowns. This type of inverse problem has infinite solutions. However the restriction of sparsity of hyperspectral cube helps to find the

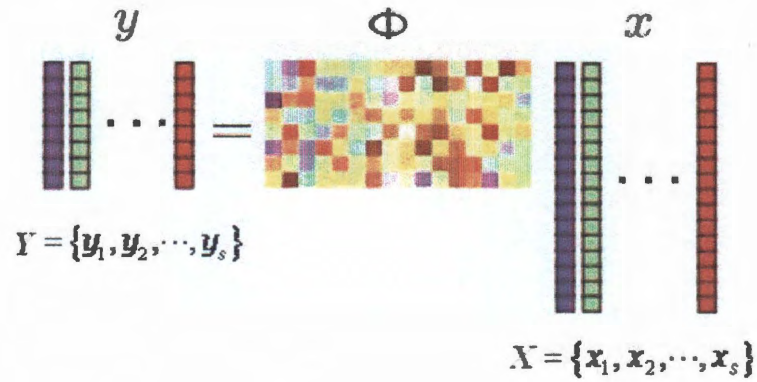


Figure 6.3 : CS hyperspectral paradigm illustrated in linear algebra

most optimized solution, which is the sparsest one.

### 6.3.1 Experiment Setup

Figure 6.4 is the CS hyperspectral setup. The spectrometer we employed was the QE65000 by Ocean Optics which features a Hamamatsu back-thinned detector with a 2D arrangement of pixels (1044 horizontal  $\times$  64 vertical) responsive from 200-1100 nm, with a optical resolution of 0.8nm. The spectrometer contains a 16-bit A/D converter delivering a dynamic range of 25000:1 and a signal-to-noise ratio of 1000:1. It is synchronized with the DMD. Whenever the pattern changes, DMD sends out a pulsed signal to the spectrometer and the sensor starts to integrate the light signal. Targets are uniformly illuminated with two halogen bulbs from 45° on both sides. The camera on the left arm helps to visualize and make sure the target is focused on the DMD.



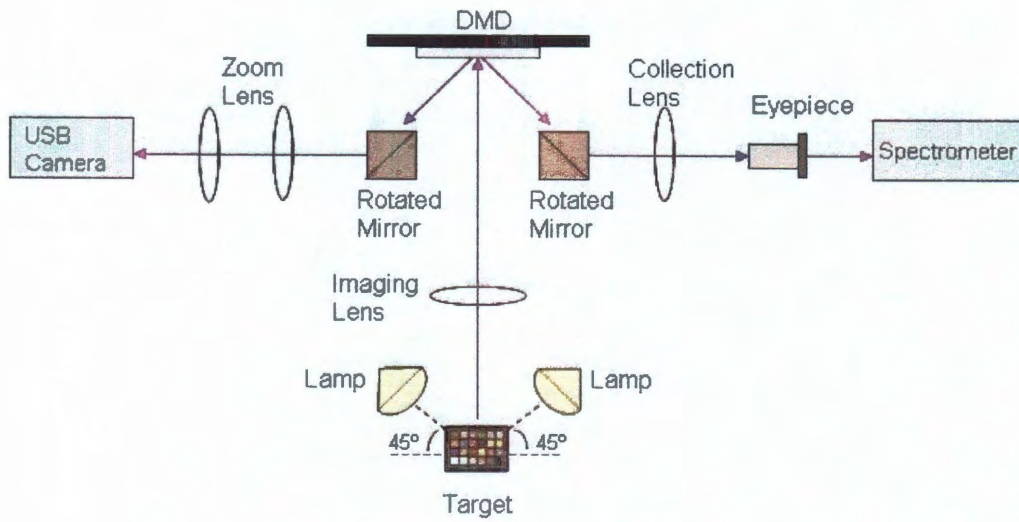


Figure 6.4 : CS hyperspectral imaging setup

### 6.3.2 Experiment Results

Our target was a standard colorchecker with 18 color and 6 gray patches, as shown in Figure 6.5. We displayed a sequence of  $128 \times 128$  random patterns on DMD. Each pattern was on hold for 25ms for a measurement acquisition. The spectrometer's integration time was set as 30ms which has to be a little longer than the DMD switching time, because the spectrometer's ADC needs a response time to read out data.

In this experiment, among 1044 wavelength channels, we chose the middle ones from  $200^{th}$  to  $800^{th}$  and averaged the spectrum every two channels. So totally there were 300 effective bands with wavelength range from 357nm to 815nm. The dense spectral information was adequate to distinguish different patches of the colorchecker. 5000 measurements were taken to reconstruct the hyper-cube. Every band was

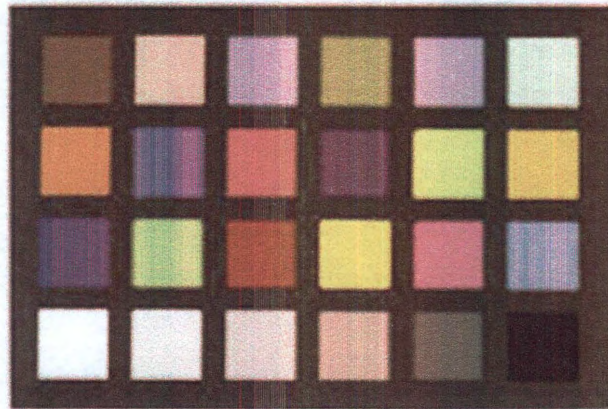


Figure 6.5 : A standard colorchecker: 18 color plus 6 gray patches.

reconstructed into a frame separately and these frames pile up together to form the  $128 \times 128 \times 300$  cube. In Figure 6.6, nine reconstructed spectral slices were picked up to demonstrate the gray-level light intensity variation of the patches with respect to the wavelength. Notice that for wavelength below 450nm or beyond 750nm, image qualities is getting worse, which is due to the low intensity of the light signal within this region. Figure 6.7 shows the illumination spectrum of our light source.

In the second experiment, three plastic objects — two peppers and an apple were imaged with the same setup. Only 6560 measurements were acquired to reconstruct a hyperspectral data cube with a lateral resolution of  $256 \times 256$  pixels and a spectrum resolution of 0.8nm. The compression rate was 10:1. The wavelength to RGB transform was performed based on 1964 CIE 10-deg XYZ Color-Matching Functions [84,85]. It converted the wavelengths of light to equivalent RGB values in the sRGB color space. To simplify data display, the spectrum was integrated into 49 channels



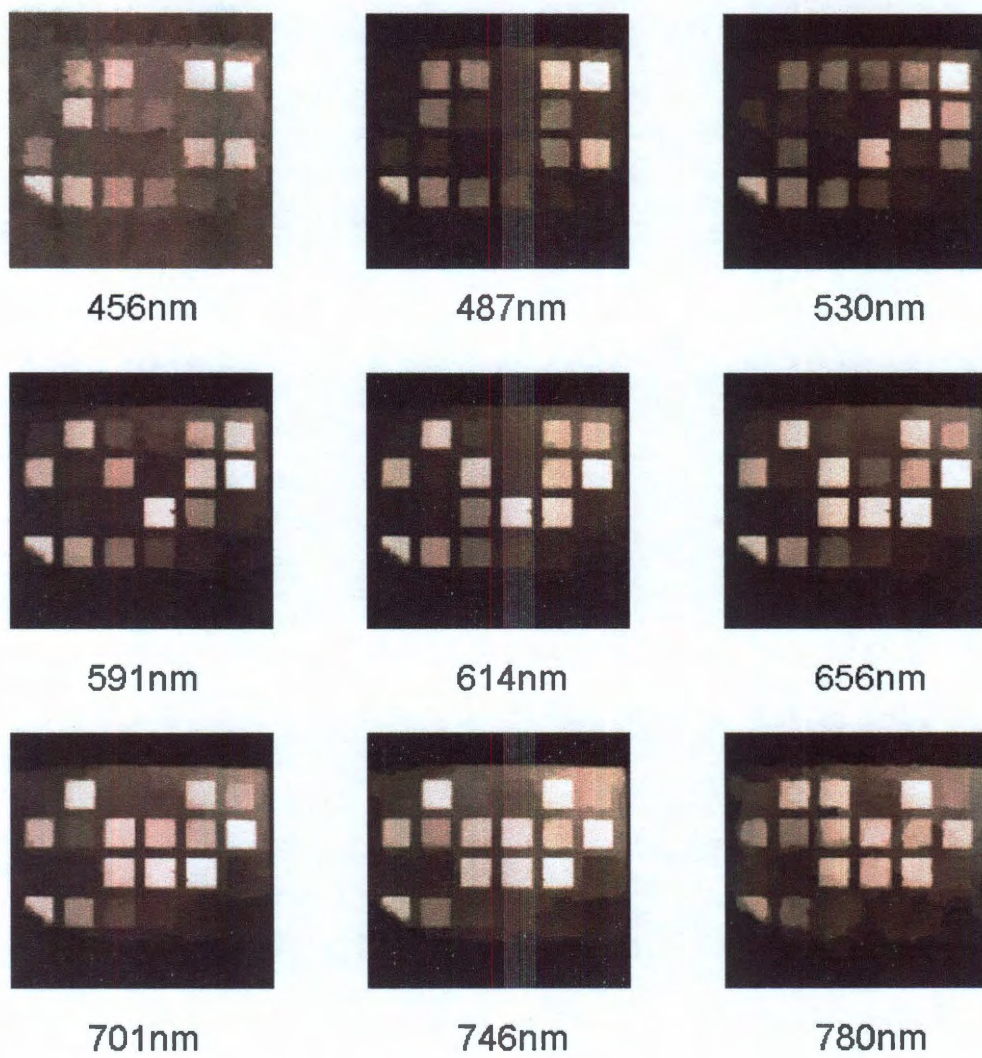


Figure 6.6 : Reconstructed spectral frames with 30% of total measurements

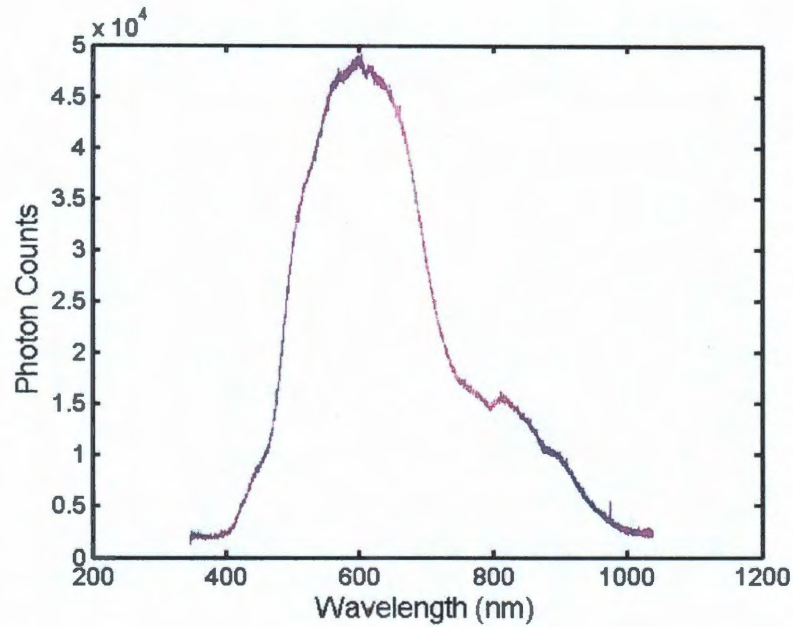


Figure 6.7 : Spectrum of the illuminating light source

from 445-640nm which means each channel was an average of spectra over 4nm. A  $7 \times 7$  montage is shown in Figure 6.8. When summing up all the visible bands from 360-830nm, we obtained the final colorful image of the target in Figure 6.8(b) which bore a strong resemblance to a digital camera image as in Figure 6.8(c).

Because CS measurement always captures  $1/2$  of the total light from the scene instead of  $1/N^2$  with raster scan, the signal to noise ratio is much higher. To compare against the CS results, we applied a pixel-by-pixel raster scan pattern and acquired the measurements under the same illumination and spectrometer integration conditions. As shown in figure 6.9, the left column is the raster results and the right one is the CS reconstruction for two different spectral bands. We can see that CS technique brings much better image quality in addition to saving 90% of acquisition time and



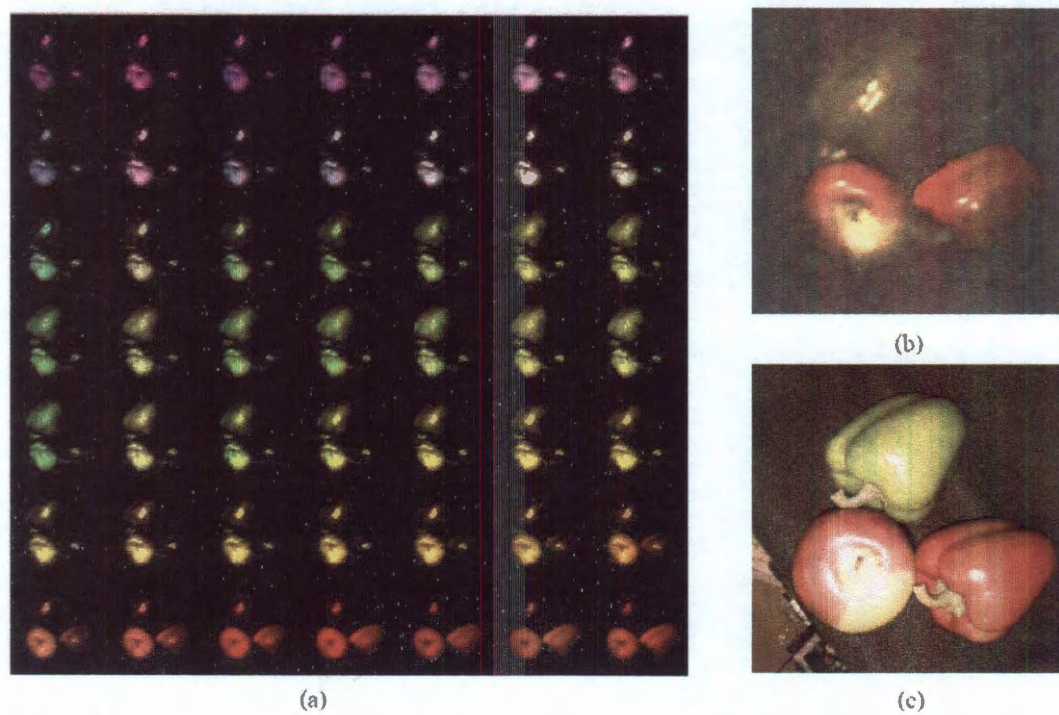


Figure 6.8 : (a) Montage of hyperspectral images with a lateral resolution of  $256 \times 256$  pixels and a spectrum resolution of 4nm. The compression rate is 10:1. (b) Reconstructed image after summing up all the visible bands. (c) Camera image

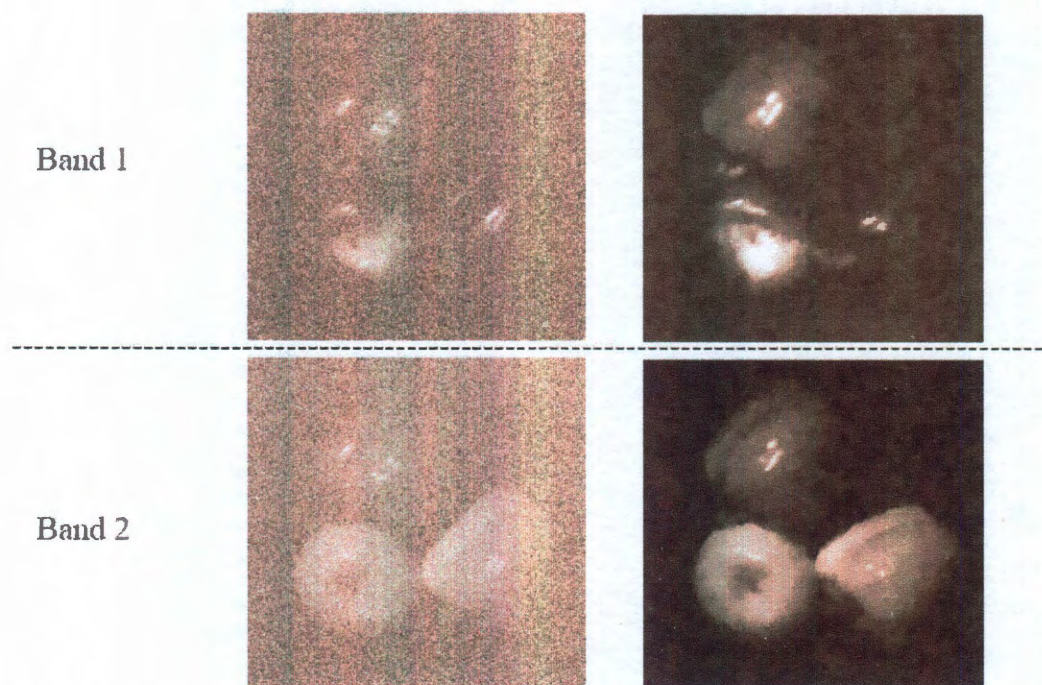


Figure 6.9 : Comparison of  $256 \times 256$  grey scale raster scan and CS reconstruction for two separate spectral bands

data storage volume compared to the traditional hyperspectral scanning acquisition method.

## 6.4 Hyperspectral Endmember Unmixing

### 6.4.1 Introduction

Hyperspectral imaging is a crucial technique to identify the composition of distinct material substances from observed spectra. The spectral unmixing is performed to decompose mixed pixels into a combination of pure spectral endmembers, weighted by their correspondent fractions or abundances that indicate the proportion of each

endmember in every pixel. A successful spectral unmixing relies on the definition of a mixing model, and the most popular one is the convex geometry model (also known as the linear mixing model) [86,87]. The linear mixing scenario assumes the negligible interaction among distinct endmembers [88], which is a plausible hypothesis in most cases.

In previous section, we have demonstrated that the single pixel camera setup [89] is extended to the acquisition and construction of the hyperspectral data cube. Furthermore, it can be applied to solve the unmixing problem. The process is to collect the compressed hyperspectral data, then recover the hyperspectral cube by CS optimization techniques, and finally decide the abundance fractions of endmembers by existing unmixing algorithms. However, due to the massive amount of data contained in the hyper-cube, it is usually too computationally costly to recover the entire cube and retrieve each endmember's information from it. Besides, the cube becomes unnecessary once we know the endmembers and corresponding abundance fractions.

We have proposed a CS unmixing model based on total variation (TV) minimization [90] and developed an efficient algorithm to solve it [91]. The underlying premise is that the gradient of each image composed by abundance fractions corresponding to some endmember can be regarded as being sparse. This is reasonable because most applications of hyperspectral imaging focus on characteristics or simply described as jumps in a scenario instead of those smooth parts. This algorithm directly unmixes the compressed hyperspectral data without reconstructing the whole cube in the middle process, which would remarkably reduce storage as well as computational cost.

In the following interpretation, we start from the assumption that we know exactly the number of involved endmembers and their spectral signatures. Solving the spatial distribution of each endmember is becoming a direct convex minimization problem.

However, in real applications, we always encounter the situation that the endmember's information is not accessible or precise. For example, due to influence of various noises from different instrument and experimental conductor or changing environment from illumination condition and variation, a priori knowledge of endmembers might be inaccurate and mislead the unmixing process. The design and implementation of blind CS unmixing algorithm will make the CS unmixing scheme more practically applicable since it can determine the endmembers' spectral signatures and abundance fractions simultaneously.

#### 6.4.2 CS Unmixing Model

Suppose that in a given scene there are totally  $n_e$  endmembers, with spectral signatures  $w_i \in \mathbb{R}^{n_b}$ , for  $i = 1, \dots, n_e$ , where  $n_b \geq n_e$  denotes the number of spectral bands. Assuming the negligible interaction among endmembers, the hyperspectral vector at the  $i^{th}$  pixel  $x_i \in \mathbb{R}^{n_b}$  can be regarded as a linear combination of the endmember spectral signatures, where the weights  $h_i \in \mathbb{R}^{n_e}$  represent the abundance fractions corresponding to each endmember, for any  $i \in \{1, \dots, n_p\}$ , where  $n_p$  denotes the number of pixels. In some scenarios, components of  $h_i$  are required to sum to one; i.e., the hyperspectral vectors lie in the convex hull of endmember spectral signatures [92]. We impose this constraint here for further descriptions, since both the model and the algorithm would stay similar but easier without the sum-to-one constraint. Furthermore, let  $X = [x_1, \dots, x_{n_p}]^T \in \mathbb{R}^{n_p \times n_b}$  denote a matrix representing the hyperspectral cube,  $W = [w_1, \dots, w_{n_e}]^T \in \mathbb{R}^{n_e \times n_b}$  the mixing matrix containing the endmember spectral signatures, and  $H = [h_1, \dots, h_{n_p}]^T \in \mathbb{R}^{n_p \times n_e}$  a matrix holding the respective abundance fractions. Then we have



$$X = HW, \quad H1_{n_e} = 1_{n_p}. \quad (6.1)$$

Since each column of  $X$  represents a 2D image corresponding to some spectral band, we can collect the compressed hyperspectral data  $F \in \mathbb{R}^{m \times n_b}$  by randomly sampling column by column using the same measurement matrix  $A \in \mathbb{R}^{m \times n_p}$ , where  $m < n_p$  is the number of samples from each column. Mathematically, the data acquisition model can be described as

$$AX = F. \quad (6.2)$$

Combining with (6.1), we get

$$AHW = F, \quad H1_{n_e} = 1_{n_p}. \quad (6.3)$$

With a priori knowledge of endmember spectral signatures, the goal is to figure out the abundance distribution  $H$  of each endmember in a scene directly from the compressed hyperspectral data  $F$ .

Under the premise that the gradient of each image composed by abundance fractions corresponding to some endmember is sparse, TV minimization optimization is performed here.  $H$  can be recovered by solving the following CS unmixing minimization problem

$$\begin{aligned} H^* &= \arg \min_H \sum_{j=1}^{n_e} TV(He_j) \\ \text{s.t. } &AHW = F, \quad H1_{n_e} = 1_{n_p} \end{aligned} \quad (6.4)$$

where

$$TV(He_j) \triangleq \sum_{i=1}^{n_p} \|D_i(He_j)\|. \quad (6.5)$$

Here,  $\|\cdot\|$  represents either 1-norm or 2-norm and  $D_i \in \mathbb{R}^{2 \times n_p}$  denotes the discrete gradient operator at the  $i^{th}$  pixel under the periodic boundary condition, as described in Chapter 2.

To separate the discrete gradient operator from non-differentiable term, a new splitting variables  $v_{ij} = D_i(He_j)(i = 1 \dots, n_p, j = 1 \dots, n_e)$  is introduced. The equation (5.4) is equivalent to solve

$$\begin{aligned} \min_{H, v_{ij}} \sum_j \sum_i \|v_{ij}\| \quad (6.6) \\ \text{s.t. } D_i(He_j) = v_{ij}, \text{ for } 1 \leq i \leq n_p, 1 \leq j \leq n_e, \\ AHW = F, \quad H1_{n_e} = 1_{n_p}, \end{aligned}$$

We apply the augmented Lagrangian method on (6.6), which minimizes its corresponding augmented Lagrangian function and then updates multipliers at each iteration. The augmented Lagrangian function can be written as

$$\begin{aligned} \mathcal{L}_A(H, v_{ij}) \triangleq \sum_j \sum_i \{ \|v_{ij}\| - \xi_{ij}^T (D_i(He_j) - v_{ij}) + \frac{\gamma_{ij}}{2} \|D_i(He_j) - v_{ij}\|_2^2 \} \\ - \Lambda \cdot (AHW - F) + \frac{\alpha}{2} \|AHW - F\|_2^2 - \nu^T (H1_{n_e} - 1_{n_p}) + \frac{\beta}{2} \|H1_{n_e} - 1_{n_p}\|_2^2, \end{aligned} \quad (6.7)$$

where  $\xi_{ij}$ ,  $\Lambda$ ,  $\nu$  are multipliers and  $\gamma_{ij}$ ,  $\alpha$ ,  $\beta$  are penalty parameters corresponding to three constraints in (6.6), respectively.

The complexity and storage primarily depend on the size of compressed data  $F$ . More precisely, it is proportional to  $n_b$ , the number of spectral bands. A singular value decomposition (SVD) preprocessing is performed on the measurements  $F$  to decrease the size of  $F$  from  $m \times n_b$  to  $m \times n_e$ , since the number of endmembers  $n_e$  is much smaller than  $n_b$ . This preprocessing would keep the solution set unchanged when  $F$  is noise-free. When  $F$  contains some random noise, even though the minimizers are not exactly

the same, this preprocessing helps drop down the noise level since truncated SVD annihilates those small singular values in  $F$  caused by noise. Therefore, this simple SVD preprocessing plays a key role during CS unmixing since it reduces not only complexity but also noise in practice. With the combination of SVD preprocessing [93] and the general augmented Lagrangian method (TVAL3) [94], the CS unmixing problem (6.4) can be solved.

### 6.4.3 Experiment Results

The testing target of this experiment was a print-out image of a color wheel, which was composed of three colors -yellow, cyan, and magenta. Each of them had four sectors with varying brightness. Their corresponding HSL values are listed in Table 5.1. From the compressed measurements, we selected 200 uniformly distributed bands in the range of  $400 \sim 800nm$  for abundance reconstruction. The spatial resolution was set to be  $128 \times 128$ . Spontaneously, we chose yellow, cyan, and magenta as three endmembers and measured their spectral signatures plotted in Figure 6.11.

The abundance fractions corresponding to three endmembers were recovered from 3270 measurements. The compression rate was 5:1. As indicated in Figure 6.12, the algorithm correctly detected the area corresponding to the three endmembers — yellow, cyan and magenta. The pixel intensities within each endmember's sectors were averaged, which revealed the luminance/brightness of corresponding color.

$$Y1 : Y2 : Y3 : Y4 = 2.38 : 1.98 : 1.47 : 1,$$

$$M1 : M2 : M3 : M4 = 2.48 : 2.20 : 1.71 : 1,$$

$$C1 : C2 : C3 : C4 = 2.33 : 2.04 : 1.59 : 1.$$

The relative intensity was slightly different with expected relative luminance ratio

	Hue	Saturation	Luminance
M1	200	240	120
M2	200	240	100
M3	200	240	75
M4	200	240	50
Y1	40	240	120
Y2	40	240	100
Y3	40	240	75
Y4	40	240	50
C1	120	240	120
C2	120	240	100
C3	120	240	75
C4	120	240	50

Table 6.1 : HSL Values of Color Wheel. M: Magenta, Y:Yellow, C:Cyan

of 2.4 : 2 : 1.5 : 1. It was due mostly to the measurement noise and the uneven illumination of the light source.

Once the abundance fraction  $H$  solved, the hyper-cube was estimated by simply multiplying  $H$  with the endmember's spectral signatures  $W$ . This recovered cube had a dimension of  $128 \times 128 \times 200$ . From the 200 band slices, we selected six of them to demonstrate in Figure 6.13. Specifically, "cyan" becomes bright around  $490 \sim 520nm$ ; "yellow" becomes bright around  $520 \sim 680nm$ ; "magenta" becomes bright around  $680nm$ . This result is consistent to the peak areas of three endmember's spectral signatures plotted in Figure 6.11.

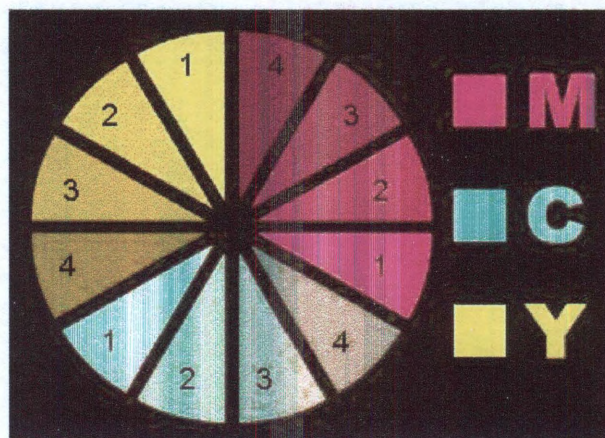


Figure 6.10 : "Color wheel" image under test.

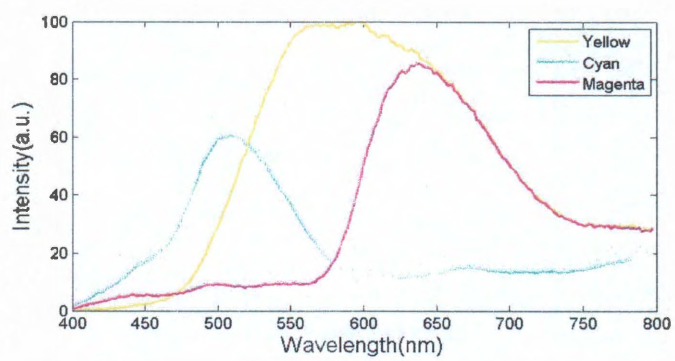


Figure 6.11 : Measured spectral signatures of the chosen endmembers.

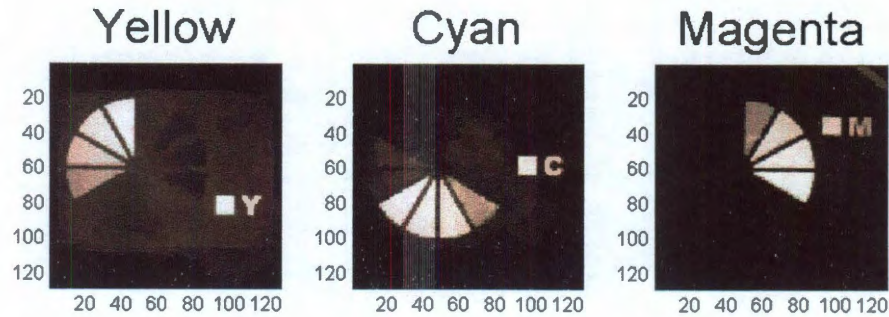


Figure 6.12 : Estimated abundance: CS unmixing solution from 10% measurements.

Figure 6.14 illustrates the slice-by-slice recovery result from the same amount of measured data. Instead of unmixing, hyperspectral cube was considered as a series of 2D images and the 2D TV solver TVAL3 was employed to recover each slice of hyperspectral cube from measured data recursively, as described in section 5.3. Neither endmembers nor abundance fractions were involved. In contrary to Figure 6.13, Figure 6.14 implies a much noisier result, which validates the denoising effects of the proposed unmixing algorithm. The remarkable improvement is facilitated by two main aspects: the low-rank decomposition of hyperspectral cube and the SVD preprocessing of measured data.

More tests were performed to study the impact of different types of noise to the CS unmixing method. For an image sensor (as used by a spectrometer), normally there are several types of noises involved - amplifier noise (Gaussian noise), impulsive noise (salt-and-pepper noise), periodic noise, quantization noise, etc. Here we simulated and testified the robustness of our model to three of them - Gaussian, periodic and



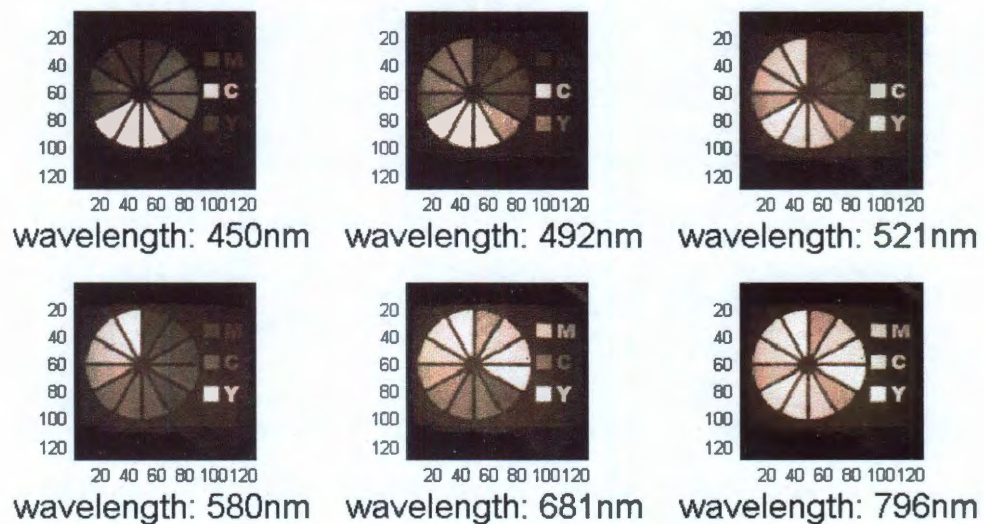


Figure 6.13 : Six slices computed by CS unmixing model.

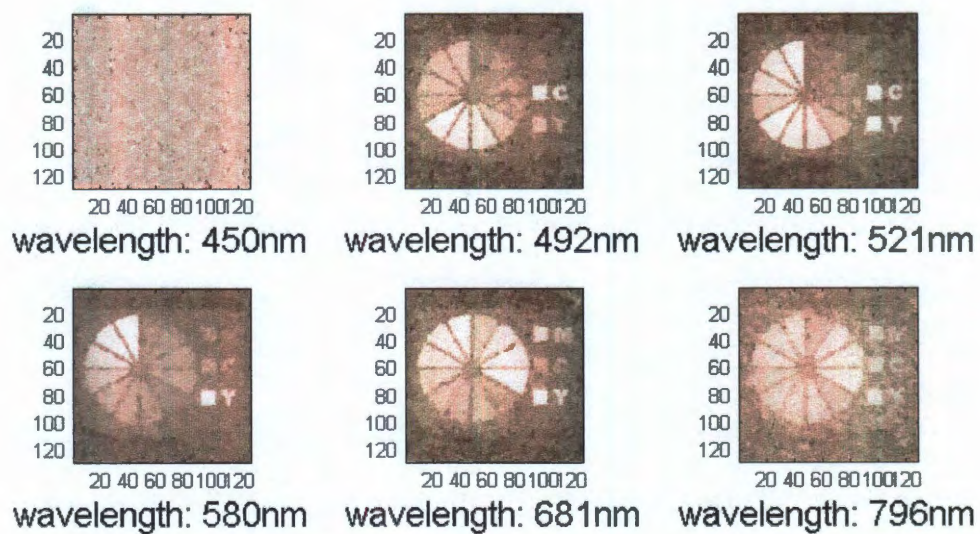


Figure 6.14 : Six slices computed slice-by-slice using 2D TV algorithm TVAL3.



impulsive noises respectively. The measurement data stays unchanged, while the input spectral signatures were imposed with the noises for reconstruction. All tests were done using 20% measurements.

In the first test, we demonstrated the robustness against Gaussian noise. Gaussian noise is an unavoidable type of noise that is a part of almost any signal. It usually occurs in low light conditions or photon counting systems. Especially for hyperspectral acquisition, a spectrometer is usually employed to distribute the light into hundreds or even thousands of channels, and the power in each channel is dissipated by orders. In this case, Gaussian noise becomes even more significant, and a robust algorithm capable of denoising is advantageous. As shown in Figure 6.15(a), the signatures of three endmembers were corrupted by Gaussian random noise and then input as the initial guess. From Figure 6.15(b), we can see that even though the signatures have been disturbed with a high noise level, the three endmembers are still correctly and clearly segmented. In the second test, a periodic noise was involved. Periodic noise is usually caused by electrical or electromechanical interference during signal acquisition. This noise results in sinusoidal patterns superimposed on the signal, having specific period and phase relationships. For example, the sensor is on the moving or vibrating platform or its circuit is affected by an external electrical field or magnetic source. It is also possible for hyperspectral imaging, such as the airborne hyperspectral sensors generally mounted to light aircraft. In our analysis, the original spectra were modulated with a sinusoidal function, and then added to the signatures of three endmembers so that they were deformed as shown in Figure 6.16(a). Starting with the corrupted signatures as a priori, we employed CS unmixing model to unmix the compressed data. Figure 6.16(b) shows that the recovered abundances are accurate.

Another type of noise was salt-and-pepper noise. It represents itself as randomly

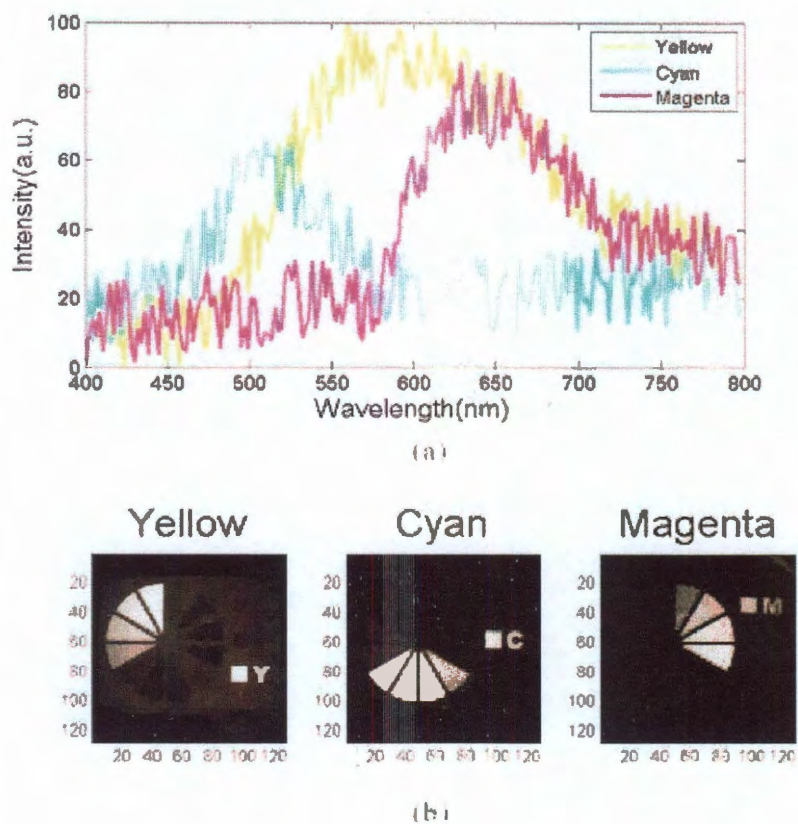


Figure 6.15 : (a) Input spectral signatures added with Gaussian noise. (b) Reconstructed abundances: CS unmixing solution from 20% measurements.

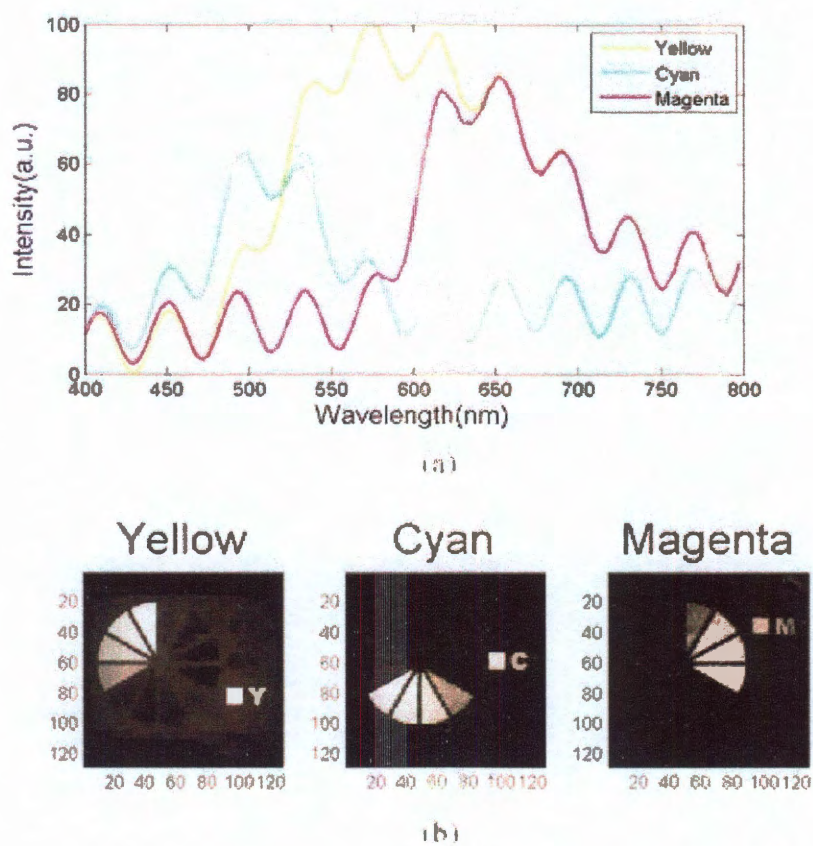


Figure 6.16 : (a) Input spectral signatures added with periodic noise. (b) Reconstructed abundances: CS unmixing solution from 20% measurements.

white and black in some positions. For example, in real application, sensors either fail to respond or saturate in error. A failed response gives a black spot in the image, which might be due to the malfunctioning pixel, faulty memory or timing error. So in the third test, this impulsive noise was applied on the signatures of three endmembers. The corrupted signatures were plotted in Figure 6.17(a) and provided as a priori information. Similarly, the abundances were successfully recovered as plotted in Figure 6.17(b).

Above three tests have covered the major types of noise possibly contained in hyperspectral data acquisition. Results have implied that the proposed CS unmixing algorithm is able to remove the noise from prior information and reconstruct every endmember's spatial distribution correctly and stably.

## 6.5 CS Blind Unmixing

### 6.5.1 Blind unmixing model

Notice that, in previous analysis, the endmember's spectral signature is a prior condition for computing. In other words, we have to know in advance how many endmembers in the area to be sensed and what their spectrum should be. If we miss or over count the actual components, or the spectral signatures are not accurate, the scheme might mislead the identification and fail the unmixing. For example, the reference spectrum from any library is measured with certain instrument under some particular conditions, barometric pressure, humidity level, temperature property, etc. Different measuring conditions might result in quite distinct spectrum for the same material. To overcome this difficulty, the CS unmixing model needs more robustness to handle the variations in spectra and recover the abundance fractions stably. This

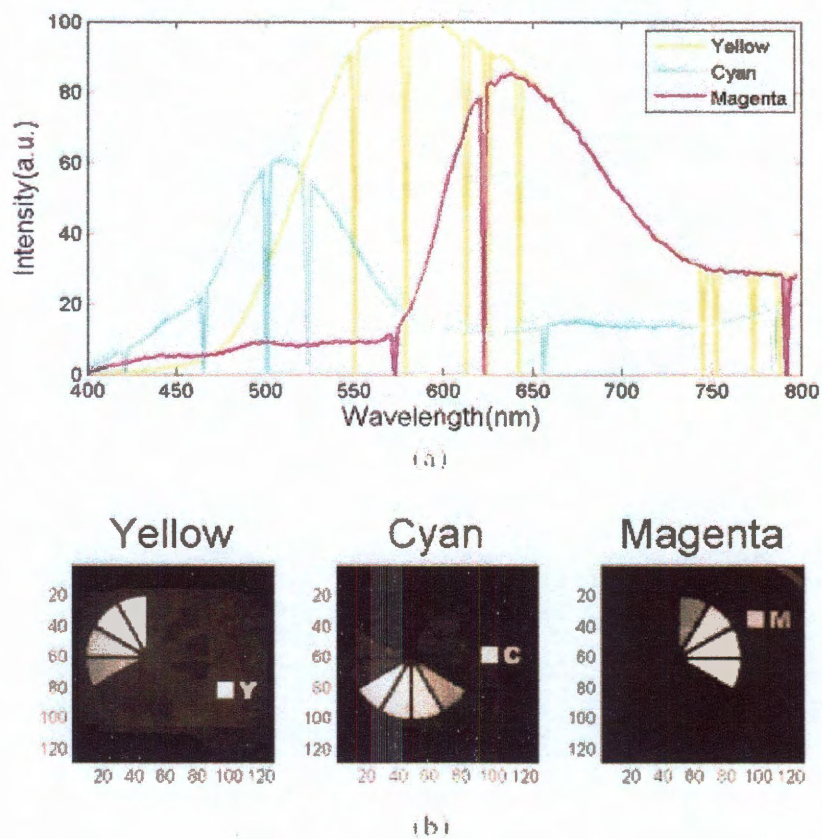


Figure 6.17 : (a) Input spectral signatures added with impulsive noise. (b) Reconstructed abundances: CS unmixing solution from 20% measurements.



extension on the CS unmixing model is named CS blind unmixing, which could update the endmember candidate's signature and the abundance with the constraint and optimization as required.

Under the same assumption of negligible interactions among endmembers, the data acquisition model (5.4) is still applicable. To extend CS unmixing scheme to blind unmixing, we consider the following CS blind unmixing model:

$$\min_{W,H} \sum_{j=1}^{n_e} TV(He_j), \quad \text{subjected to } AHW = F, \quad H1_{n_e} = 1_{n_p}. \quad (6.8)$$

Although the same objective function is used in both models, (5.4) is convex with linear constraints whereas (5.7) becomes a non-convex problem with nonlinear constraints.

The recent research on matrix completion [95] proposed an ADM-type method on a non-convex minimization problem, which turned out to be effective and efficient. The alternating direction method (ADM) is an extension of the classic augmented Lagrangian method. ADM solves the augmented Lagrangian function of the underlying problem with respect to each variable, and then update the multiplier. Unlike the augmented Lagrangian method, ADM avoids minimizing the augmented Lagrangian function exactly. More details about the inner algorithm and processing of the blind unmixing method are introduced in this document [96].

### 6.5.2 Experimental Results

In our first test, we measured the three endmember's signatures under another illumination source - white light LED. The new spectra are shown in Figure 6.18. To test our blind unmixing algorithm, one of the three endmember's signatures was replaced with the corresponding one under the LED illumination. Here we chose cyan as the



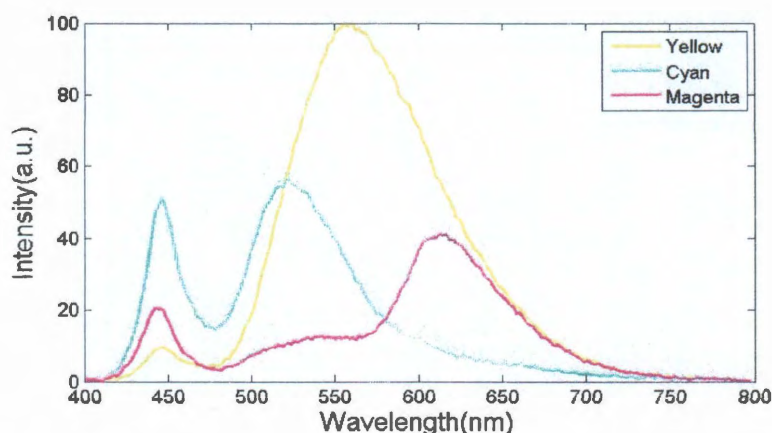


Figure 6.18 : Measured spectral signatures of the chosen endmembers under white light LED illumination.

endmember whose wrong signature was input as the initial guess. The other two were still represented with the right signatures. As shown in Figure 6.19(a), yellow and magenta's spectra together with the misleading one of magenta are granted as the input of the blind unmixing algorithm for reconstruction. Figure 6.19(b) reveals that magenta's signature is correctly recovered. Notice that the reconstructed cyan's spectrum still has a little deviation compared to the original one. However, the three color sectors are accurately differentiated.

In the second test, we further increased degrees of freedom as well as the difficulty of blind unmixing by assuming one of the three endmembers was completely missing. Its signature was replaced with an arbitrary guess. Here we simply assigned a curve to represent the initial guess of the missing endmember's signature. Note that this guess is not correlated to the other two. As illustrated in Figure 6.20, the recovered signatures match the characteristics of the original Y, M and C colors.

The results indicates that CS blind unmixing method is capable of retrieving

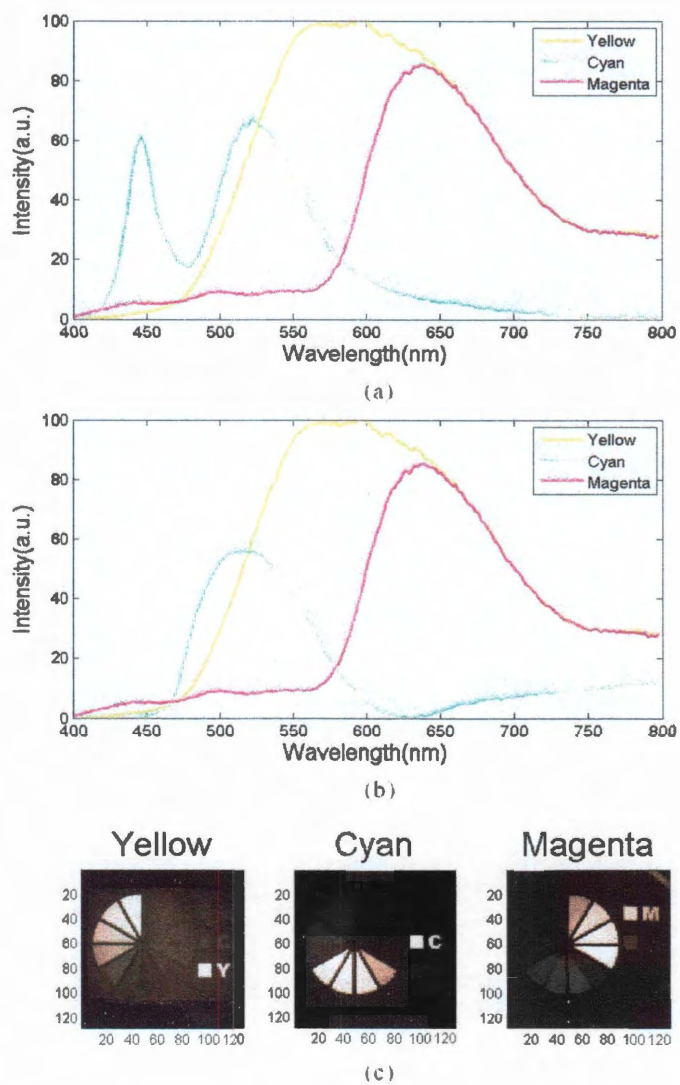


Figure 6.19 : (a) Initial Guess of spectral signatures. (Cyan's signature is switched.) (b) Recovered spectral signatures. (c) Reconstructed abundances: CS blind unmixing solution from 20% measurement.

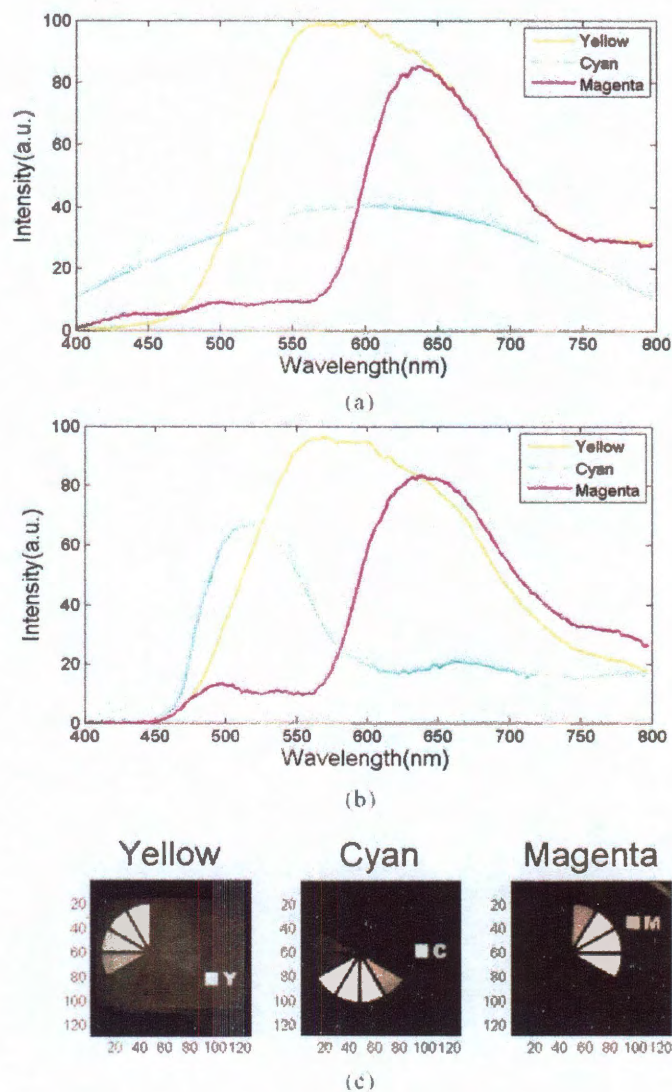


Figure 6.20 : (a) Initial Guess of spectral signatures. (Arbitrary guess of cyan's signature) (b) Recovered spectral signatures. (c) Reconstructed abundances: CS blind unmixing solution from 20% measurement.

signatures when one of them is deformed or completely missing. Due to the non-convex property of this problem, it is usually difficult to solve due to the existence of many local minima. However, our proposed method and newly developed algorithm have successfully resolved this issue. In a certain extent, the endmember' signature as well as the abundance distribution can be accurately recovered. However this method is not perfect yet. For example, the reconstruction depends on the initial guess of the spectral signature. Not all the arbitrary assumptions will lead to the correct result. It needs to be process a kind of similarity respect to the true signature. Totally random or groundless guesses may result in the unmixing failure. Moreover, if the missing spectral signatures are increased to two or all of them are severely deformed in our experiment, the reconstructions fails, too.

However, in spite of those limitations, the CS blind unmixing technique still holds great potential in the hyperspectral imaging field and is worthy of more research work to improve the performance and reliability for future applications.

## 6.6 Summary

The CS application in hyperspectral imaging and endmember unmixing is demonstrated. The CS unmixing scheme extracts the essential endmember information directly from the compressed measurements, in which cube reconstruction and end-member unmixing are combined into one step. The heavy burden on both hardware design as well as software implementation is relieved. CS blind unmixing, as a complement to normal unmixing technique, has a great potential in the real large-scale hyperspectral imaging application. Its efficiency have inspired us for further and deeper research along this direction.

## Chapter 7

### Conclusions

The CS imaging applications presented in this thesis are all based on the idea of single pixel camera. The signals are randomly manipulated by DMD before they are detected. The compressed measurements contain abundant information to recover the original signal back. This smart sensing mechanism has dramatically improves the detection efficiency of the sensor and also simplify the data processing procedure involved in the underlying DSP chips. It also offers a promising solution to a lot of difficulties and problems that traditional imaging systems are facing, such as high cost of 2D infrared imaging, long duration of raster scanning microscopy, complex processing of hyperspectral imaging, and so on. Meanwhile, it has the potential to create new applications in areas where currently no sensing/imaging schemes are possible or economically or physically impractical. For example, hyperspectral video camera. It is a 4D sensing system which captures both spatial, temporal and spectral information simultaneously. It is hard to realize with the current instrument, due to the low light signal and long acquisition time. However, in light of CS's unique property, it might be realized based on the compressive, random multiplexing technique.

The simple yet flexible single-pixel architecture for CS is based on 2D spatial light modulators. According to the driven force, light modulators are usually divided to electrically, mechanically, optically and thermally addressed devices. DMD, liquid crystal display (LCD) and liquid crystal on silicon (LCoS) are the common electrically-driven modulators. Deformable mirrors provide mechanical induced op-

tical modulation. Vanadium dioxide array is an example of thermal-optical light modulator. Among all of them, DMD's speed, precision, efficiency and broadband capability outperform other competitors. It is an ideal modulation device for imaging in UV, visible and IR regions.

Also, there are promising potential applications where current digital cameras have difficulty imaging where the DMD fails as a modulator, such as THz. Professor Mittleman's group at Rice University has built a terahertz modulator that could allow the terahertz radiation to reach the pixel through random pinholes electrically and fast. This modulator is made of active terahertz metamaterials, which consists of a planar array of subwavelength-sized split-ring resonator elements fabricated on a semiconductor substrate. Each pixel can be independently controlled by applying an external voltage. This first generation has only a resolution of 4 by 4, but its reasonably high switching speed still makes it a promising solution for CS terahertz imaging application.



## Bibliography

- [1] L. J. Hornbeck, “Digital light processing64: A new mems-based display technology,”
- [2] P. Van Kessel, L. Hornbeck, R. Meier, and M. Douglass, “A mems-based projection display,” *Proceedings of the IEEE*, vol. 86, pp. 1687–1704, aug 1998.
- [3] <http://www.rfcafe.com/references/electrical/NEETS20Modules/NEETS-Module-07-1-21-1-30.htm/>.
- [4] D. Bannan, “Hyperspectral imaging: Cubes and slices,” *Nature Photonics*, vol. 3, pp. 627–629, Nov. 2009.
- [5] E. Candes, J. Romberg, and T. Tao, “Robust uncertainty principles: exact signal reconstruction from highly incomplete frequency information,” *Information Theory, IEEE Transactions on*, vol. 52, pp. 489–509, feb. 2006.
- [6] D. Donoho, “Compressed sensing,” *Information Theory, IEEE Transactions on*, vol. 52, pp. 1289–1306, april 2006.
- [7] E. J. Candes and T. Tao, “Near-Optimal Signal Recovery From Random Projections: Universal Encoding Strategies,” *IEEE Transactions on Information Theory*, vol. 52, no. 12, pp. 5406–5425, 2006.
- [8] W. C. File:X-Ray Circuit Board Zoom 1.jpg. <http://commons.wikipedia.org/>.

- [9] E. T. Hale, W. Yin, and Y. Zhang, "Fixed-point continuation for  $\ell_1$ -minimization: Methodology and convergence," *SIAM Journal on Optimization*, vol. 19, no. 3, pp. 1107–1130, 2008.
- [10] M. Figueiredo, R. Nowak, and S. Wright, "Gradient projection for sparse reconstruction: Application to compressed sensing and other inverse problems," *Selected Topics in Signal Processing, IEEE Journal of*, vol. 1, pp. 586–597, dec. 2007.
- [11] S. Cotter and B. Rao, "Sparse channel estimation via matching pursuit with application to equalization," *Communications, IEEE Transactions on*, vol. 50, pp. 374–377, mar 2002.
- [12] D. Needell and J. A. Tropp, "Cosamp: Iterative signal recovery from incomplete and inaccurate samples," *Applied and Computational Harmonic Analysis*, vol. 26, no. 3, pp. 301–321, 2009.
- [13] T. Blumensath and M. Davies, "Iterative hard thresholding for compressed sensing," *Applied and Computational Harmonic Analysis*, vol. 27, no. 3, pp. 265–274, 2009.
- [14] L. I. Rudin, S. Osher, and E. Fatemi, "Nonlinear total variation based noise removal algorithms," *Phys. D*, vol. 60, pp. 259–268, November 1992.
- [15] Y. Wang, J. Yang, W. Yin, and Y. Zhang, "A new alternating minimization algorithm for total variation image reconstruction," vol. 1, no. 3, pp. 248–272, 2008.
- [16] J. Yang, Y. Zhang, and W. Yin, "A fast alternating direction method for tvl1-l2

- signal reconstruction from partial fourier data,” *Selected Topics in Signal Processing, IEEE Journal of*, vol. 4, pp. 288 –297, april 2010.
- [17] <http://www.caam.rice.edu/~optimization/L1/TVAL3/>.
- [18] M. Makoto and N. Takuji, “Mersenne twister: a 623-dimensionally equidistributed uniform pseudo-random number generator,” *ACM Trans. Model. Comput. Simul.*, vol. 8, pp. 3–30, January 1998.
- [19] W. Yin, S. Morgan, J. Yang, and Y. Zhang, “Practical compressive sensing with Toeplitz and circulant matrices,” in *Society of Photo-Optical Instrumentation Engineers (SPIE) Conference Series*, vol. 7744 of *Society of Photo-Optical Instrumentation Engineers (SPIE) Conference Series*, July 2010.
- [20] <http://www.janis.com/Products/AccessoriesandAncillaryEquipment/WindowTransmissionCurves.aspx/>.
- [21] R. G. Baraniuk, V. Cevher, M. F. Duarte, and C. Hegde, “Model-based compressive sensing,” *IEEE Trans. Inf. Theor.*, vol. 56, pp. 1982–2001, April 2010.
- [22] D. J. Brady, “Multiplex sensors and the constant radiance theorem,” *Opt. Lett.*, vol. 27, pp. 16–18, Jan 2002.
- [23] M. Maggioni, G. L. Davis, F. J. Warner, F. B. Geshwind, A. C. Coppi, and R. DeVerse, “Spectral analysis of normal and malignant microarray tissue sections using a novel micro-optoelectricalmechanical system (mod pathol 2004; 17 suppl 1: 358a),”
- [24] O. F. R. Center, “Galvanometer-based confocal scanning system.” <http://www.olympusfluoview.com/java/galvanometerscanning/index.html/>.

- [25] V. Bansal, S. Patel, and P. Saggau, "A high-speed confocal laser-scanning microscope based on acousto-optic deflectors and a digital micromirror device," in *Engineering in Medicine and Biology Society, 2003. Proceedings of the 25th Annual International Conference of the IEEE*, vol. 3, pp. 2124 – 2127 Vol.3, sept. 2003.
- [26] R. G. W. B. J. Dakin, *Handbook of Optoelectronics*. Taylor and Francis, 2006.
- [27] G. Binnig, "Scanning tunneling microscopy g. binnig and h. rohrer," *Surface Science*, vol. 126, no. 1-3, pp. 236–244, 1983.
- [28] L. Reimer, *Scanning electron microscopy : physics of image formation and microanalysis*. Springer, 1998.
- [29] C. B. Williams, D. B.; Carter, *Transmission Electron Microscopy*. Springer, 2009.
- [30] J. T. Woodward, H. Gwin, and D. K. Schwartz, "Contact angles on surfaces with mesoscopic chemical heterogeneity," *Langmuir*, vol. 16, no. 6, pp. 2957–2961, 2000.
- [31] Messerschmidt, R. G. and Harthcock, M. A., *Infrared Microspectroscopy: Theory and Applications*. Dekker: New York, 1988.
- [32] P. J. Treado, A. Govil, M. D. Morris, K. D. Sternitzke, and R. L. McCreery, "Hadamard transform raman microscopy of laser-modified graphite electrodes," *Applied Spectroscopy*, vol. 44, no. 8, pp. 1270–1275, 1990.
- [33] P. Guyot-Sionnest, R. Superfine, J. Hunt, and Y. Shen, "Vibrational spectroscopy of a silane monolayer at air/solid and liquid/solid interfaces using sum-

- frequency generation,” *Chemical Physics Letters*, vol. 144, no. 1, pp. 1 – 5, 1988.
- [34] P. Guyot-Sionnest, J. H. Hunt, and Y. R. Shen, “Sum-frequency vibrational spectroscopy of a langmuir film: Study of molecular orientation of a two-dimensional system,” *Phys. Rev. Lett.*, vol. 59, pp. 1597–1600, Oct 1987.
- [35] X. D. Zhu, H. Suhr, and Y. R. Shen, “Surface vibrational spectroscopy by infrared-visible sum frequency generation,” *Phys. Rev. B*, vol. 35, pp. 3047–3050, Feb 1987.
- [36] J. Hunt, P. Guyot-Sionnest, and Y. Shen, “Observation of c-h stretch vibrations of monolayers of molecules optical sum-frequency generation,” *Chemical Physics Letters*, vol. 133, no. 3, pp. 189 – 192, 1987.
- [37] Y. Shen, J. Swiatkiewicz, J. Winiarz, P. Markowicz, and P. N. Prasad, “Second-harmonic and sum-frequency imaging of organic nanocrystals with photon scanning tunneling microscope,” *Applied Physics Letters*, vol. 77, no. 19, pp. 2946–2948, 2000.
- [38] T. B. Huff, Y. Shi, Y. Fu, H. Wang, and J.-X. Cheng, “Multimodal nonlinear optical microscopy and applications to central nervous system imaging,” *IEEE journal of selected topics in quantum electronics a publication of the IEEE Lasers and Electrooptics Society*, vol. 14, no. 1, pp. 4–9, 2008.
- [39] R. D. Schaller and R. J. Saykally, “Near-field infrared sum-frequency generation imaging of chemical vapor deposited zinc selenide,” *Langmuir*, vol. 17, no. 7, pp. 2055–2058, 2001.
- [40] R. D. Schaller, J. C. Johnson, K. R. Wilson, L. F. Lee, L. H. Haber, and R. J. Saykally, “Nonlinear chemical imaging nanomicroscopy: from second and third

- harmonic generation to multiplex (broad-bandwidth) sum frequency generation near-field scanning optical microscopy,” *The Journal of Physical Chemistry B*, vol. 106, no. 20, pp. 5143–5154, 2002.
- [41] N. Ji, K. Zhang, H. Yang, and Y.-R. Shen, “Three-dimensional chiral imaging by sum-frequency generation,” *Journal of the American Chemical Society*, vol. 128, no. 11, pp. 3482–3483, 2006.
- [42] Y. Fu, H. Wang, R. Shi, and J.-X. Cheng, “Second harmonic and sum frequency generation imaging of fibrous astroglial filaments in ex vivo spinal tissues,” *Biophysical Journal*, vol. 92, no. 9, pp. 3251 – 3259, 2007.
- [43] A. V. Kachynski, A. N. Kuzmin, M. Nyk, I. Roy, and P. N. Prasad, “Zinc oxide nanocrystals for nonresonant nonlinear optical microscopy in biology and medicine,” *The Journal of Physical Chemistry C*, vol. 112, no. 29, pp. 10721–10724, 2008.
- [44] M. Flörsheimer, C. Brillert, and H. Fuchs, “Chemical imaging of interfaces by sum frequency microscopy,” *Langmuir*, vol. 15, no. 17, pp. 5437–5439, 1999.
- [45] D. M. P. Hoffmann, K. Kuhnke, and K. Kern, “Sum-frequency generation microscope for opaque and reflecting samples,” vol. 73, no. 9, pp. 3221–3226, 2002.
- [46] K. Kuhnke, D. M. P. Hoffmann, X. C. Wu, A. M. Bittner, and K. Kern, “Chemical imaging of interfaces by sum-frequency generation microscopy: Application to patterned self-assembled monolayers,” vol. 83, no. 18, pp. 3830–3832, 2003.
- [47] K. Cimatú and S. Baldelli, “Sum frequency generation imaging microscopy of co on platinum,” *Journal of the American Chemical Society*, vol. 128, no. 50, pp. 16016–16017, 2006.



- [48] K. Cimatu, H. J. Moore, T. R. Lee, and S. Baldelli, "Sum frequency generation imaging of microcontact-printed monolayers derived from aliphatic dithiocarboxylic acids: contrast based on terminal-group orientation," *The Journal of Physical Chemistry C*, vol. 111, no. 32, pp. 11751–11755, 2007.
- [49] S. Baldelli, G. Mailhot, P. Ross, Y.-R. Shen, and G. A. Somorjai, "Potential dependent orientation of acetonitrile on platinum (111) electrode surface studied by sum frequency generation," *The Journal of Physical Chemistry B*, vol. 105, no. 3, pp. 654–662, 2001.
- [50] K. A. Cimatu and S. Baldelli, "Chemical microscopy of surfaces by sum frequency generation imaging," *The Journal of Physical Chemistry C*, vol. 113, no. 38, pp. 16575–16588, 2009.
- [51] J. Hedberg, C. Leygraf, K. Cimatu, and S. Baldelli, "Adsorption and structure of octadecanethiol on zinc surfaces as probed by sum frequency generation spectroscopy, imaging, and electrochemical techniques," *The Journal of Physical Chemistry C*, vol. 111, no. 47, pp. 17587–17596, 2007.
- [52] K. Cimatu and S. Baldelli, "Spatially resolved surface analysis of an octadecanethiol self-assembled monolayer on mild steel using sum frequency generation imaging microscopy," *The Journal of Physical Chemistry C*, vol. 111, no. 19, pp. 7137–7143, 2007.
- [53] K. Cimatu and S. Baldelli, "Sum frequency generation microscopy of microcontact-printed mixed self-assembled monolayers," *The Journal of Physical Chemistry B*, vol. 110, no. 4, pp. 1807–1813, 2006.

- [54] M. Buck and M. Himmelhaus, "Vibrational spectroscopy of interfaces by infrared-visible sum frequency generation," vol. 19, no. 6, pp. 2717–2736, 2001.
- [55] R. Superfine, P. Guyot-Sionnest, J. H. Hunt, C. T. Kao, and Y. R. Shen, "Surface vibrational spectroscopy of molecular adsorbates on metals and semiconductors by infrared-visible sum-frequency generation," *Surface Science*, vol. 200, no. 1, pp. 445–450, 1988.
- [56] L. F. Scatena, M. G. Brown, and G. L. Richmond, "Water at hydrophobic surfaces: Weak hydrogen bonding and strong orientation effects," *Science*, vol. 292, no. 5518, pp. 908–912, 2001.
- [57] M. B. Raschke and Y. R. Shen, "Nonlinear optical spectroscopy of solid interfaces," *Current Opinion in Solid State and Materials Science*, vol. 8, no. 5, pp. 343–352, 2004.
- [58] Y. R. Shen, *The principles of nonlinear optics*. John Wiley: Hoboken, New Jersey, 2003.
- [59] R. W. Boyd, *Nonlinear optics*; Elsevier: New York, 2008.
- [60] H.-F. Wang, W. Gan, R. Lu, Y. Rao, and B.-H. Wu, "Quantitative spectral and orientational analysis in surface sum frequency generation vibrational spectroscopy (sfg-vs)," *International Reviews in Physical Chemistry*, vol. 24, no. 2, pp. 191–256, 2005.
- [61] A. L. Harris, C. E. D. Chidsey, N. J. Levinos, and D. N. Loiacono, "Monolayer vibrational spectroscopy by infrared-visible sum generation at metal and semiconductor surfaces," *Chemical Physics Letters*, vol. 141, no. 4, pp. 350–356, 1987.

- [62] F. Brown, R. E. Parks, and A. M. Sleeper, "Nonlinear optical reflection from a metallic boundary," *Phys. Rev. Lett.*, vol. 14, pp. 1029–1031, Jun 1965.
- [63] H. W. K. Tom, C. M. Mate, X. D. Zhu, J. E. Crowell, T. F. Heinz, G. A. Somorjai, and Y. R. Shen, "Surface studies by optical second-harmonic generation: The adsorption of  $O_2$ , CO, and sodium on the rh(111) surface," *Phys. Rev. Lett.*, vol. 52, pp. 348–351, Jan 1984.
- [64] R. B. Bass and A. W. Lichtenberger, "Microcontact printing with octadecanethiol," *Applied Surface Science*, vol. 226, no. 4, pp. 335–340, 2004.
- [65] S. Sarvotham, D. Baron, and R. G. Baraniuk, "Measurements vs. bits: Compressed sensing meets information theory," in *Proc. Allerton Conf. on Comm., Control, and Computing*, 2006.
- [66] NASA. <http://speclib.jpl.nasa.gov/>.
- [67] USGS Spectroscopy Lab. <http://speclab.cr.usgs.gov/spectral.lib04/spectral-lib04.html/>.
- [68] M. E. Winter, "N-FINDR: an algorithm for fast autonomous spectral end-member determination in hyperspectral data," in *Society of Photo-Optical Instrumentation Engineers (SPIE) Conference Series* (M. R. Descour & S. S. Shen, ed.), vol. 3753 of *Society of Photo-Optical Instrumentation Engineers (SPIE) Conference Series*, pp. 266–275, Oct. 1999.
- [69] J. Boardman, "Automating spectral unmixing of AVIRIS data using convex geometry concepts," *JPL Pub.93-26, AVIRIS Workshop*, vol. 1, pp. 11–14, 1993.

- [70] J. M. P. Nascimento and J. M. B. Dias, "Does Independent Component Analysis Play a Role in Unmixing Hyperspectral Data," *IEEE Transactions on Geoscience and Remote Sensing*, vol. 43, pp. 175–187, Jan. 2005.
- [71] C.-I. Chang, C.-C. Wu, W. Liu, and Y.-C. Ouyang, "A New Growing Method for Simplex-Based Endmember Extraction Algorithm," *IEEE Transactions on Geoscience and Remote Sensing*, vol. 44, pp. 2804–2819, Oct. 2006.
- [72] X. Tao, B. Wang, L. Zhang, and J. Q. Zhang, "A new scheme for decomposition of mixed pixels based on nonnegative matrix factorization," in *Geoscience and Remote Sensing Symposium, 2007. IGARSS 2007. IEEE International*, pp. 1759–1762, july 2007.
- [73] J. Bioucas-Dias, "A Variable Splitting Augmented Lagrangian Approach to Linear Spectral Unmixing," *ArXiv e-prints*, Apr. 2009.
- [74] J. Li and J. Bioucas-Dias, "Minimum volume simplex analysis: A fast algorithm to unmix hyperspectral data," in *Geoscience and Remote Sensing Symposium, 2008. IGARSS 2008. IEEE International*, vol. 3, pp. III –250 –III –253, july 2008.
- [75] T.-H. Chan, C.-Y. Chi, Y.-M. Huang, and W.-K. Ma, "A convex analysis-based minimum-volume enclosing simplex algorithm for hyperspectral unmixing," *Signal Processing, IEEE Transactions on*, vol. 57, pp. 4418 –4432, nov. 2009.
- [76] D. Manolakis, C. Siracusa, and G. Shaw, "Hyperspectral subpixel target detection using the linear mixing model," *Geoscience and Remote Sensing, IEEE Transactions on*, vol. 39, pp. 1392 –1409, jul 2001.

- [77] C.-I. Chang and D. Heinz, "Constrained subpixel target detection for remotely sensed imagery," *Geoscience and Remote Sensing, IEEE Transactions on*, vol. 38, pp. 1144 –1159, may 2000.
- [78] X. Li and A. Strahler, "Geometric-optical bidirectional reflectance modeling of the discrete crown vegetation canopy: effect of crown shape and mutual shadowing," *Geoscience and Remote Sensing, IEEE Transactions on*, vol. 30, pp. 276 –292, mar 1992.
- [79] H. Okamoto and W. S. Lee, "Green citrus detection using hyperspectral imaging," *Comput. Electron. Agric.*, vol. 66, pp. 201–208, May 2009.
- [80] J. Timlin, M. Sinclair, D. Haaland, J. Martinez, M. Manginell, S. Brozik, J. Guzowski, and M. Werner-Washburne, "Hyperspectral imaging of biological targets: the difference a high resolution spectral dimension and multivariate analysis can make," in *Biomedical Imaging: Nano to Macro, 2004. IEEE International Symposium on*, pp. 1529 – 1532 Vol. 2, april 2004.
- [81] G. Vane, R. O. Green, T. G. Chrien, H. T. Enmark, E. G. Hansen, and W. M. Porter, "The airborne visible/infrared imaging spectrometer (aviris)," *Remote Sensing of Environment*, vol. 44, no. 2-3, pp. 127 – 143, 1993. Airbone Imaging Spectrometry.
- [82] M. B. Sinclair, J. A. Timlin, D. M. Haaland, and M. Werner-Washburne, "Design, construction, characterization, and application of a hyperspectral microarray scanner.," *Applied Optics*, vol. 43, no. 10, pp. 2079–2088, 2004.
- [83] J. T. Daly, W. A. Bodkin, W. J. Schneller, R. B. Kerr, J. Noto, R. Haren, M. T. Eismann, and B. K. Karch, "Tunable narrow-band filter for lwir hyperspectral

imaging,” vol. 3948, no. 1, pp. 104–115, 2000.

- [84] <http://cvrl.ioo.ucl.ac.uk/database/text/cmfs/ciexyz64.htm/>.
- [85] P. W. Trezona, “Derivation of the 1964 cie 10-degree xyz colour-matching functions and their applicability in photometry,” *Color Research and Application*, vol. 26, pp. 67–75, 2001.
- [86] N. Keshava and J. F. Mustard, “Spectral unmixing,” *IEEE Signal Processing Magazine*, vol. 19, pp. 44–57, Jan. 2002.
- [87] J. M. Bioucas-Dias and J. M. P. Nascimento, “Estimation of signal subspace on hyperspectral data,” in *Society of Photo-Optical Instrumentation Engineers (SPIE) Conference Series* (L. Bruzzone, ed.), vol. 5982 of *Society of Photo-Optical Instrumentation Engineers (SPIE) Conference Series*, pp. 191–198, Oct. 2005.
- [88] R. N. Clark and T. L. Roush, “Reflectance spectroscopy - Quantitative analysis techniques for remote sensing applications,” *Journal of Geophysical Research*, vol. 89, pp. 6329–6340, July 1984.
- [89] D. Takhar, J. N. Laska, M. B. Wakin, M. F. Duarte, D. Baron, S. Sarvotham, K. F. Kelly, and R. G. Baraniuk, “A new compressive imaging camera architecture using optical-domain compression,” in *Society of Photo-Optical Instrumentation Engineers (SPIE) Conference Series* (C. A. Bouman, E. L. Miller, & I. Pollak, ed.), vol. 6065 of *Society of Photo-Optical Instrumentation Engineers (SPIE) Conference Series*, pp. 43–52, Feb. 2006.
- [90] L. I. Rudin, S. Osher, and E. Fatemi, “Nonlinear total variation based noise



removal algorithms,” *Physica D Nonlinear Phenomena*, vol. 60, pp. 259–268, Nov. 1992.

- [91] K. K. C. B. Li, T. Sun and Y. Zhang, “A compressive sensing and unmixing scheme for hyperspectral data processing,” *IEEE Transactions on Image Processing*, accepted 2011.
- [92] J. Nascimento and J. Dias, “Does independent component analysis play a role in unmixing hyperspectral data?,” *Geoscience and Remote Sensing, IEEE Transactions on*, vol. 43, pp. 175–187, jan. 2005.
- [93] C. Li, T. Sun, K. Kelly, and Y. Zhang, “Hyperspectral data compression and unmixing using compressive sensing techniques,” *IEEE Transactions on Image Processing*, Accepted.
- [94] C. Li, “An efficient algorithm for total variation regularization with applications to the single pixel camera and compressive sensing,” Mater Thesis, Computational and Applied Mathematics, Rice University 2009.
- [95] W. Y. Z.Wen and Y. Zhang, “Solving a low-rank factorization model for matrix completion by a non-linear successive over-relaxation algorithm,” 2010.
- [96] C. B. Li *PhD thesis*.